Dynamic Modeling, Reliability Analysis, and Control of Startup Transients in High Speed Web Handling Equipment

by

Manuel E. Jaime Esqueda

Submitted to the Department of Mechanical Engineering in partial fulfillment of the requirements for the degree of

Master of Science

at the

MASSACHUSETTS INSTITUTE OF TECHNOLOGY

May 1994

Author .....
Department of Mechanical Engineering
May 6, 1994

Certified by .....
David Hardt
Professor of Mechanical Engineering
Thesis Supervisor

Accepted by .....
Ain A. Sonin
Professor of Mechanical Engineering
Graduate Officer

Dynamic Modeling, Reliability Analysis and Control of Startup Transients in High Speed Web Handling Equipment

by

Manuel E. Jaime Esqueda

Submitted to the Department of Mechanical Engineering
on May 6, 1994, in partial fulfillment of the requirements
for the degree of Master of Science

Abstract

Production data from a web handling process reveals that 25% of all startup attempts fail to produce any product before the line is shut down. Further reliability analysis reveals that a particular unwind unit exhibits the same failure behavior and accounts for 3.42% of all failed startups. Failure rate functions for the unwind unit in the first minute after startup decrease dramatically; a clear indication that the failure of the system is directly correlated to uncontrolled dynamic transients in the first minute of operation. Measurement of dynamic transient lasting approximately 50 seconds confirm this hypothesis.

An interference model for system failures has been developed. It is based on the assumption the system fails every time peak tensions induced on the material during a startup transient overlap with a point in the lower end of the strength distribution of the material. Better tension control during startup is expected to alter the shape of the stress distribution so that interference and failures do not occur.

Linear and non-linear dynamic models have been developed for the unwind unit. The former has been validated using experimental data from production equipment. The latter has been used to run a designed experiment and the results have been compared to actual test data from a prototype unwind unit. Both models accurately reproduce machine states, but the non-linear model clearly reproduces test data much better. However, both models ignore the fact that tensions in the material are distributed in both time and space. Because material breakouts are due to localized peak tensions it is recommended that a distributed parameter model of the process be developed. This model will be able to predict tensions as a function of time and position and these estimates can be used within a feedback loop to accurately control tension using full state feedback.

Thesis Supervisor: David Hardt
Title: Professor of Mechanical Engineering

Acknowledgments

Once again, it is time to thank all of those that have made this possible. First of all I would like to thank Prof. Hardt for his guidance and support in the last two years. I have come to learn a whole lot about control and manufacturing. Dave, it has been a real pleasure working with you!

Thanks to all the people in the participating EIP company for this project who to a large extent made this possible. I am particularly grateful to Art Koehler for his insight, encouragement, support and camaraderie. All the time we devoted toward this project was well worth it. I thank him for making every day in the office an enjoyable one. Besides, I owe him a "Bohemia" in Mexico City. Thanks as well to Mike Looney ("the lunatic") for putting up with my behavior in our office; gracia bambino!

I also want to thank Tom Lange for his support of the project and his willingness to see it come through. Thanks to Eric Berg for his help and critiques. Thanks to Bub Stuebe for his critiques and recommendations, and for making his equipment available to us.

Very special thank you must go to the "Wizard of Ron". Ron, thanks a ton for helping us make all those measurements; the model would not have run without them. It was extremely enjoyable working with you. Enjoy Yosemite!

Thanks to Amy Chaney for her help in getting all sort of details worked out. Oh...and thanks for dinner too! Finally, I want to thank Jean Sparks for her warmth and "specially for that orange fan"; thanks for the token of appreciation.

Last, but not least I am grateful to all of those around me who know nothing about this thesis, but who where there to make it possible. Special thanks to Adeeb, Kay and Amar for making Greenhills a nice place to come home to. Thanks to Amit, Miguel, Alex, Aria, and others back in Boston and elsewhere who kept cheering all along.

....And finally a big big THANK YOU to my parents and grandmother for their love, never ending support and encouragement. Thanks for helping me go through MIT; these last five years would not have been the same without your love.

Para Papa Abo

Contents

List of Figures

Chapter 6

List of Tables

Chapter 1

Introduction

Dynamic transients in high speed web handling equipment can result in stress levels that exceed the strength of the material being processed. As a result the system can experience failed startups. The frequent occurrence of failed startups contributes to the reduction of the equipment's efficiency by increasing the amount of downtime and scrap. It is desirable, therefore, to reduce the number of failed startups so that the startup reliability of the equipment contributes to the overall reliability of the system. This thesis addresses the need for better process control to enhance the reliability of a high speed web handling process.

Using time distributions of system failures, the reliability of the web handling process was characterized. Multi-failure mode Weibull fits where used to determine instantaneous and cumulative failure probability functions. From these failure functions, failure rates (hazard functions) where estimated. The failure rate of the system rapidly decreases in the first minute after startup. That is, once the system has "survived" the first minute of operation, the probability it will fail is reduced considerably. The fact that failure distributions as skewed toward the first minute of operation indicates that there is something about the stress induced in the system by dynamic startup transients that results in system failures.

An interference model has been formulated to explain how startup dynamic transients result in system unreliability. The interference model assumes that the amount of overlap that exists between the strength distribution of the system and the stress distribution induced on the system by startup transients is equal to the unreliability of the process. In order to increase process reliability it is necessary to either shift the strength distribution to the right (higher values) or the stress distribution to the left (lower values).

The former action requires changing processing characteristics of the raw material and dealing with the process control of the supplier which can be cumbersome from an operations standpoint. Besides, it is likely that while attempting to obtain a stronger material other quality attributes can be compromised. On the other hand, shifting the stress distributions toward lower values can be achieved though better process control of the web handling equipment itself and can be applied to a variety of similar processes.

To quantify the interference model, it was necessary to obtain strength distributions from the supplier and estimate stress distributions induced on the system. The latter task was achieved by developing linear and non-linear models of the web handling equipment, validating the models and performing simulations for different processing conditions. Note that in estimating what the stress levels induced on the system are, it is expected that enhanced control for the process will be focused on controlling material states (tension and/or strain in the material) so that the overlap between stress and strength of the system is minimized and reliability is increased.

The analysis presented in this document is limited to a single unwinding unit operation in the web handling process. The operation chosen was selected because it is the most significant contributor to overall system unreliability and because its inherent physical behavior is not very different from other unit operations. Thus, the results obtained can be applied to other sub-systems that exhibit similar behavior.

The document begins with a complete probabilistic characterization of the system behavior and its failure mechanisms. In Chapter 3, a linear and a non-linear model of the unwind unit of interest is presented, followed by a description of the digital and analog control systems used during experimentation. The results of the experiments conducted on production equipment and a prototype unwind unit are presented in Chapter 5.

Chapter 6 includes the validation of the models and the estimates of the stress distributions induced on the unwind unit. The document concludes with a discussion of the results from model simulations as well as some short term and long term recommendations. A structure for a distributed parameter model that predicts tensions as a function of time and position is proposed. Such a model enables full state feedback to be used with an enhanced control system to better control tension and increase system reliability.

Chapter 2

Probabilistic Characterization of System Behavior

2.1 Reliability Theory Overview

Reliability is the probability that a system will perform its required or intended function, when used under specified conditions for a specified period of time. That is, reliability is a number between zero and one, where zero guarantees 100% failures and one guarantees 100% success.

To determine the reliability of a system it is necessary to measure the failures of the system over a specified period of time. The time distribution of these events is referred to as the Probability Distribution Function (PDF=f(t)) of failures. A sample PDF is shown in Figure 2.1.

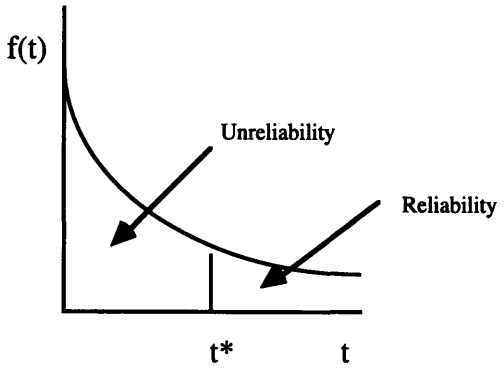

Figure 2.1: Sample Failure PDF

The "unreliability" of the system (the probability for failure) up to a given time t=t* is the ratio of the total number of failures to the total number of events (fraction failed). This ratio can be evaluated by integrating the PDF for failures from t=0 to t=t* as shown in Equation 2.1.

$$F(t^*) = \int_0^{t^*} f(t)\,dt \tag{2.1}$$

Similarly, the reliability of the system is the ratio of the total number of successes to the total number of events. To evaluate this ratio it is necessary to integrate the PDF from t=t* to t=∞. That is,

$$R(t^*) = \int_{t^*}^{\infty} f(t)\,\mathrm{dt} \tag{2.2}$$

Very often Equation (2.2) is difficult to evaluate. However, we can make use of the fact that the integral of the PDF from t=0 to t=∞is equal to one because the sum of the two ratios (reliability and unreliability) is equal to one (failures + successes = total events). Therefore we can express Equation (2.2) as,

$$R(t^*) = 1 - F(t^*) = 1 - \int_0^{t^*} f(t)\,dt \tag{2.3}$$

Another useful way of characterizing failure data is to consider the failure rate of a system, which is defined as the rate at which failures occur in a certain time interval for those devices surviving at the start of the interval (fraction failed per unit time).

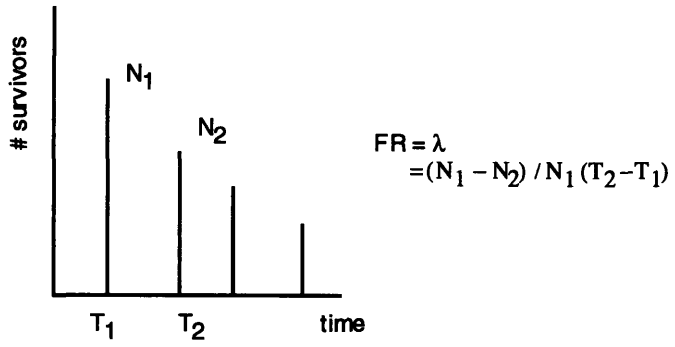

Figure 2.2: Failure Rate Concept

A hazard function is the limit of the failure rate as T2-T1 approaches 0. That is:

$$h(t) = \lim_{\Delta t \to 0} \frac{N1 - N2}{N1 \cdot \Delta t} \tag{2.4}$$

Equation (2.4) can be shown to be equivalent to:

$$h(t) = \frac{f(t)}{R(t)} \tag{2.5}$$

Models of hazard functions can be used to explain failure rates at different points in the operating life of a system. These models include:

- constant (or exponential PDF) hazard function
- linearly increasing hazard function
- piece-wise linear bathtub hazard function
- power function
- Weibull

The Weibull model is very commonly used because it is capable of fitting a wide range of data sets by changing its parameters. A two-parameter Weibull function is given by:

$$f(t) = \left(\frac{\beta (t)^{\beta - 1}}{\theta^{\beta}} \right) e^{-\left(\frac{t}{\theta}\right)^{\beta}} \tag{2.6}$$

Where β is known as the shape parameter and θ is known as the time characteristic parameter.

Different failure rate models describe different types of behavior in the operation of a system. A decreasing failure rate is indicative of premature failure (or "infant mortality") in the system. A constant failure rate reflects "normal" operating conditions in the system in which by design it is expected that the system will fail for "accidental" reasons at a certain rate. Finally, an increasing failure rate indicates that the system has reached its wear out region and is, therefore, failing often.

From a manufacturing standpoint, the different failure rate models can be thought of in the following way. Premature failure is induced by poor manufacturing practices that build or induce in the system certain characteristics that may cause it to fail. Constant failure rate occurs due to characteristics of the system that were built in by design and are irreducible unless the design is changed. That is, it is expected that on occasions the system will fail due to its inherent design limitations. Finally, wear out failures are expected to occur after a certain useful period of the system has gone by.

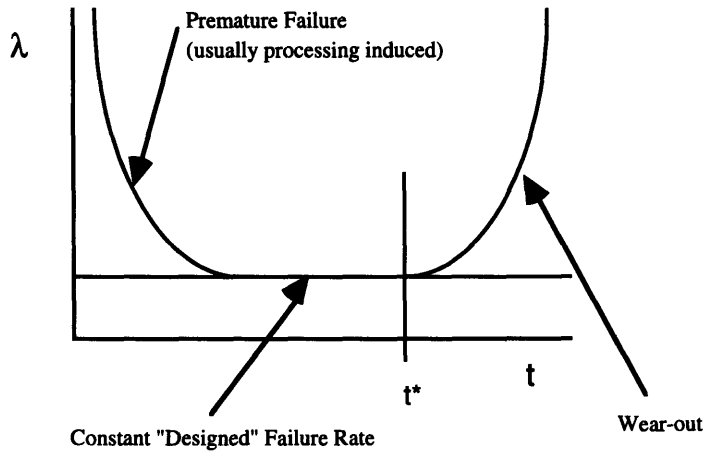

Figure 2.3: The "Bathtub Curve" in Relation to Manufacturing

2.2 Production Uptime Distributions of a Web Handling Process

Failure data for a web handling process has been obtained. Every time the process is stopped, a failure event is recorded. The area, cause, reason, and sensor that triggered the process to stop are downloaded to a data base. Associated with each event are two important time measurements. One is the uptime which is the amount of time the process was operating from the last startup to the moment is was stopped again. The other measurement is the downtime associated with a stop event, that is, the amount of time the process was not in operation.

For example, assume the process is running since time t=0. At time $t=t_1$, sub-system or area A fails and the process goes down. The event is recorded and the cause for the stop is attributed to sub-system A. At time t=t2, the process starts running again until it is once again interrupted due to some sub-system failure at time t=t3. The time history of the process looks something like this:

Event	Downtime	Uptime	Cause
1	5.6	3.7	sub-system A
2	1.8	10.8	sub-system C
3	8.9	2.3	sub-system A
4	3.2	9.6	sub-system B

Table 2.1: Sample Record of Uptime and Downtime Data

The data is interpreted as follows. The process was running from time t=0 until time t_1=3.7 min. when it stopped due to sub-system A and remained down until time t_3=9.3 min. for a total downtime of 5.6 min. The process began operating again and remained in operation until time t_4=20.1 min. when it was stopped due to sub-system C after a total uptime of 10.8 min.

We are interested in the uptimes associated with stop events because it is assumed that if the uptimes of a sub-system are short and the associated stop events occur frequently, the sub-system is experiencing premature failure. Furthermore, premature failure is possibly due to uncontrolled dynamic transients following a startup.

For example, Figure 2.4 shows the distribution of uptimes for the entire web handling process for a period of one month. The distribution is heavily skewed toward very short uptimes. As seen in the summary statistics, 25% of all events have an associated uptime of 0 min. This does not mean the process never ran, but rather that no finished product ever reached the end of the line.

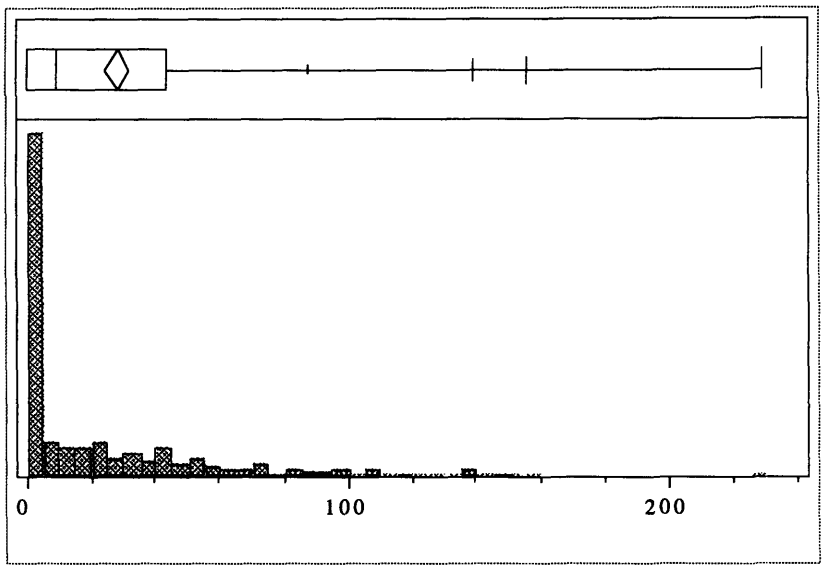

Figure 2.4: Uptime Distribution for One Month of Production

Summary Statistics:

Quantiles			Moments	
maximum	100.0%	229.20	Mean	28.4181
	99.5%	156.26	Std Dev	39.3470
	97.5%	140.05	Std Err Mean	1.6687
	90.0%	87.81	upper 95% Mean	31.6958
quartile	75.0%	43.93	lower 95% Mean	25.1403
median	50.0%	9.51	N	556.0000
quartile	25.0%	0.00	Sum Wgts	556.0000
	10.0%	0.00		
	2.5%	0.00		
	0.5%	0.00		
minimum	0.0%	0.00		

Similarly, if we look at the distribution of the uptimes for the unwind unit of interest we observe that the same shape is present in the distribution and 25% of uptime events also result in no finished product.

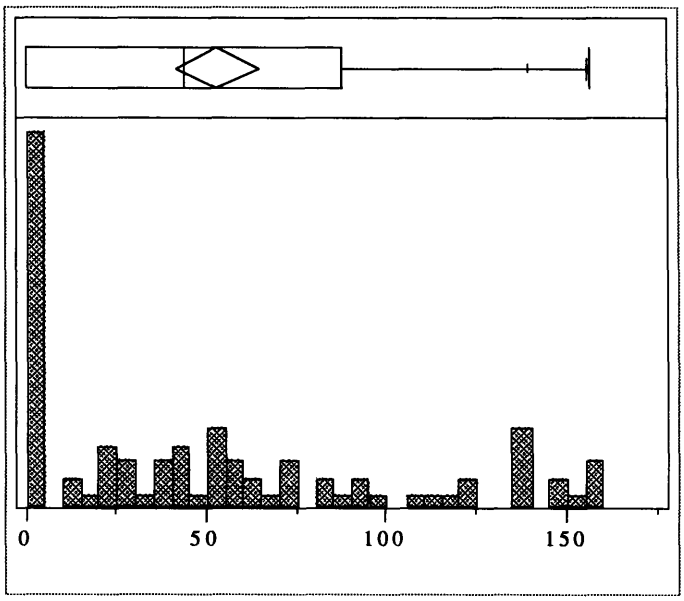

Figure 2.5: Uptime Distribution of the Unwind Unit for One Month of Production

Summary Statistics:

Quantiles			Moments	
maximum	100.0%	156.71	Mean	53.36055
	99.5%	156.71	Std Dev	51.31105
	97.5%	156.15	Std Err Mean	5.80983
	90.0%	139.88	upper 95% Mean	64.92945
quartile	75.0%	87.51	lower 95% Mean	41.79166
median	50.0%	43.75	N	78.00000
quartile	25.0%	0.00	Sum Wgts	78.00000
	10.0%	0.00		
	2.5%	0.00		
	0.5%	0.00		
minimum	0.0%	0.00		

From both uptime distributions it is quite obvious that the process as a whole and the process due to the unwind unit are exhibiting a significant number of false starts. In order to quantify the failure modes of the process due to the unwind unit, the following analysis was performed.

2.3 Suspended Item Analysis

The entire web handling process is composed of a series of subsystems that fail at different rates and exhibit different distributions. Because the failure data

that is obtained is for the entire system and we are interested in the reliability of one of the sub-systems it is necessary to perform what is known as suspended item analysis. The following example will be used to illustrate the idea behind suspended item analysis.

Imagine a collection of 1000 light bulbs that are simultaneously placed in operation. It is desired to obtain the reliability of the product by recording the number of failed bulbs and the time to failure. Thus, for example, the first light bulb might fail after 500 hours, the second one after 800, etc. Now imagine that at some point during the test there is a power surge and the test is interrupted. The power surge cannot be counted as a failure of the light bulbs, but must be accounted for by weighing the data appropriately. For example, the next failure that occurs after the power surge could have occurred before or after it did had the surge not occurred; weighting data appropriately accounts for this.

For every failure, there is an associated order number which in the case of no suspended items is always increased by one. However, in the case of suspended items, the data is weighed by incrementing the order number using the following formula, which is a way of averaging the order numbers.

$$I = \frac{(n+1) - \text{previous order \#}}{1 + \text{\# of items after suspension}} \tag{2.7}$$

Once the order numbers for the sequence of data have been calculated, point estimates for the cumulative failure distribution (F(t)) can be obtained using median ranking. That is, at the time of an event, the percent of items failed (items failed/# of items) is approximated by:

$$Pj = \frac{j - 0.3}{n + 0.4} \tag{2.8}$$

Where j is the order number and n is the number of events.

Table 2.2 summarizes the suspended item analysis procedure for 10 events. The numbers in the increment column are calculated using Equation (2.7)

Time	Results	Increment	Order #	Pj
544	Fail	1	1	(1-0.3)/(10+0.4) = 0.07
663	Fail	1	2	(2-0.3)/(10.4) = 0.16
802	Suspend	N/A	N/A	N/A
827	Suspend	N/A	N/A	N/A
897	Fail	((10+1)-(2)/(1+6)=1.3	3.3	(3.3-0.3)/(10.4) = 0.29
914	Fail	1.3	4.6	(4.6-0.3)/(10.4) = 0.41
939	Suspend	N/A	N/A	N/A
1084	Fail	((11)-(4.6))/(1+3)=1.6	6.2	(6.2-0.3)/(10.4) = 0.57
1099	Fail	1.6	7.8	(7.8-0.3)/(10.4) = 0.72
1202	Suspend	N/A	N/A	N/A

Table 2.2: Suspended Item Analysis Example

The same principle applies to the web handling process we are dealing with. We are interested in the reliability of a particular sub-system (an unwind unit in this case). This sub-system is often responsible for the failure of the entire process. However, there are occasions in which the process (and the operation of the unwind unit) are interrupted due to the failure of some other sub-system. This interruption in operation of the unwind unit can be treated as a suspended item.

In order to perform a suspended item analysis on this data and obtain fits for different distribution functions it is first necessary to format the data. We are interested in looking at the amount of uptime that precedes a stop due to a certain sub-system. Therefore, the first step is to order the data by increasing uptime. If the sub-system of interest is, for example, sub-system A, then failures due to other sub-systems are treated as suspended items. Order numbers and point estimates (Pj's) are then calculated. Once the point estimates have been calculated, a CDF (cumulative distribution function F(t), Equation (2.1)), a PDF (probability distribution function f(t), instantaneous probability) and a hazard function (h(t), Equation (2.5)) can be obtained using the procedure outlined in the following section.

2.4 System Failure Model Using Multi-failure Mode Fitting

The suspended item analysis procedure outline in Section 2.3 was applied to all the stops events for one month of production of a web handling process. The sub-system of interest was a particular unwind unit. The point estimates for the unwind unit are shown in Figure 2.6.

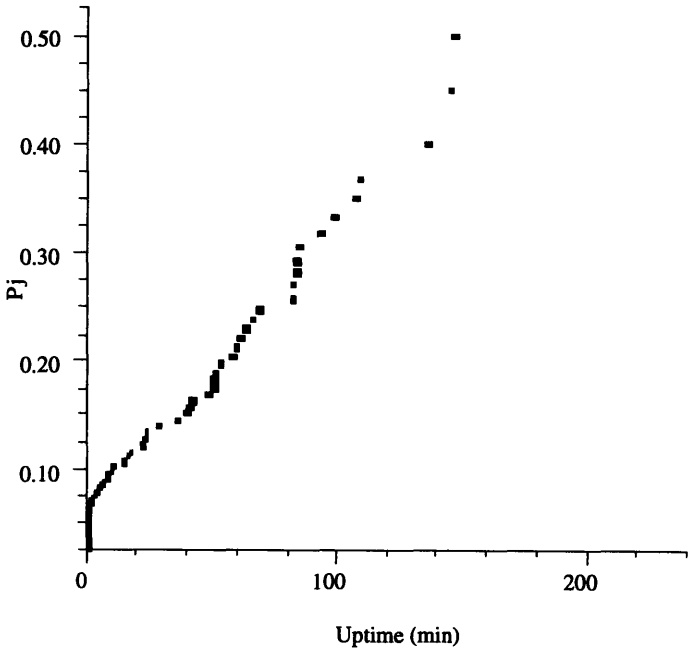

Figure 2.6: Point Estimates for Suspended Item Analysis of an Unwind Unit

The point estimates can be approximated with a Weibull function. That is, Equation (2.6) can be integrated with respect to time to obtain a cumulative distribution function given by:

$$Pj(t) \approx F(t) = 1 - e^{-\left(\frac{t}{\theta}\right)^{\beta}} \tag{2.9}$$

By taking the natural log on both sides of Equation (2.9), we can obtain a linear relationship and express it as:

$$ln\left[ln\left(\frac{1}{1-F(t)}\right)\right] = \beta ln(t) - \beta ln(\theta) \tag{2.10}$$

Approximating Pj(t) with F(t) and plotting Equation (2.10) on Weibull scale, the plot shown in Figure 2.7 is obtained.

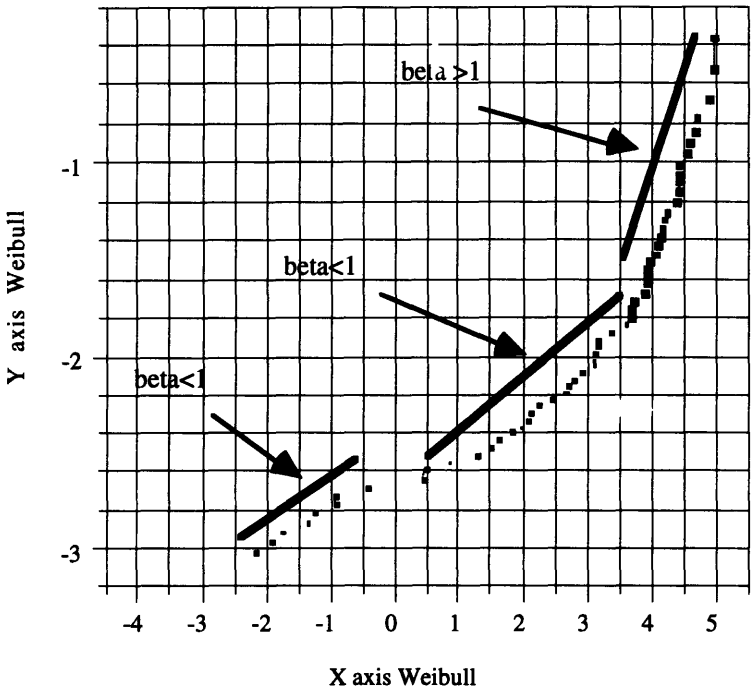

Figure 2.7: Weibull Scale Plot of Unwind Unit Point Estimates

If a single failure mode were present in the data, Figure 2.7 would be a straight line. The presence of several slopes indicates that there are several failure modes present in the data. Slopes (that is, β's) smaller than unity represent a decreasing failure rate, indicative of premature failure. Thus, the first two regions are the only regions of interest and are shown in Figure 2.8.

The three failure mode regions were split into subsets and linear fits were performed on each region to get initial estimates of the different β's and θ's. As seen in Figure 2.11, the third region has a slope>1 and is not indicative of premature failure.

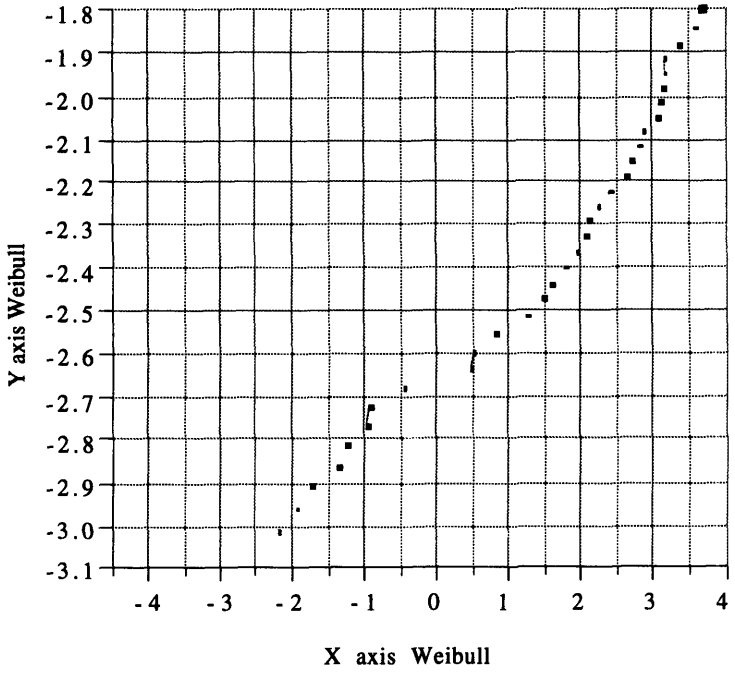

Figure 2.8: Weibull Scale Plot of Premature Failure Modes

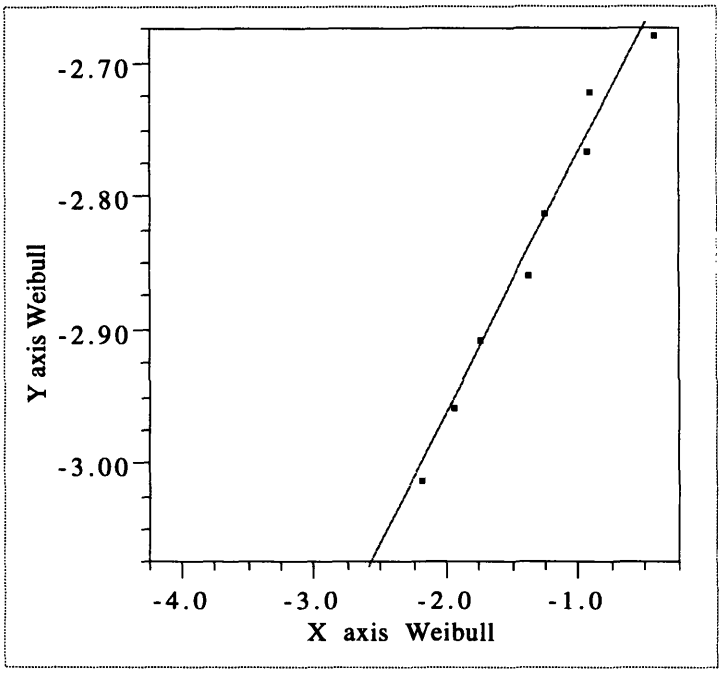

Figure 2.9: Region #1 Linear Fit

Linear Fit for Region #1

Summary of Fit

Rsquare	0.979776
Root Mean Square Error	0.017865
Mean of Response	-2.8386
Observations (or Sum Wgts)	8

Analysis of Variance

Source	DF	Sum of Squares	Mean Square	F Ratio
Model	1	0.09277318	0.092773	290.6717
Error	6	0.00191501	0.000319	Prob>F
C Total	7	0.09468819		0.0000

Parameter Estimates

Term	Estimate	Std Error	t Ratio	Prob>|t|
Intercept	-2.571325	0.0169	-152.1	0.0000
Beta	0.1959778	0.01149	17.05	0.0000

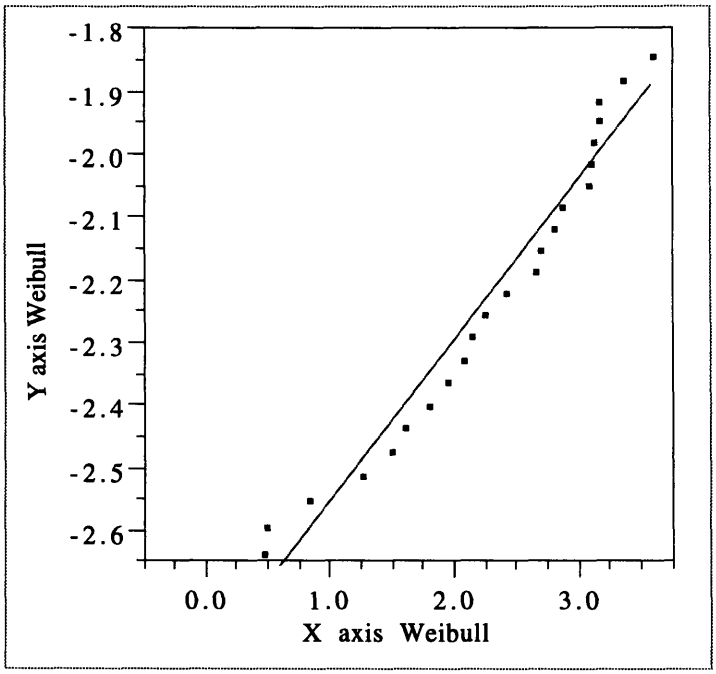

Figure 2.10: Region #2 Linear Fit

Linear Fit for Region #2

Summary of Fit

Rsquare	0.960789
Root Mean Square Error	0.048928
Mean of Response	-2.22543
Observations (or Sum Wgts)	23

Analysis of Variance

Source	DF	Sum of Squares	Mean Square	F Ratio
Model	1	1.2318471	1.23185	514.5599
Error	21	0.0502736	0.00239	Prob>F
C Total	22	1.2821207		0.0000

Parameter Estimates

Term	Estimate	Std Error	t Ratio	Prob>|t|
Intercept	-2.809049	0.02768	-101.5	0.0000
Beta	0.2572451	0.01134	22.68	0.0000

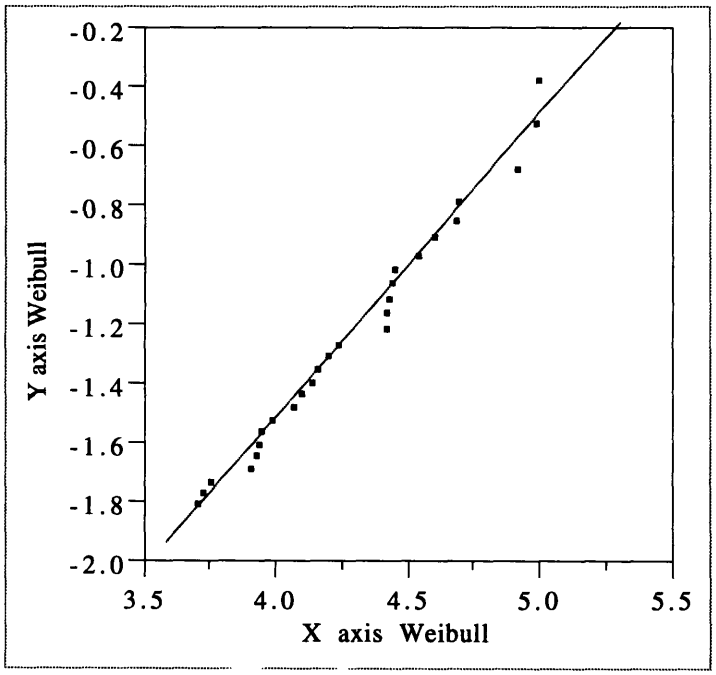

Figure 2.11: Region #3 Linear Fit

Linear Fit for Region #3

Summary of Fit

Rsquare	0.985168
Root Mean Square Error	0.049043
Mean of Response	-1.2286
Observations (or Sum Wgts)	26

Analysis of Variance

Source	DF	Sum of Squares	Mean Square	F Ratio
Model	1	3.8342095	3.83421	1594.113
Error	24	0.0577255	0.00241	Prob>F
C Total	25	3.8919350		0.0000

Parameter Estimates

Term	Estimate	Std Error	t Ratio	Prob>|t|
Intercept	-5.601213	0.10994	-50.95	0.0000
Beta	1.0221926	0.0256	39.93	0.0000

Once suspended item analysis has been done and the different failure modes have been identified, a multi-mode failure fit can be performed on the data. The multi-mode failure method is described by Kececioglu [7]. It consists on using the θ and β estimates from the individual regions as the starting points of a non-linear multiple regression for a CDF given by:

$$Pj = 1 - \left[\left(\frac{n_1}{n_t}\right) e^{-\left(\frac{uptime}{\theta_1}\right)^{\beta_1}} + \left(\frac{n_2}{n_t}\right) e^{-\left(\frac{uptime}{\theta_2}\right)^{\beta_2}} \ldots + \left(\frac{n_n}{n_t}\right) e^{-\left(\frac{uptime}{\theta_n}\right)^{\beta_n}} \right] \quad (2.11)$$

Where:

n_t = order number for last failed item

n_1 = order number at the end of region 1

θ_1 = scale parameter of region 1 subset fit

β_1 = shape parameter of region 1 subset fit

n_2 = order number at the end of region 2 minus n_1

θ_2 = scale parameter of region 2 subset fit

β_2 = shape parameter of region 2 subset fit

n_n = order number n_t minus n_{n-1}

θ_n = scale parameter of region n subset fit

β_n = shape parameter of region n subset fit.

Equation (2.11) was used to fit the first two regions of the CDF. Notice that the ratios of the order numbers are used to weight the Weibull functions for the individual regions. The resulting fit is shown in Figure 2.12.

The equation of fit for the point estimates is given by:

$$Pj(t) \approx F(t) = 1 - \left(\frac{37}{82} e^{-\left(\frac{uptime}{\theta}\right)^{\beta}} + \frac{45}{82} e^{-\left(\frac{uptime}{\theta_2}\right)^{\beta_2}} \right) \quad (2.12)$$

Where:

β = 0.1080506394

θ = 34,742,924

β_2 = .9430066469

θ_2 = 345.40862096

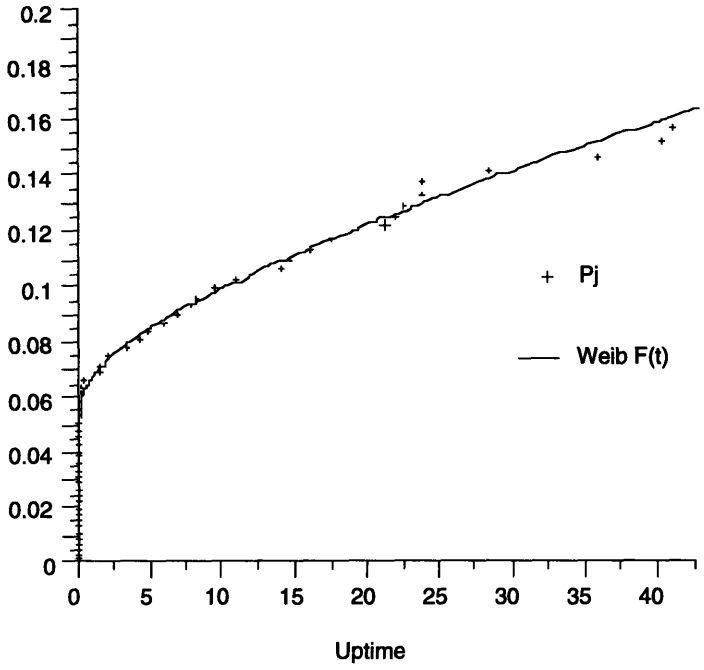

Figure 2.12: Two Parameter Weibull Fit

With the fit obtained for the cumulative failure function, it is possible to obtain f(t) (the instantaneous probability distribution function) by differentiating Equation (2.12) to obtain:

$$f(t)=\left[\left(\frac{37}{82}\right)\left(\frac{\beta}{\theta}\right)\left(\frac{uptime}{\theta}\right)^{(\beta-1)}\right]e^{-\left(\frac{uptime}{\theta}\right)^{\beta}} + \left[\left(\frac{45}{82}\right)\left(\frac{\beta_2}{\theta_2}\right)\left(\frac{uptime}{\theta_2}\right)^{(\beta_2-1)}\right]e^{-\left(\frac{uptime}{\theta_2}\right)^{\beta_2}} \tag{2.13}$$

The plot for the PDF (Equation (2.13)) is shown in Figure 2.13. It can be clearly seen that for very short uptimes, the probability of a failure is considerably higher than for longer uptimes; an indication of premature failure.

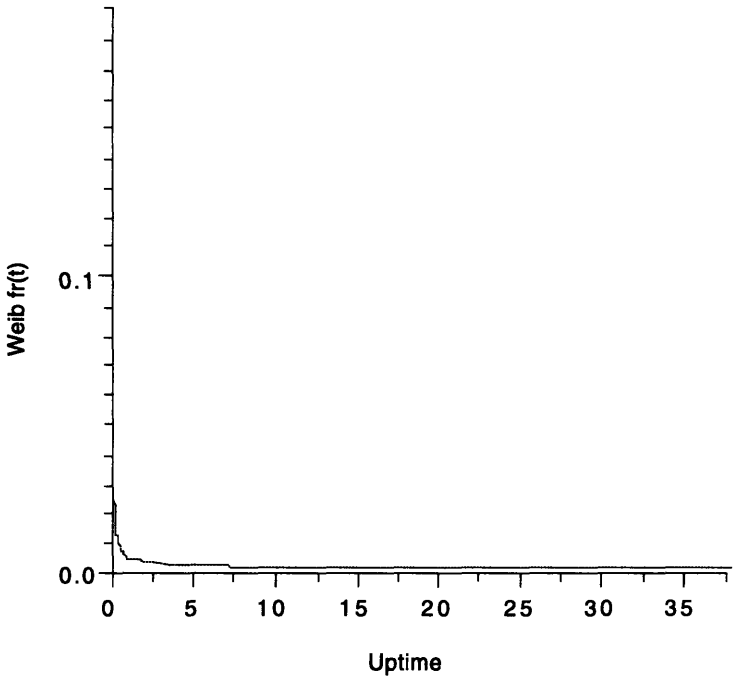

Figure 2.13: Instantaneous Failure Probability for the Unwind Unit

The premature failure mode is better appreciated if the PDF is plotted for the first two minutes of uptime.

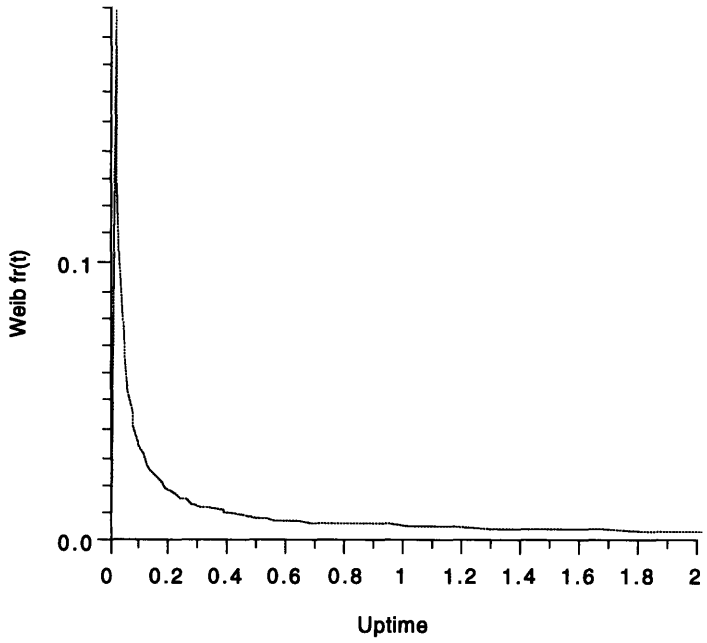

Figure 2.14: PDF of the Unwind Unit for Uptimes < 2 Minutes

As mentioned in Section 2.1, the clearest indication of premature failure is a decreasing failure rate h(t) which is the ratio of the PDF to the reliability of the system as seen in Equation (2.5). Figure 2.15 shows the hazard function of the unwind unit.

Once again the premature behavior is clearly shown in the first two minutes of uptime as seen in Figure 2.16. The time period in which a quick decrease in the failure rate occurs coincides with the duration of startup transients for the unwind unit. Therefore, it is reasonable to assume that uncontrolled dynamic transients are creating excessive stress in the unit which causes premature failures.

The following section presents the concept of an probabilistic interference model. The model shows that the overlap of the strength distribution of the system and the stress distribution induced by startup transients is equivalent to the unreliability of the system. Dynamic modeling of the transients and possible control solutions are addressed in the remaining chapters.

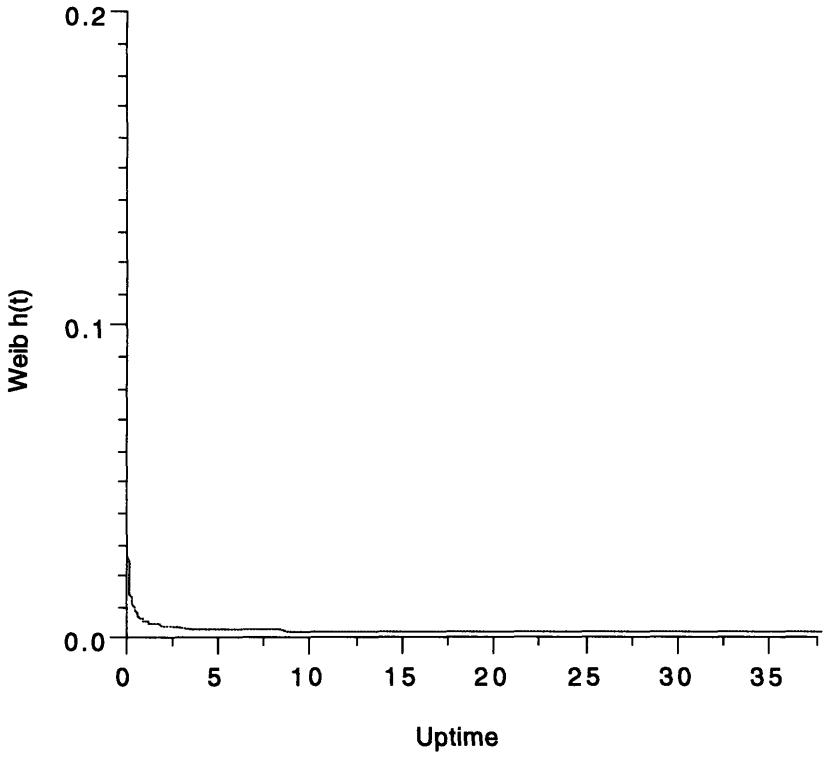

Figure 2.15: Hazard Function of Unwind Unit

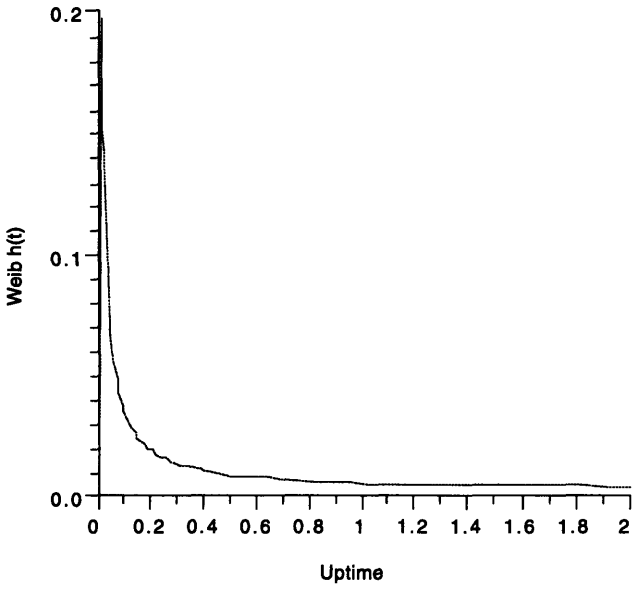

Figure 2.16: Hazard Function of Unwind Unit for Uptimes < 2 min.

2.5 Stress and Strength Distributions Interference Model

The unwind unit fails every time the induced stress in the system is of higher or equal value than the strength of the system. It is known that the induced stress and the strength of the system are not single values, but that there are underlying strength and stress distributions. When points in these distributions overlap, the strength of the system is exceeded and a failure occurs. Thus, it can be said that the failures of the unwind unit, that is, its unreliability is equal to the area where the strength and stress curves overlap as seen in Figure 2.17.

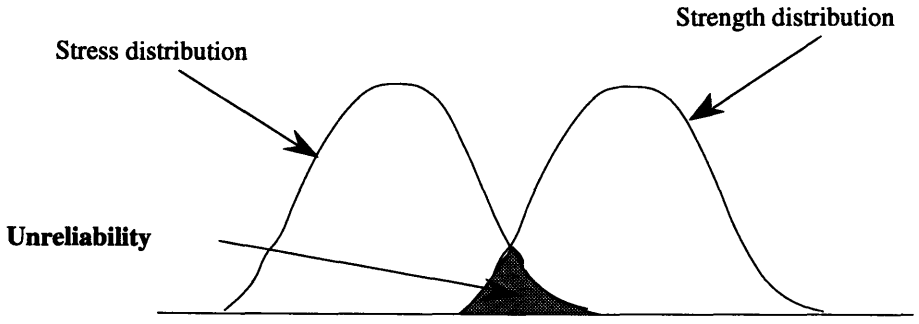

Figure 2.17: Interference Model Based on Strength and Stress Distributions

System failures have been characterized by PDF's CDF's and hazard functions. With these models we are able to calculate and predict the reliability of the unwind unit at different times. However, in the case of the interference model it is desired to determine what is the unreliability and

consequently what the area under the strength distribution that overlaps with the stress distribution.

It will be assumed that the peak stress induced in the system occurs during the first 15 seconds after a startup. By looking at all the stop events for the month of production data with which the hazard function was calculated, we find that out of the 556 stop events 19 of those are due to the unwind unit and occur in times less than 15 seconds. Thus we conclude that the unreliability of the unwind unit is:

$$F(t \leq 15 \text{ sec}) = \frac{19}{556} = 3.42\% \tag{2.14}$$

There is no extensive data on the stress distribution that the system is subjected to. However, the supplier of the unwind unit's raw material conducts ultimate tensile strength (UTS) tests on the material they produce. It should be pointed out, though, that the material is tested using 1 in wide samples when the actual web used is 5 in. Besides,, the strain rate at which the material is tested is 12 in/min. while the estimated startup strain rate in the process is approximately 40 in/min. Even though the ability to scale up the interference model formulated here is questionable, the principle behind it remains a valid one.

Distributions of the ultimate tensile strength data from the supplier have been fitted with Weibull functions and are shown in Figures 2.18 to 2.21 (the actual histograms from which this fits were obtained are shown in Appendix A). The x axis corresponds to grams of tension per inch of material width. The y axis is the probability distribution function of the ultimate tensile strength (UTS), that is, (f(UTS)).

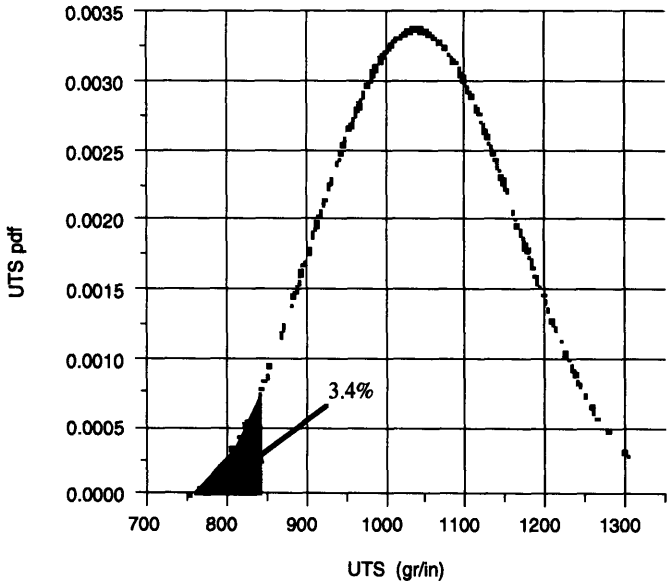

Figure 2.18: Strength Distribution #1 from Plant A

If we integrate the UTS PDF's to obtain CDF's (shown in Appendix A) we can find on the y axis (cumulative probability) the 3.42% mark and its corresponding UTS value. The area under the strength distributions up to that UTS value corresponds to 3.42% of the total area as shown in the plots. For the different distributions these values are:

- 839 gr. for the first distribution of plant A.
- 749 gr. for the second distribution of plant A.
- 755-765 gr. for the distribution of plant B.
- 780-805 for the combined distribution.

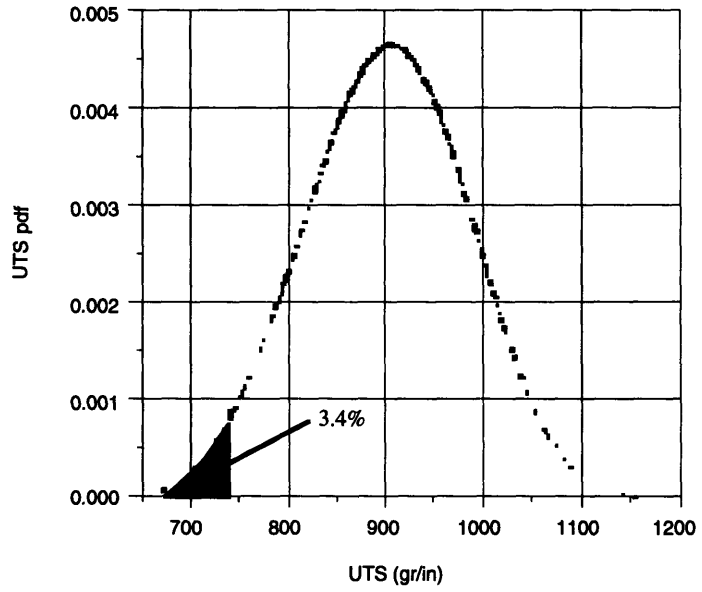

Figure 2.19: Strength Distribution #2 from Plant A

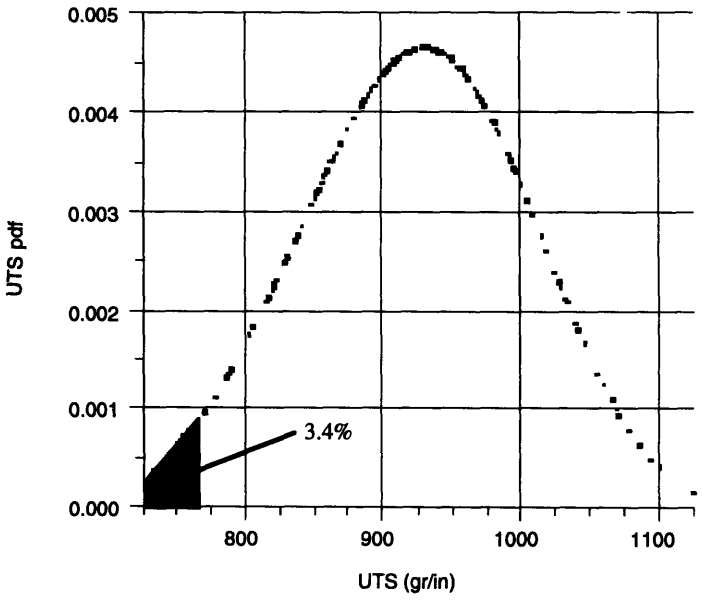

Figure 2.20: Strength Distribution from Plant B

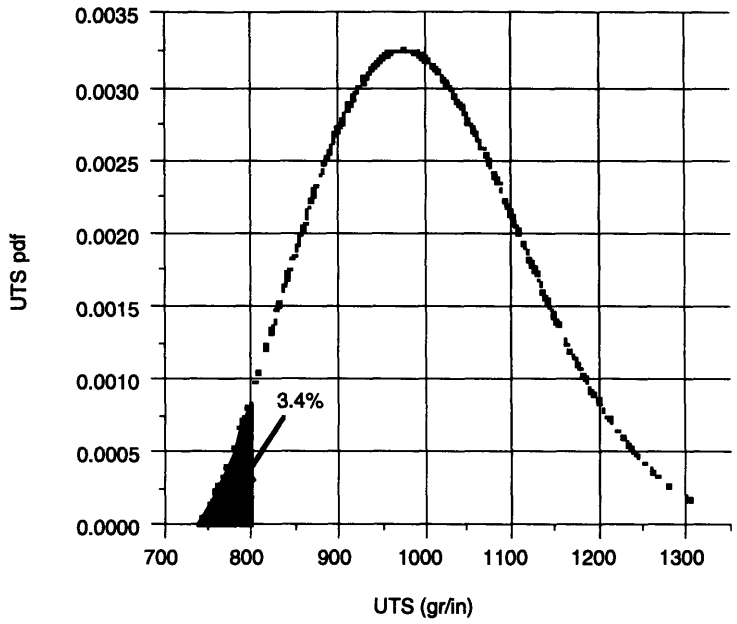

Figure 2.21: Combined Strength Distribution for Plants A and B

If we assume that a 5 in sample will have 5 times the UTS of a 1 in sample and convert that load to Newtons, tensions experienced by the material during failed startups were in the following regions:

- Between 36.78 N and 41.15 N for the first distribution of plant A.
- Between 32.91 N and 36.74 N for the second distribution of plant A.
- Between 35.90 N and 37.52 N for the distribution of plant B.
- Between 35.90 N and 39.49 N for the combined distribution (A and B)

Thus, whenever tension in the web is in the range of 30-40 N, it is likely that the material will break. However, as mentioned earlier, these estimates assume that the UTS of the web as it is being processed is not significantly different from that obtained during the tensile test performed by the supplier.

Notice, however, that in determining what is the range in which failures occur, it has been assumed that the tail of the stress distribution drops vertically at a given value. This is extremely unlikely and the actual maximum value at which failures occur is likely to be higher because the stress distribution does not drop off at a certain point, but rather has a decreasing slope. Unfortunately if we are to use UTS distributions to estimate the region of unreliability, a single point where the unreliability region ends is the best we can do. If information on the shape of the stress distribution where available, then the unreliability region would be better defined.

The following chapter describes two models that can be used to predict some points of the stress distribution induced on the system. The models are also useful in evaluating how different control methods can alter the shape and location of the stress distribution.

Chapter 3

Dynamic Models of Web Unwind Units

This chapter describes two lumped parameter models for a web unwind unit. The first model is a linear model and describes an unwind unit currently used in production systems. The second model accounts for non-linearities in the system's geometric configuration as well as material behavior non-linearities. Both models include controllers, unwind hardware, and web material. The first linear model of the production equipment utilizes an analog controller while the non-linear model describes a prototype unwind unit with a digital control system.

Both systems have been designed such that PI controllers attempt to keep certain machine states at constant values. The angular velocity of an unwind motor and the position of a dancer arm are the two states that are controlled. Unfortunately, as seen by the production data, controlling these machine states does not always insure that the material states (tension or strain) will be such that no distribution overlap occurs and the system does not fail.

Both models are an attempt to determine what the stress distribution of the system is. Simulating the tension in the web that can't be measured in the actual unwind unit and trying to alter it by modifying the control mechanisms employed will improve the startup reliability of the unwind units.

3.1 Description of Web Unwind Equipment

There are seven components in the system: the controller, the unwind motor, the transmission and surface belt drive, the roll of material, a dancer, idlers, and the material itself. For modeling purposes, the system shown in Figure 3.1 was split-up into two main components:

1) a web supply "block" comprised of the unwind motor, transmission, belt drive and the roll of material.
2) a web storage and transport "block" comprised of the material, dancer, and idlers.

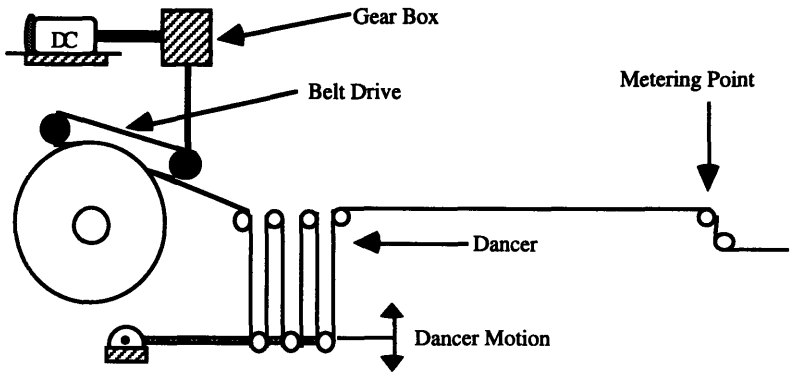

Figure 3.1: Web Unwind System Diagram

3.2 Linear Lumped Parameter Model

3.2.1 Web Supply Block Model

The simplest part of the system is comprised of the motor, transmission, surface belt drive and material roll. These four components are lumped into a single first order system with an equivalent inertia (J_{eq}) and an equivalent damping (b_{eq}). The bond graph in Figure 3.2 shows the complete system and the reflected equivalent inertia and damping. The motor has been modeled as an gyrator that given a certain current imposes a torque on the load. The gear box and belt drive have been modeled as an ideal transmission with no slippage or backslash.

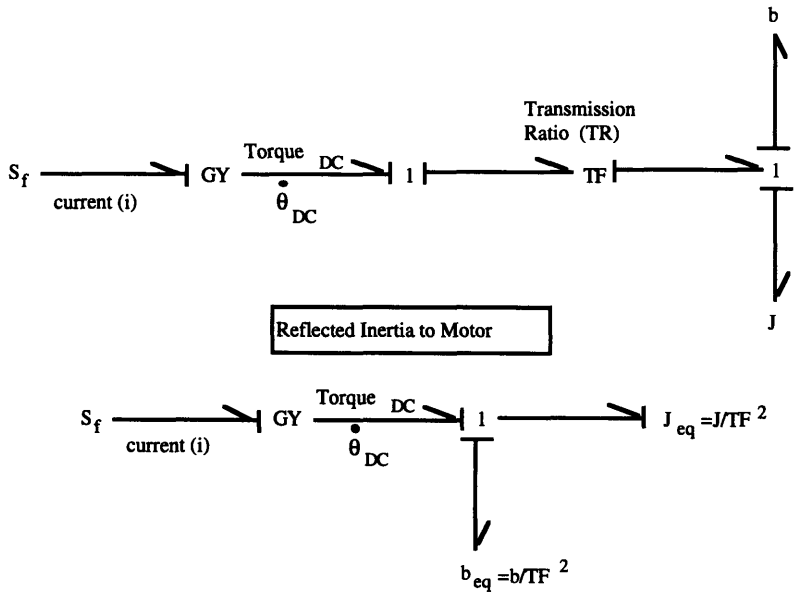

Figure 3.2: Web Supply Bond Graph

The resulting web supply block is shown in Figure 3.3. The input to the block is the current to the motor and the output is the angular velocity of the roll of material. Notice that the transmission ratio is a function of the roll radius. As the roll is used up, the equivalent inertia changes and so does the transmission. However, for a short duration transient (1 minute or less) it is reasonable to assume that the inertia and the transmission remain constant.

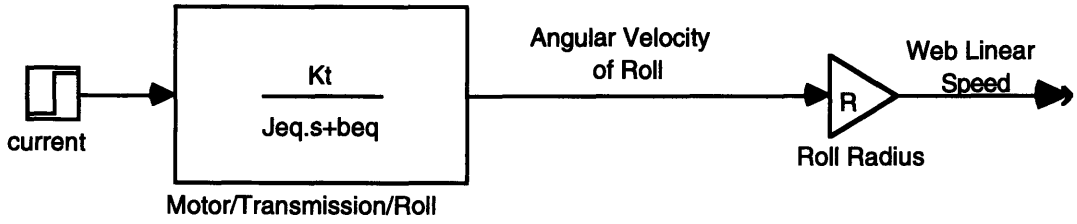

Figure 3.3: Web Supply Transfer Function

3.2.2 Dancer and Material Model

After the web leaves the roll is goes over a series of idlers, two of which are attached to a dancer arm that is free to rotate. In the lumped parameter model described in this section the continuous web is treated as a series of springs whose tension is only a function of time and not length. [1] The same modeling approach has been used in the past by other authors including Pfeiffer [10].

The approach used in modeling the material was to treat each individual span as a discrete and massless spring, whose constitutive equation is given by Hook's law:

$$F = K x \tag{3.1}$$

Taking the rate of change of the state variable, and assuming the length of the span remains approximately constant, the "spring equation" becomes:

$$\dot{F} = K \dot{x} \tag{3.2}$$

Which is the same form as Equations 3.3-3.6. The velocity ($\dot{x}$) is the net velocity difference seen across the endpoints of a spring. As long as that difference is not zero the force in the spring will be changing because the spring will either be experiencing elongation or compression.

If the tension in a span is to reach a steady state value, the velocities of the control points across the spring must be the same at the steady state. If the material being processed is not being strained significantly, this limitation might not be that important because the difference in linear web speeds from

---

[1] As will be shown later, the assumption that the continuous web can be modeled as discrete springs is the main limitation of the model.

one point to the other will probably be negligible. However, if it is necessary to meter a certain amount of relaxed material into the process, but the web at the metering point is stretched, it will be necessary for the linear speed of the web at the metering point to be higher than the speed coming off the roll. The material spring model, however, does not allow for that because for the tension to be constant at the steady state, the velocity across the spring must be zero. Thus, it is evident that treating each individual span as a discrete spring ignores the fact that the web is distributed in both time and space, and that the web "flows" and is constantly replenished.

The model of the system as shown in Figure 3.4 comprises four springs (one for each span) and four rotational inertias (three for the idlers and one for the dancer arm). The actual system has two idlers attached to the dancer arm, but for modeling purposes they have been lumped into a single idler. The four spans of the dancer (with a total length L), have been lumped into two spans each with length L/2.

The constitutive equations for the eight elements are:

$$\dot{F}_{K_1} = K_1\left(V_o - \dot{\theta}_1 r_1\right) \tag{3.3}$$

$$\dot{F}_{K_2} = K_2\left(\dot{\theta}_1 r_1 - \dot{\theta}_d r_d - R_d \dot{\theta}_a\right) \tag{3.4}$$

$$\dot{F}_{K_3} = K_3\left(\dot{\theta}_d r_d - \dot{\theta}_2 r_2 - \dot{\theta}_a R_d\right) \tag{3.5}$$

$$\dot{F}_{K_4} = K_4\left(\dot{\theta}_2 r_2 - V_1\right) \tag{3.6}$$

$$\ddot{\theta}_1 = \frac{1}{J_1}\left[\left(F_{K_1} - F_{K_2}\right) r_1 - b_1 \dot{\theta}_1\right] \tag{3.7}$$

$$\ddot{\theta}_2 = \frac{1}{J_2}\left[\left(F_{K_3} - F_{K_4}\right) r_2 - b_2 \dot{\theta}_2\right] \tag{3.8}$$

$$\ddot{\theta}_d = \frac{1}{J_d}\left[\left(F_{K_2} - F_{K_3}\right) r_d - b_d \dot{\theta}_d\right] \tag{3.9}$$

$$\ddot{\theta}_a = \frac{1}{J_a}\left[c_w R_w + \left(F_{K2} + F_{K3}\right) R_d - w_a R_{cm} - b_a \dot{\theta}_a\right] \tag{3.10}$$

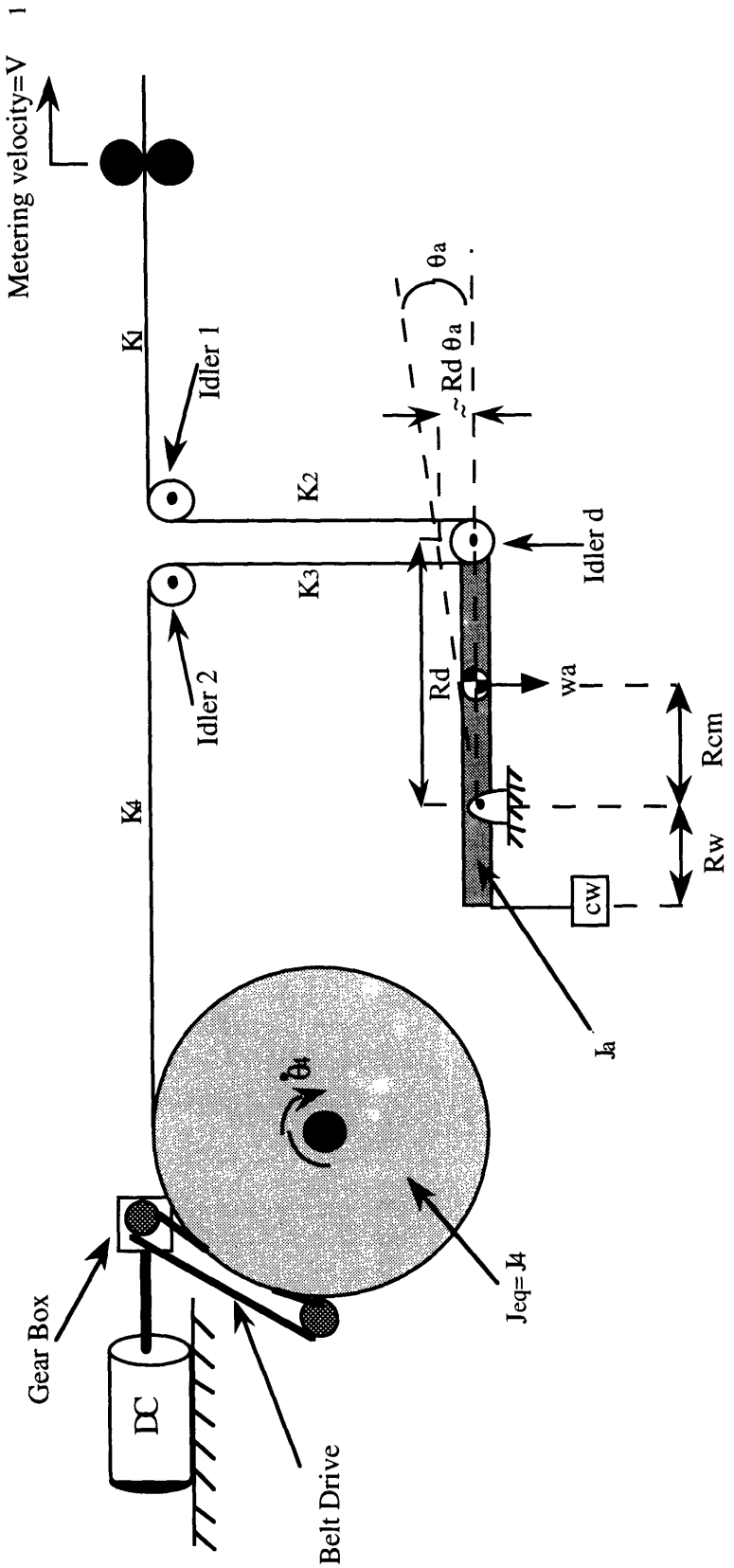

Figure 3.4: Web Unwind Unit Diagram

Where:

- J_1, J_2, J_d, J_a are the inertias of idler 1, idler 2, dancer idler, and dancer arm respectively.

- E is Young's Modulus of the material, A is the cross sectional area, and L is the length of the span, and

- The spring constant for each span is given by:

$$K_n = \frac{EA}{L_n} \tag{3.11}$$

Equations 3.3-3.10 can be rewritten is state space form as the following eighth order system:

$$\dot{\vec{x}} = \mathbf{A}\vec{x} + \mathbf{B}\vec{u} \tag{3.12}$$

Where:

$$\mathbf{A} = \begin{bmatrix} 0 & 0 & 0 & 0 & -K_1 r_1 & 0 & 0 & 0 \\ 0 & 0 & 0 & 0 & -K_2 r_1 & -K_2 r_d & 0 & -K_2 R_d \\ 0 & 0 & 0 & 0 & 0 & K_3 r_d & -K_3 r_2 & -K_3 R_d \\ 0 & 0 & 0 & 0 & 0 & 0 & K_4 r_2 & 0 \\ \frac{r_1}{J_1} & -\frac{r_1}{J_1} & 0 & 0 & -\frac{b_1}{J_1} & 0 & 0 & 0 \\ 0 & \frac{r_d}{J_d} & -\frac{r_d}{J_d} & 0 & 0 & -\frac{b_d}{J_d} & 0 & 0 \\ 0 & 0 & \frac{r_2}{J_2} & -\frac{r_2}{J_2} & 0 & 0 & -\frac{b_2}{J_2} & 0 \\ 0 & \frac{R_d}{J_a} & \frac{R_d}{J_a} & 0 & 0 & 0 & 0 & -\frac{b_a}{J_a} \end{bmatrix}$$

$$\mathbf{B} = \begin{bmatrix} K_1 & 0 & 0 & 0 \\ 0 & 0 & 0 & 0 \\ 0 & 0 & 0 & 0 \\ 0 & -K_4 & 0 & 0 \\ 0 & 0 & 0 & 0 \\ 0 & 0 & 0 & 0 \\ 0 & 0 & 0 & 0 \\ 0 & 0 & \frac{R_w}{J_a} & -\frac{R_{cm}}{J_a} \end{bmatrix}$$

The state vector is given by the four tensions in the spans and the four angular velocities of the rotational inertias. The input vector contains the velocity of the web being supplied into the system (linear velocity of the web leaving the roll), the metering velocity and two constants (the weight of the dancer arm and the counter weight of the dancer). These vectors are:

$$\vec{x} = \begin{bmatrix} F_{K1} \\ F_{K2} \\ F_{K3} \\ F_{K4} \\ \dot{\theta}_1 \\ \dot{\theta}_d \\ \dot{\theta}_2 \\ \dot{\theta}_a \end{bmatrix} \qquad \text{and} \qquad \vec{u} = \begin{bmatrix} Vo \\ V_1 \\ c_w \\ w_a \end{bmatrix}$$

The output equation for the system is given by:

$$\vec{\mathbf{y}} = \mathbf{C}\dot{\mathbf{x}} + \mathbf{D}\vec{\mathbf{u}} \tag{3.13}$$

Where:

$$\mathbf{C} = \begin{bmatrix} 1 & 0 & 0 & 0 & 0 & 0 & 0 & 0 \\ 0 & 1 & 0 & 0 & 0 & 0 & 0 & 0 \\ 0 & 0 & 1 & 0 & 0 & 0 & 0 & 0 \\ 0 & 0 & 0 & 1 & 0 & 0 & 0 & 0 \\ 0 & 0 & 0 & 0 & r_1 & 0 & 0 & 0 \\ 0 & 0 & 0 & 0 & 0 & r_d & 0 & 0 \\ 0 & 0 & 0 & 0 & 0 & 0 & r_2 & 0 \\ 0 & 0 & 0 & 0 & 0 & 0 & 0 & 1 \end{bmatrix} \qquad \text{and} \qquad \mathbf{D} = [0]$$

The output Equation 3.13 gives as outputs the four tensions in the spans, the linear velocity of the web through idlers 1,2, and d and the angular velocity of the dancer arm. Note that D is a 4x8 matrix of zeros.

3.3 Non-Linear Lumped Parameter Model

3.3.1 Prototype Unwind Unit Description

A non-linear lumped parameter model was developed for a prototype unwind unit. The model accounts for material and geometric non-linearities and as will be shown in Chapter 6, matches experimental data more accurately than the linear model. The prototype unit differs from the production unit in several ways. First, the geometric configuration is different with the dancer arm oriented perpendicular rather than parallel to the floor. Second, the dancer arm does not have a counter weight, but rather a pneumatic piston that "pre-tensions" the material like the counter weight does in the production unit. Third, the web path is different with the prototype unit having eight rather than four spans, thus allowing for greater web accumulation. Finally, the prototype unit has a digital rather than an analog control system including a resolver instead of a potentiometer to measure dancer position.

A diagram of the prototype unit is shown in Figure 3.5.

3.3.2 Non-linear Dancer Spans Model

One of the major assumptions made in the dancer model developed in Section 3.2 (other than geometric non-linearities) is that the spring constant (K) of the dancer spans does not change as the dancer moves. However, from Equation (3.11) it is obvious that the dancer spans' spring constants are inversely proportional to the dancer length. That is, as the dancer moves the effective elasticity of the web it holds decreases or increases. Taking the complete derivative of Equation (3.1) we find:

$$\dot{F} = \dot{K}'x + K'\frac{dx}{dt} \tag{3.14}$$

Where: $K' = \frac{EA}{L}$.

In the case of the spans in the dancer the length L is given by:

$$\begin{aligned} L_n &= l_{n_o} - R_n \sin\theta_a \\ L_n &\approx l_{n_o} - R_n\theta_a \qquad \text{for small } \theta_a \end{aligned} \tag{3.15}$$

Where ln_o is the initial length of the span and R_n is the distance from the pivot point of the dancer to the location of the span. It has been assumed that the approximation in Equation (3.15) is valid because the maximum dancer angle is approximately 30 degrees. However, as will be discussed further, other geometric non-linearities have been considered. Appendix B includes calculations of the lengths of spans as a function of dancer displacement which justify these approximations.

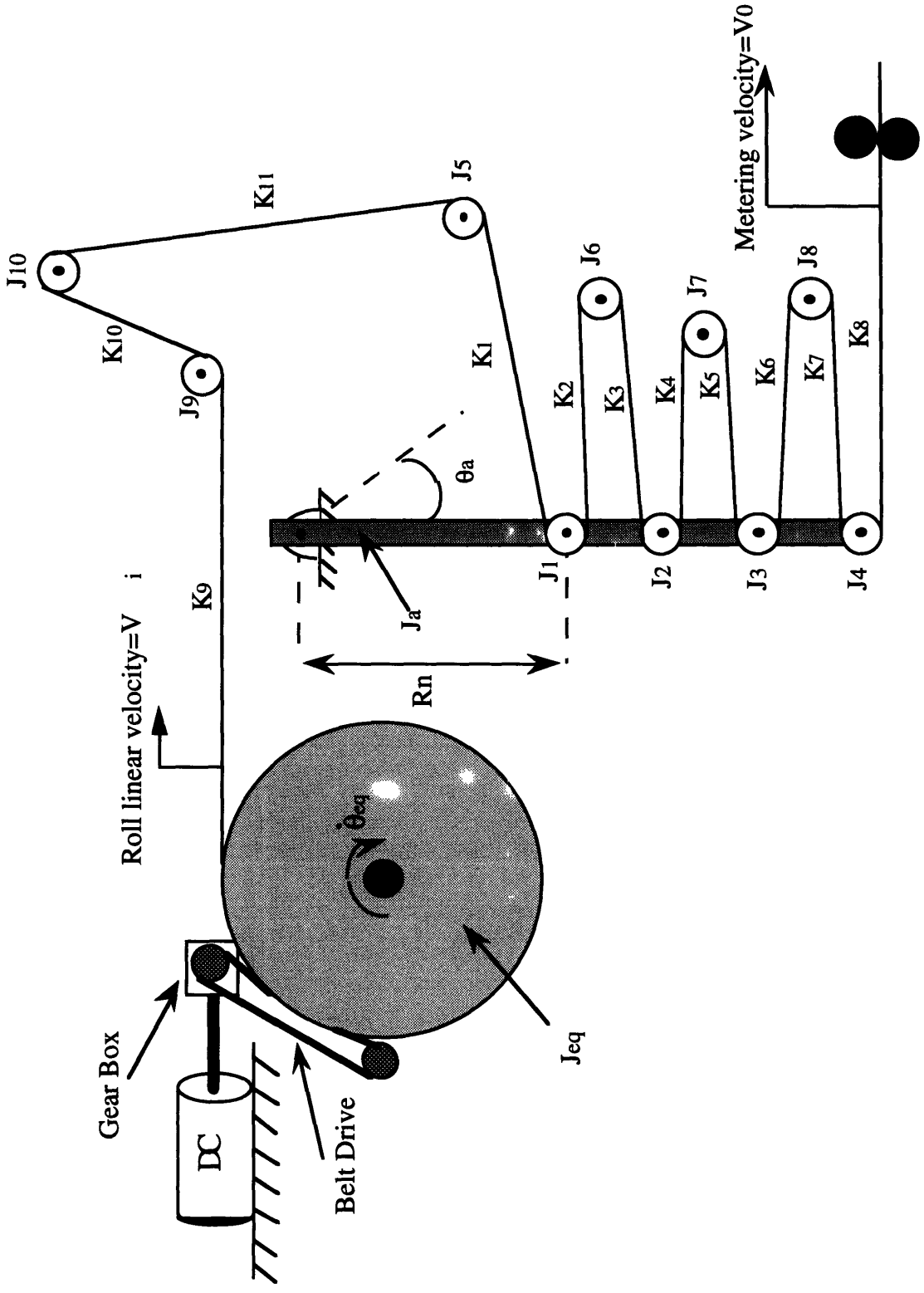

Figure 3.5: Prototype Unwind Unit Schematic

Substituting Equation (3.15) into Equation (3.14):

$$\dot{F} = \frac{d}{dt}\left(\frac{EA}{l_{n_o} - R_d}\right)x + \left(\frac{EA}{l_{n_o} - R_d}\right)\frac{dx}{dt} \tag{3.16}$$

Using the quotient rule to take the time derivative of the first term and assuming EA and ln_o do not change over time:

$$\begin{aligned} \frac{d}{dt}\left(\frac{EA}{l_{n_o} - R_n\theta_a}\right) &= \frac{\left(l_{n_o} - R_n\theta_a\right)\frac{d}{dt}(EA) - EA\left(\dot{l}_{n_o} - R_n\dot{\theta}_a\right)}{\left(l_{n_o} - R_n\theta_a\right)^2} \\ \frac{d}{dt}\left(\frac{EA}{l_{n_o} - R_n\theta_a}\right) &= \frac{EA\left(R_n\dot{\theta}_a\right)}{\left(l_{n_o} - R_n\theta_a\right)^2} \end{aligned} \tag{3.17}$$

Note that in Equation (3.17) it has been assumed that the modulus and cross-sectional area of the material do not change over time. However, if the material is highly viscoelastic (modulus changes significantly over time), the first term of the equation would have to be included.

Substituting Equation (3.17) into Equation (3.16):

$$\dot{F} = \left(\frac{EA}{l_{n_o} - R_n\theta_a}\right)\left[\frac{dx}{dt} + \left(\frac{R_n\dot{\theta}_a}{l_{n_o} - R_n\theta_a}\right)x\right] \tag{3.18}$$

Equation (3.18) is analogous to Equation (3.2) if we consider that the left term to be the equivalent spring constant, which is now a function of time, that is K=K(t), and that there is an additional term dependent on the position rather than the velocity across the spring. Also note that if viscoelasticity is considered, then Equation (3.18) can be expressed as:

$$\dot{F} = \left(\frac{EA}{l_{n_o} - R_n\theta_a}\right)\left[\frac{dx}{dt} + \left(\frac{R_n\dot{\theta}_a}{l_{n_o} - R_n\theta_a}\right)x\right] + \left(\frac{\frac{d}{dt}(EA)}{l_{n_o} - R_n\theta_a}\right)x \tag{3.19}$$

In the case of the dancer spans (assuming small angle displacement), the velocity across the modeled non-linear spring is:

$$\frac{dx}{dt} = r_{out}\dot{\theta}_{out} - r_{in}\dot{\theta}_{in} - R_n\dot{\theta}_a \tag{3.20}$$

Similarly, the position across the spring is:

$$x = r_{out}\theta_{out} - r_{in}\theta_{in} - R_n\theta_a \tag{3.21}$$

In both cases the subscript $_{out}$ refers to the idler at the end of the span (whose displacement increases tension) and the subscript $_{in}$ refers to the idler at the beginning of the span.

Equations (3.18) (3.20) and (3.21) are implemented in software using *Simulink*® [2]. The corresponding block diagram is shown in Figure 3.6. Note that this block diagram is not a universal block diagram from control theory, but rather a graphical representation of a state space system in the *Simulink*® environment.

The figure corresponds to span #1 where V_1 is the velocity out of the first idler in the dancer V_5 is the velocity out of the first fixed idler and V_{a1} is the linear velocity of the first idler as the dancer arm swings. Notice subscripts are the only change from span to span and the same model applies to all spans (K1-K8 in Figure 3.5).

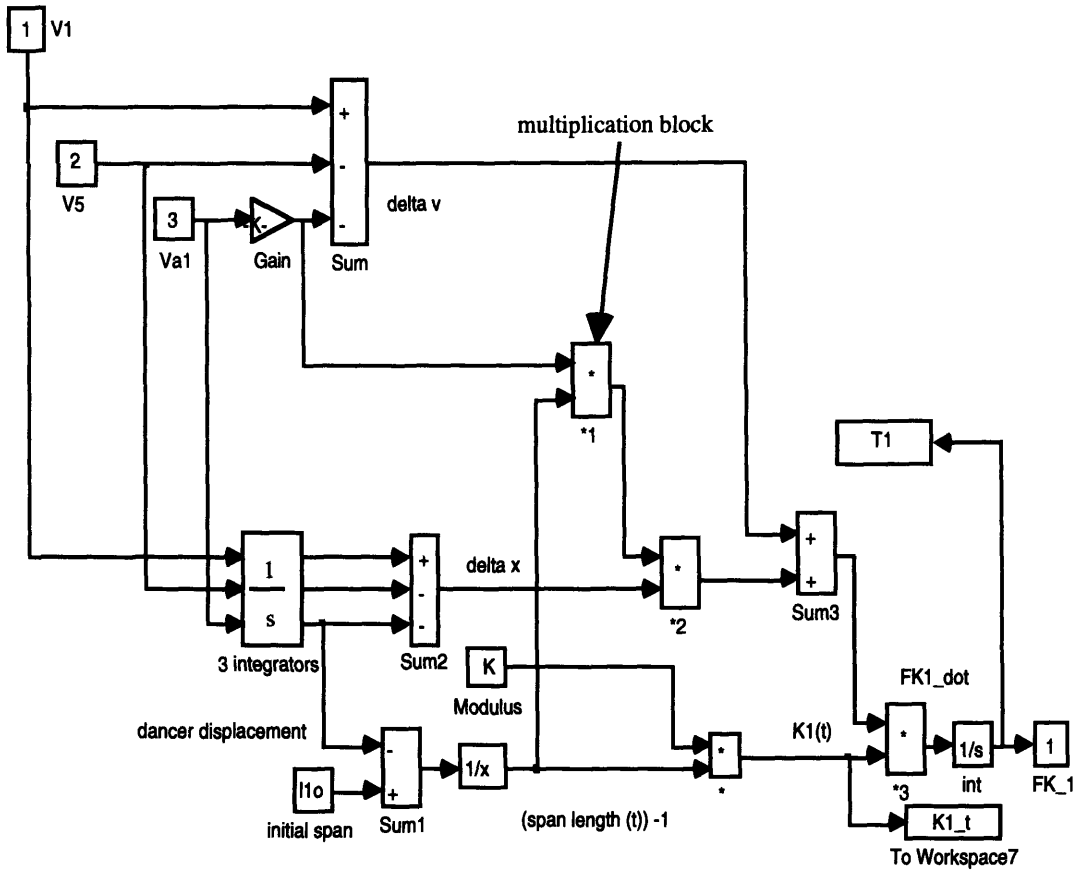

Figure 3.6: *Simulink*® Block Diagram of a Non-Linear Dancer Span

[2] *Simulink*® is a dynamics and control system design simulation software produced by *The MathWorks Inc.*

3.3.3 Spans and Idlers Linear Model

Modeling the spans as discrete springs and the idlers as inertias with bearing damping, a three span, two idler model for the elements prior to the dancer (J_9, J_{10}, K_9-K_{11} in Figure 3.5.) has the following state-space representation.

$$\begin{aligned} \dot{\vec{x}}_1 &= \mathbf{A_1}\vec{x}_1 + \mathbf{B_1}\vec{u}_1 \\ \vec{y}_1 &= \mathbf{C_1}\vec{x}_1 + \mathbf{D_1}\vec{u}_1 \end{aligned} \tag{3.22}$$

Where, the state, input and output vectors are given by:

$$\vec{x}_1 = \begin{bmatrix} F_{K_9} \\ F_{K_{10}} \\ F_{K_{11}} \\ \dot{\theta}_9 \\ \dot{\theta}_{10} \end{bmatrix} \qquad \vec{u}_1 = \begin{bmatrix} V_5 \\ V_i \end{bmatrix} \qquad \vec{y}_1 = \begin{bmatrix} F_{K_9} \\ F_{K_{10}} \\ F_{K_{11}} \\ V_9 \\ V_{10} \end{bmatrix}$$

Similarly the matrices of Equation (3.22) are:

$$\mathbf{A_1} = \begin{bmatrix} 0 & 0 & 0 & K_9 r_9 & 0 \\ 0 & 0 & 0 & -K_{10} r_9 & K_{10} r_{10} \\ 0 & 0 & 0 & 0 & -K_{11} r_{10} \\ -\frac{r_9}{J_9} & \frac{r_9}{J_9} & 0 & -\frac{b_9}{J_9} & 0 \\ 0 & -\frac{r_{10}}{J_{10}} & \frac{r_{10}}{J_{10}} & 0 & -\frac{b_{10}}{J_{10}} \end{bmatrix} \qquad \mathbf{B_1} = \begin{bmatrix} 0 & -K_9 \\ 0 & 0 \\ K_{11} & 0 \\ 0 & 0 \\ 0 & 0 \end{bmatrix}$$

$$\mathbf{C_1} = \begin{bmatrix} 1 & 0 & 0 & 0 & 0 \\ 0 & 1 & 0 & 0 & 0 \\ 0 & 0 & 1 & 0 & 0 \\ 0 & 0 & 0 & r_9 & 0 \\ 0 & 0 & 0 & 0 & r_{10} \end{bmatrix} \qquad \mathbf{D_1} = \begin{bmatrix} 0 & 0 \\ 0 & 0 \\ 0 & 0 \\ 0 & 0 \\ 0 & 0 \end{bmatrix}$$

In this model, V_i and V_5 are respectively, the linear web speed leaving the roll and the linear web speed of the web going over the first stationary idler of the dancer. Also note that the radius r_n correspond to the radius of the idlers J_n.

3.3.4 Fixed Idlers and Moving Idlers Models

In the dancer model in Section 3.2 the span tensions that produce the torque that accelerates idlers are treated as states in the state space representation of the model. In the current treatment of the non-linear dancer spans, tensions are not considered states for a state space dancer model. They are considered outputs of the non-linear span models and inputs into the idler models because tensions are not linear combinations of the angular velocities and positions of idlers.

If we substitute Equation (3.20) and (3.21) into Equation (3.18) and use the appropriate subscripts, then the force in span #4 is given by:[3]

$$\dot{F}_4 = \left(\frac{EA}{l_{4_o} - R_4\theta_a}\right)\left[r_7\dot{\theta}_7 - r_2\dot{\theta}_2 - R_4\dot{\theta}_a + \left(\frac{R_4\dot{\theta}_a}{l_{4_o} - R_4\theta_a}\right)\left(r_7\theta_7 - r_2\theta_2 - R_4\theta_a\right)\right] \quad (3.23)$$

Notice that Equation (3.23) cannot be expressed as part of a matrix with constant coefficients because it is a non-linear function of the system's states. For example, the first terms of the equation include the idler angular velocities (states) in the numerator and the dancer angular position (another state) in the denominator.

Thus, these idler models have the following state-space form with the span forces as inputs from non-linear blocks:

$$\begin{aligned} \dot{\vec{\mathbf{x}}}_2 &= \mathbf{A}_2\vec{\mathbf{x}}_2 + \mathbf{B}_2\vec{\mathbf{u}}_2 \\ \vec{\mathbf{y}}_2 &= \mathbf{C}_2\vec{\mathbf{x}}_2 + \mathbf{D}_2\vec{\mathbf{u}}_2 \end{aligned} \quad (3.24)$$

The state, input, and output vectors of Equation (3.24) are given by:

$$\vec{\mathbf{x}}_2 = \begin{bmatrix} \dot{\theta}_1 \\ \dot{\theta}_2 \\ \dot{\theta}_3 \\ \dot{\theta}_4 \end{bmatrix} \qquad \vec{\mathbf{u}}_2 = \begin{bmatrix} F_1 \\ F_2 \\ F_3 \\ F_4 \\ F_5 \\ F_6 \\ F_7 \\ F_8 \end{bmatrix} \qquad \vec{\mathbf{y}}_2 = \begin{bmatrix} V_1 \\ V_2 \\ V_3 \\ V_4 \end{bmatrix}$$

[3]The equations for all the other spans can be written in a similar way.

The matrices of the state equations are:

$$\mathbf{A_2} = \begin{bmatrix} \frac{-b_1}{J_1} & 0 & 0 & 0 \\ 0 & \frac{-b_2}{J_2} & 0 & 0 \\ 0 & 0 & \frac{-b_3}{J_3} & 0 \\ 0 & 0 & 0 & \frac{-b_4}{J_4} \end{bmatrix} \quad \mathbf{B_2} = \begin{bmatrix} -\frac{r_1}{J_1} & \frac{r_1}{J_1} & 0 & 0 & 0 & 0 & 0 & 0 \\ 0 & 0 & -\frac{r_2}{J_2} & \frac{r_2}{J_2} & 0 & 0 & 0 & 0 \\ 0 & 0 & 0 & 0 & -\frac{r_3}{J_3} & \frac{r_3}{J_3} & 0 & 0 \\ 0 & 0 & 0 & 0 & 0 & 0 & -\frac{r_4}{J_4} & \frac{r_4}{J_4} \end{bmatrix}$$

$$\mathbf{C_2} = \begin{bmatrix} r_1 & 0 & 0 & 0 \\ 0 & r_2 & 0 & 0 \\ 0 & 0 & r_3 & 0 \\ 0 & 0 & 0 & r_4 \end{bmatrix} \quad \mathbf{D_2} = \begin{bmatrix} 0 & 0 & 0 & 0 & 0 & 0 & 0 & 0 \\ 0 & 0 & 0 & 0 & 0 & 0 & 0 & 0 \\ 0 & 0 & 0 & 0 & 0 & 0 & 0 & 0 \\ 0 & 0 & 0 & 0 & 0 & 0 & 0 & 0 \end{bmatrix}$$

Idlers 1-4 correspond to the four idlers on the dancer while idlers 5-8 correspond to the fixed idlers. For the fixed idlers, the force on the last span is not used as an input. Tension in the span prior to idler 5 (F_{11}) is used instead. Thus the state equations for the fixed idlers are identical in form to Equation (3.24) except that subscripts 1-4 are substituted by subscripts 5-8 and the input vector is:

$$\bar{\mathbf{u}}_3 = \begin{bmatrix} F_{11} & F_1 & F_2 & F_3 & F_4 & F_5 & F_6 & F_7 \end{bmatrix}^T \tag{3.25}$$

The *Simulink*® implementation of the state space system representations is shown in Figure 3.7. Note that this block diagram is not a universal block diagram from modern control theory, but rather a graphical representation of a state space system in the *Simulink*® environment.

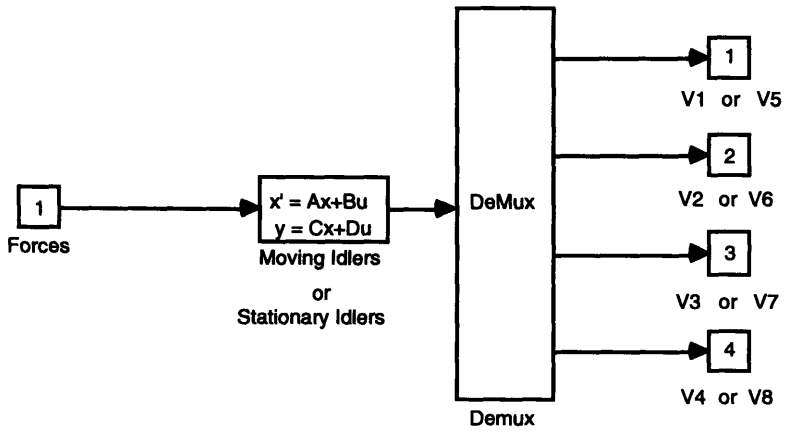

Figure 3.7: *Simulink*® Block Diagram of Idler Models

The "Demux" block in Figure 3.7 is used to separate each of the scalar outputs from vectors $\vec{y}_1$ and $\vec{y}_2$ in Equations (3.22) and (3.24). Similarly, the "Mux" block (shown later in Figure 3.12) is used to combine all of the dancer tensions into a single tension vector.

3.3.5 Geometric non-linearities

Because of the way the system has been configured, the tension in the web does not act perpendicular to the dancer arm. As seen in Figure 3.8 the tension of the web acts at an angle ϕ_n to the dancer arm (the subscript refers to the span number). The three angles shown are related by the following trigonometric relationships:

$$\phi_n = 90 + (\theta_a - \beta_n) \tag{3.26}$$

$$\beta_n = tan^{-1}\left(\frac{y_n - R_n(1 - cos\,\theta_a)}{x_n - R_n(sin\,\theta_a)}\right) \tag{3.27}$$

Thus, the perpendicular component of web tensions is a function of the dancer arm position and is given by:

$$F_n' = F_n\ sin(\phi_n) \tag{3.28}$$

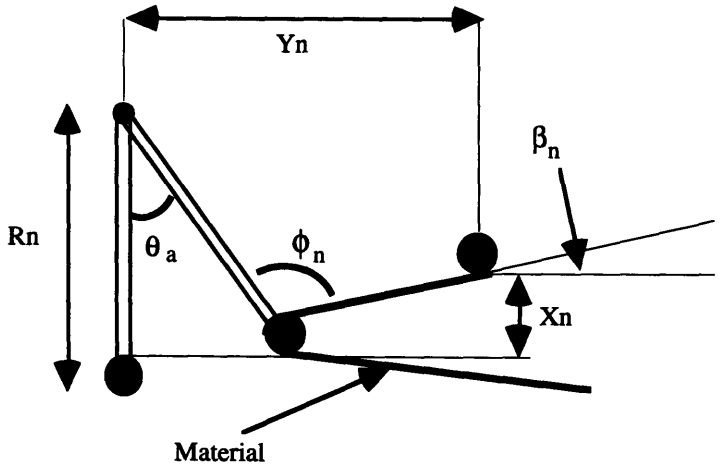

Figure 3.8: Dancer Spans Geometric Non-linearities

The calculation of the perpendicular component of the web tensions is implemented with the block diagrams shown in Figures 3.9 and 3.10. Figure 3.10 is the detailed block used to find the angle β_n.

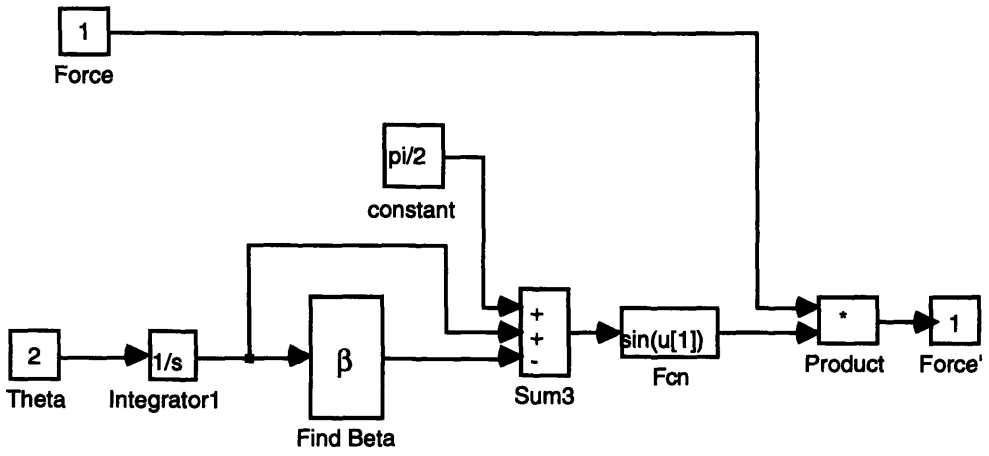

Figure 3.9: Geometric Non-Linearities Block Diagram

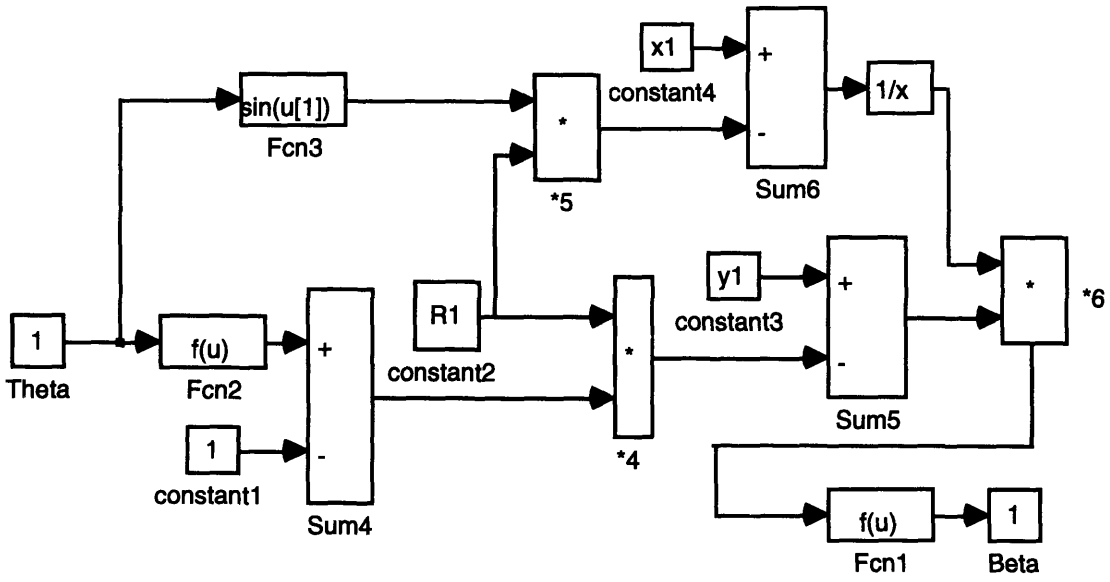

Figure 3.10: Find Beta Block Diagram

3.3.6 Dancer Arm Equation of Motion

Once the component perpendicular to the dancer arm has been calculated (Equation 3.28), it is possible to write an equation for the angular velocity of the dancer arm.

$$\ddot{\theta}_d = \frac{1}{J_d}\left[F_1' R_1 + F_2' R_2 + \ldots F_8' R_8 - b_d \dot{\theta}_d + T_p\right] \tag{3.29}$$

Where:
b_d = the bearing friction on the shaft of the dancer
T_p= the torque applied on the dancer by a pneumatic piston that "pre-tensions" the web.

Using an integrator block as shown in Figure 3.11 Equation (3.29) can be easily solved for θ_a, the angular velocity of the dancer arm.

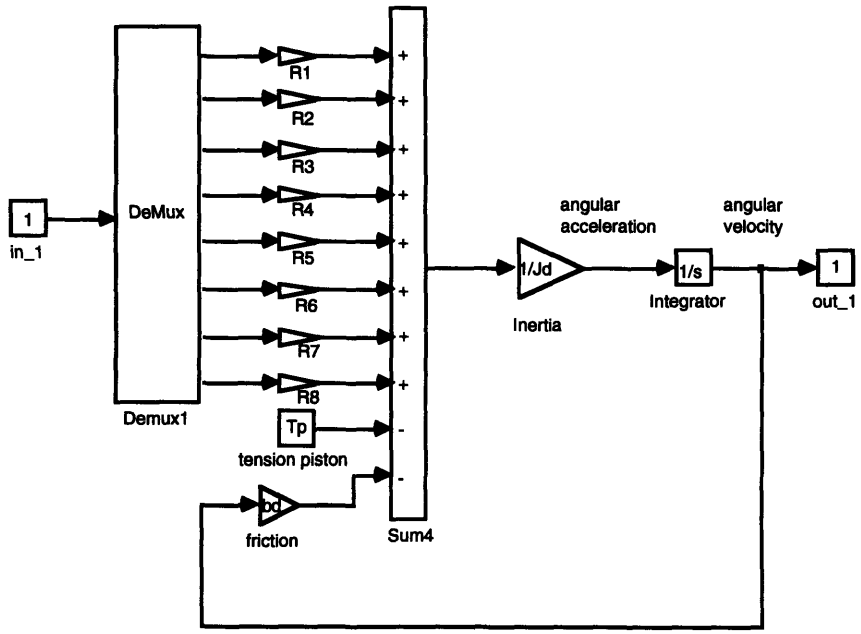

Figure 3.11: Dancer Arm Equation of Motion Implementation

In summary, the prototype unwind unit model has been split into the following blocks:

- Eight non-linear dancer spans (Figure 3.6).
- A linear block for the first three spans and first two idlers (Figure 3.7).
- A linear block for the four fixed idlers (Figure 3.7).
- A linear block for the four moving idlers on the dancer arm (Figure 3.7).
- Eight non-linear geometry blocks that calculate the normal component of the span tension applying a torque on the dancer arm (Figures 3.9 and 3.10).
- A linear block for the dancer arm inertia (Figure 3.11).

Figure 3.12 shows the block diagram of the entire model where all the blocks described in the previous sections are grouped.

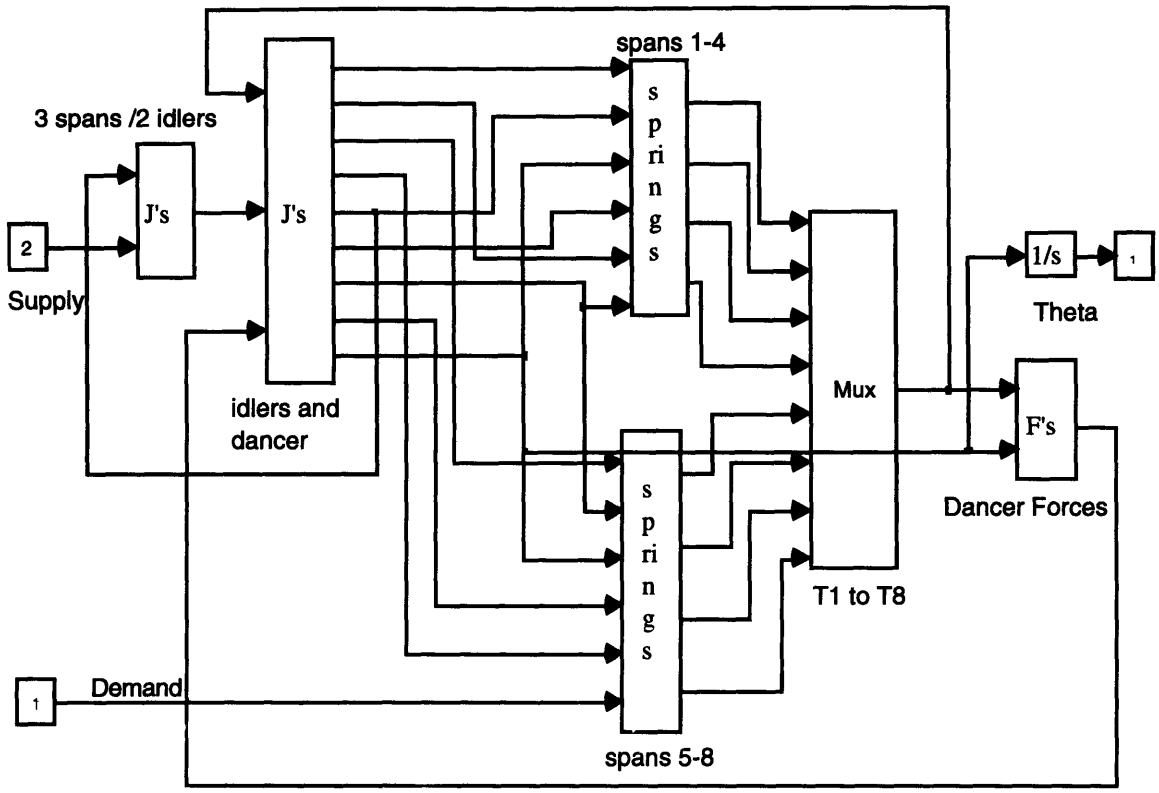

Figure 3.12: Non-linear Prototype Unwind Unit Model

Chapter 4

Comparison of Analog and Digital Control System Platforms

4.1 Analog Web Unwind Control System

The purpose of the unwind system is to supply material from a roll to a main process at the same rate at which it is being metered. If the supply of material lags the demand, tension in the web can become excessive and the material might break. A rupture in the unwind unit can also occur if the inertial and frictional "barriers" the web must overcome are too excessive or out of phase with each other. This will cause local peaks in tension that will exceed the material's tensile strength.

The control system for the unwind equipment is configured as shown in Figure 4.1. The maximum DC speed of the unwind unit is set to a value proportional to the line reference speed of the main process. That is, if the main process operates at a rate that requires x m/s of material to be metered, the target value for the DC motor speed is K*x, where K is a constant such that the motor will unwind material at x m/s. To insure that the unwind speed follows the main line reference, velocity feedback from the DC motor tachometer is used.

The velocity feedback loop is complemented with an outside loop for the dancer position. Because the web has to overcome the inertia of the idlers and the friction in the idler bearings, there are occasions when the material required by the process has to be given up by the dancer. This occurs when the material unwound from the roll lags the material required at the metering point. This lag results in an increase in tension that causes the dancer to rise and give up material. As the dancer rises, an error signal is generated. This error trims the velocity feedback loop of the motor, and the motor speeds up to replenish the web in the dancer. The opposite can also occur; too much web is being supplied, tension decreases, the dancer falls and the motor slows down so that web will be used up and the dancer will return to its target position.

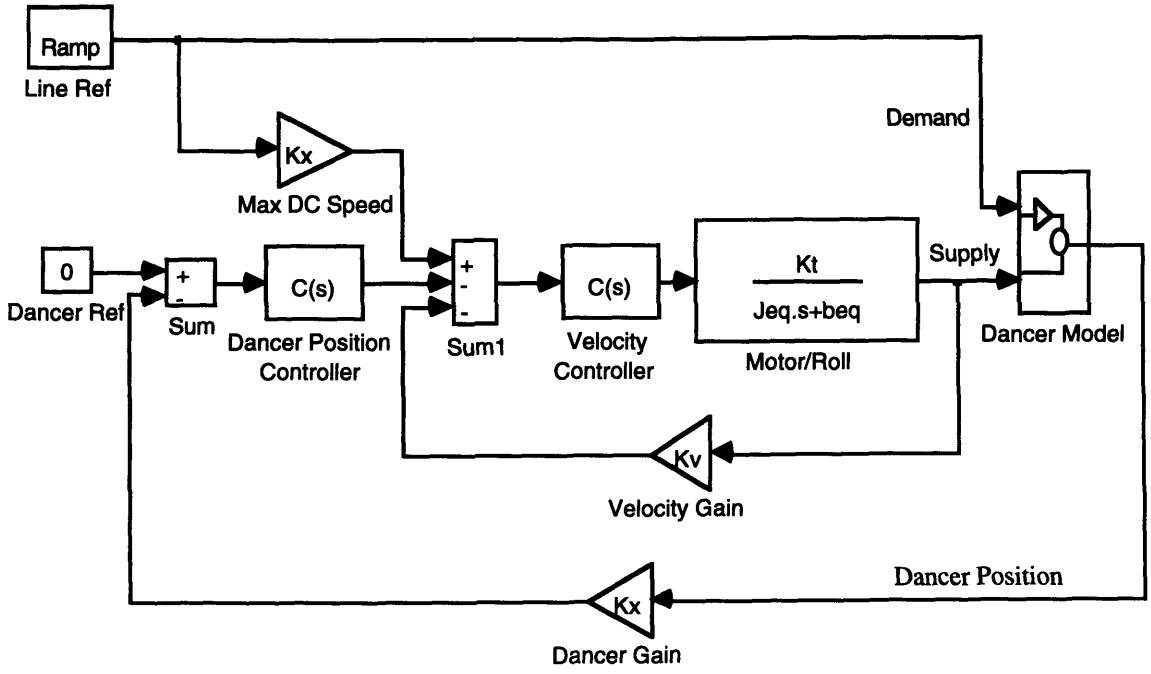

Figure 4.1: Analog Control System / Linear Model Block Diagram

4.2 Digital Web Unwind Control System

Figure 4.2 shows a block diagram of the prototype unwind unit with a digital controller. The prototype unwind unit includes a digital control system that incorporates an additional feedback loop to the control system block diagram. The purpose of this additional loop is to have the unwind motor *position* (not only the velocity) follow the main reference signal. This feature along with a dancer with greater storage and a feedforward velocity signal, make this system much more robust than the analog system evaluated in Section 3.2. The digital platform also provides some additional advantages.

The first advantage of the digital control platform is its flexibility. Changes in the system's configuration and implementation of different controller designs are all done in software. The architecture of the controller enables it to easily interact with PLC's and other logic sequences that might be built into a given process of which the unwind unit is part of. Another advantage of the digital controller is that references can be set to precise values. Besides, because the references are set in software, they do not drift over time as with analog controllers. Girgash [3] discusses some of the features of these kind of programmable winder drives in detail.

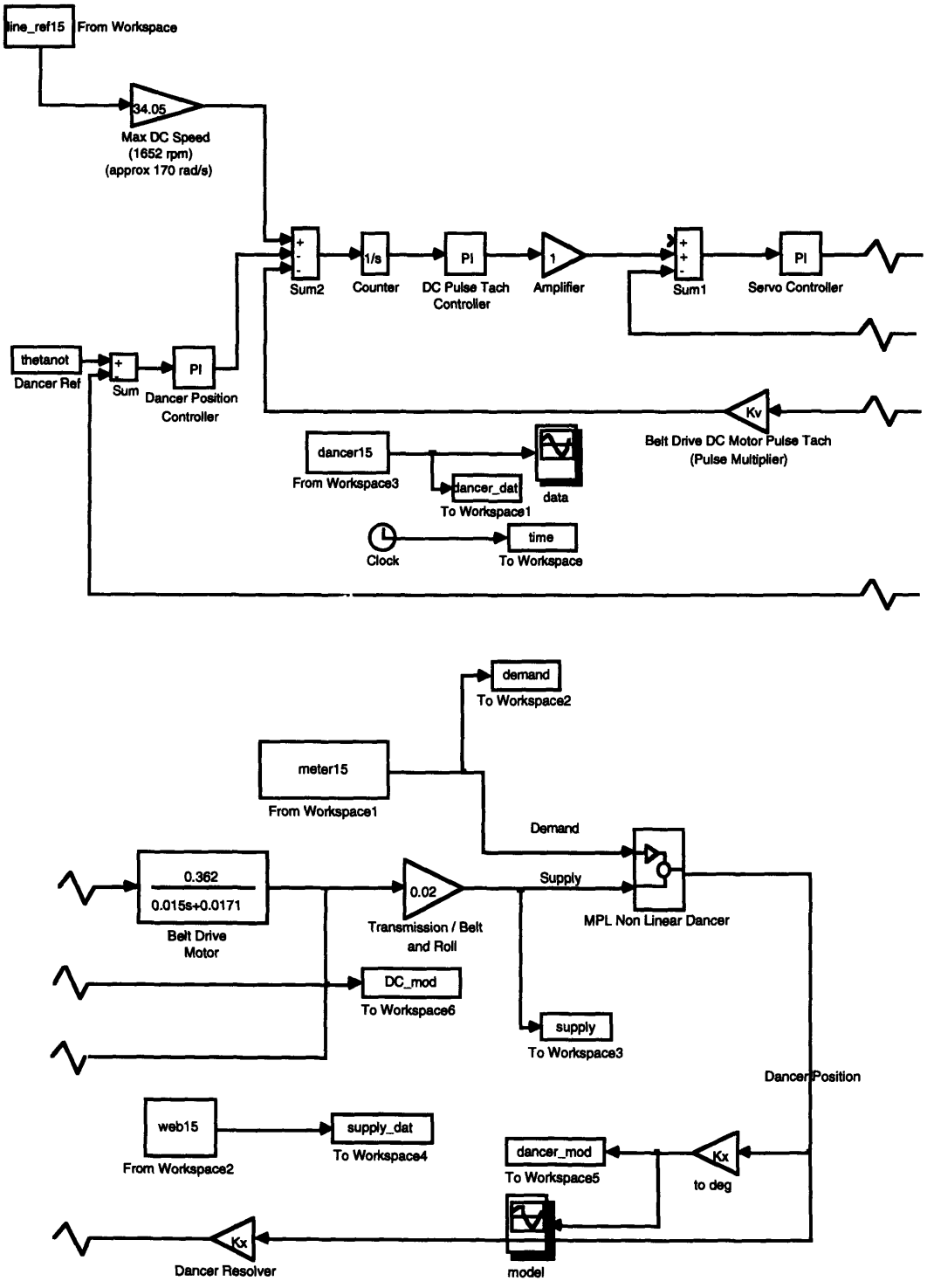

Figure 4.2: Digital Control System Block Diagram

There are two main differences between the prototype unit controller and the analog controllers on production equipment. First, the digital controller has a counter after the first summing junction where tachometer feedback, dancer position feedback and line reference come together. This counter is

effectively an integrator. By integrating the velocity of the line reference and the motors, the system becomes much more sensitive at lower speeds. If the unwind motor is trying to follow a position reference, it can do so even if the velocity signal is very small. Thus the control of the unit during the initial portion of the startup (low speeds) is much better with digital than with analog control.

Secondly, the addition of a feedforward signal and an additional PI controller (pulse tach controller) also enhances the performance of the prototype unit. The feedforward signal makes the system very responsive and allows the supply of web to keep up with the demand, particularly at high speeds or in the presence of speed disturbances.

In summary a digital control platform is preferred for the following reasons:

- *Flexibility:* System configuration changes are done in software. PLC and other process functions can easily interface with the controller.
- *Repeatability and Accuracy:* Set points are "exactly" set in software. No drift is present making repeatability of reference signals possible.
- *Position Tracking:* Pulse counter makes system responsive even at low speeds.
- *Feedforward Signal:* Unwind speed is "anticipated". System is responsive to high speeds and speed disturbances.

Chapter 5

Web Dynamics Startup Transient Experimentation

5.1 Production Equipment Experimentation

The characterization of the probabilistic behavior of the unwind equipment and the formulation of an interference model indicate that uncontrolled dynamic transients during startup can be responsible for system failure. In an attempt to correlate system failures to dynamic transients the behavior of the unwind system and controller was evaluated by recording several startups and shutdowns of the production equipment.

Unfortunately, manufacturing procedures and restrictions on testing of production equipment limited experimentation to recording several process variables of interest during the course of normal production. It should be noted that testing was performed on production equipment that on the average runs at an efficiency of 90% or higher. Thus, the amount of data collected was limited. In fact, only seven startup attempts were recorded in two shifts of production and in none of the cases did tension become so excessive as to break the web. That is, in none of the recorded cases were there any points of the stress distribution that overlapped with the strength distribution of the system. This fact is unfortunate because the main point of the experimentation was to find some dynamic data for the region of interference.

The process parameters recorded where: DC motor speed, dancer position, dancer error (that is, the output of the dancer controller unit), line reference signal, and linear web speed at the first span downstream of the dancer. Note that it was possible to record the linear web speed by using an optical non-contact sensor similar to the ones used in automobile test tracks. [1]

[1] The device uses a prismatic grating that produces a frequency signal from the light reflected on the moving surface. It is manufactured by SEIK Optics.

5.1.1 Line Reference and Motor Speed Time Traces

Figure 5.1 shows a plot of the angular speeds of the line reference and the DC motor.

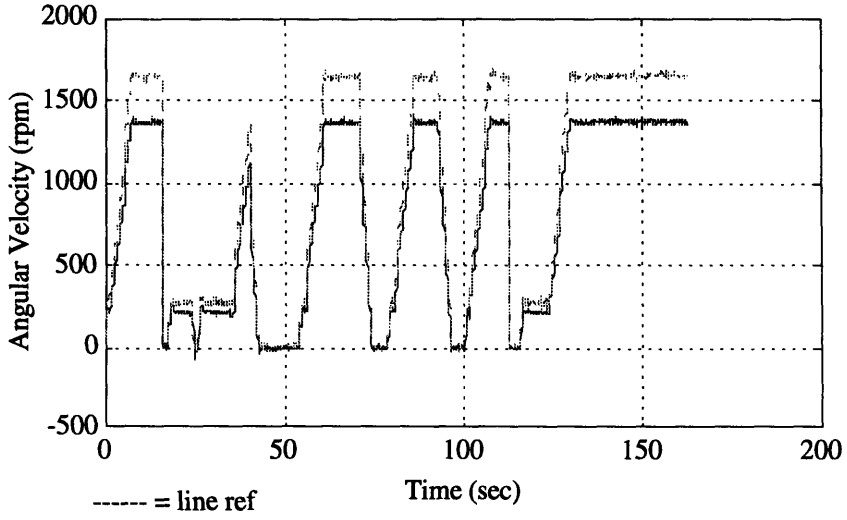

Figure 5.1a: Line Reference and Unwind DC Motor Angular Velocities

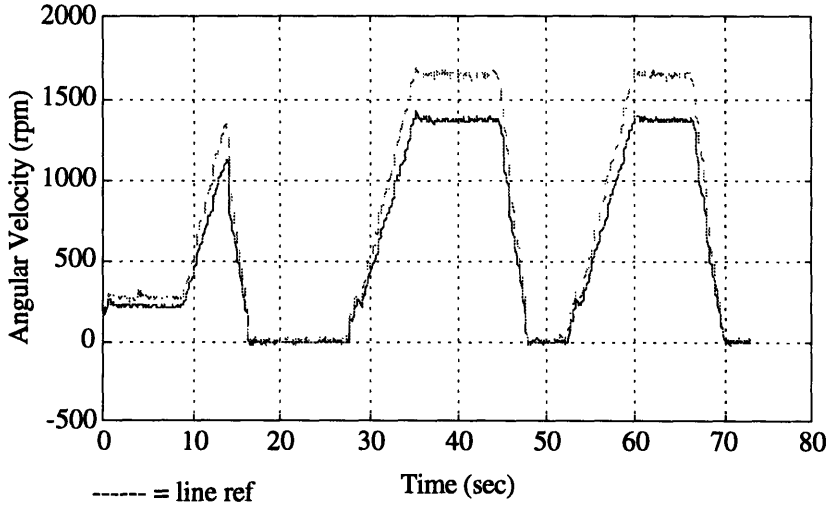

Figure 5.1b: Angular Velocity Startups No. 3, No. 4 and No. 5

Notice that startup No. 3 was a false start of approximately 8 seconds in duration. It was not, however, due to a failure in the unwind unit.

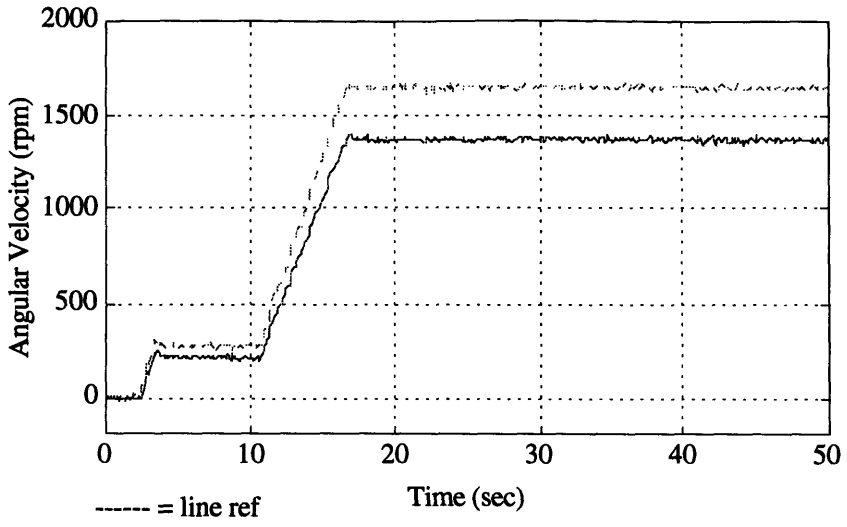

Figure 5.1c: Angular Velocity Startup Transient No. 8

The DC motor follows the main line reference quite accurately. Thus, we can say that the unwind motor does a fairly good job at supplying the system with material. However, we can still notice a minor time lag as seen by the smaller slope of the DC motor curve in the 12-18 second range.

5.1.2 Linear Web Speed Time Traces

The linear speed of the web coming out of the dancer also accurately resembles the ramp-up profile of the line reference. The linear speed of the web during the startup transient in shown in Figure 5.2.

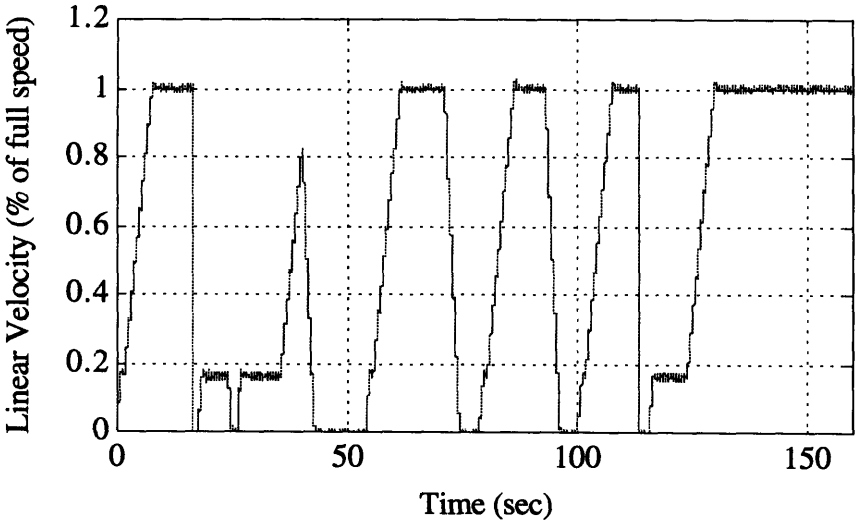

Figure 5.2a: Linear Web Speed During Startup Transients

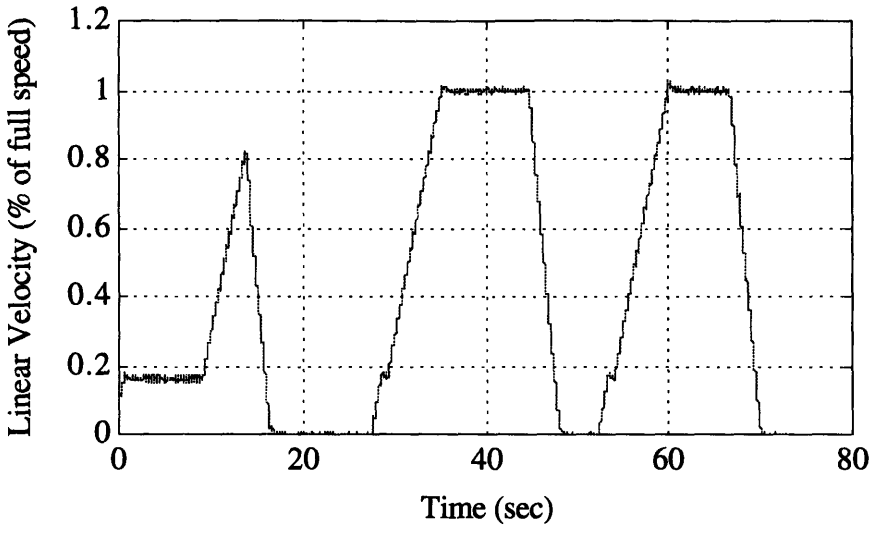

Figure 5.2b: Linear Web Velocity Startups No. 3, No. 4 and No. 5

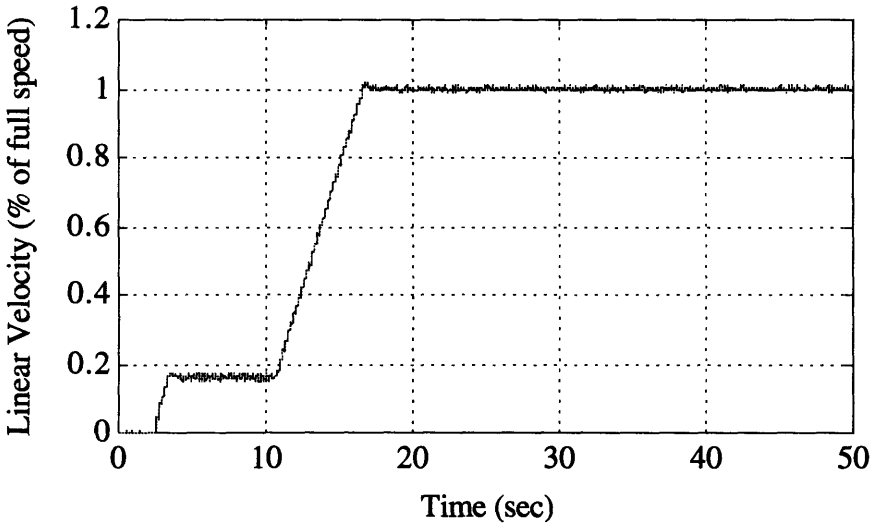

Figure 5.2c: Web Linear Speed During Startup Transient No. 8

Figure 5.2 seems to indicate that the control system is running fairly well and that the tension in the material should not exceed the ultimate tensile strength. However, the fact that about 3% of stop events are due to broken web indicate that there is some localized phenomena where a fracture in the material is induced.

5.1.3 Dancer Position Time Traces

The dancer motion shown in Figure 5.3 is not in degrees or in radians, but rather in Volts. It was not possible to obtain a calibration curve and the data

shown is the output of the potentiometer attached to the shaft of the dancer arm. It is actually this output voltage that is used as a control signal to trim the DC motor speed. Also shown along with the dancer potentiometer output is the "dancer error". This is the output signal from the PI controller for the dancer's position. This output from the controller actually changes the reference signal for the DC motor depending on whether the dancer is falling or rising. Note that it is common practice in the plant to adjust the gains of the analog controller such that at steady state this error signal goes to zero volts.

Looking at the dancer motion slightly hints on the cause of breaks during startup. The motion is not excessive, but as seen in Figure 5.3 the controller does not do a good job of returning the dancer to its target position after every transient. Thus, there is the possibility that on some occasions the dancer initial position is too high and there is not enough web accumulated to withstand the transient. If this is compounded with a large roll (large inertia seen by the motor), excessive bearing drag, and a localized defect in the material it is more likely that the web will break.

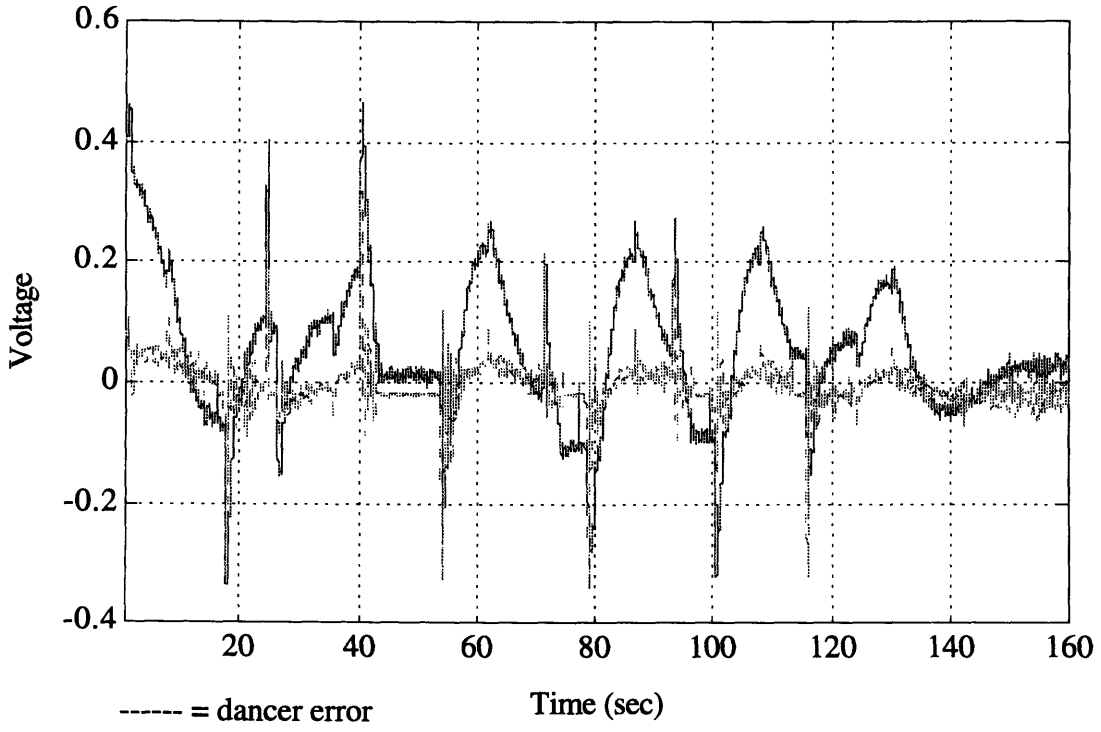

Figure 5.3a: Dancer Potentiometer Output and Dancer Error

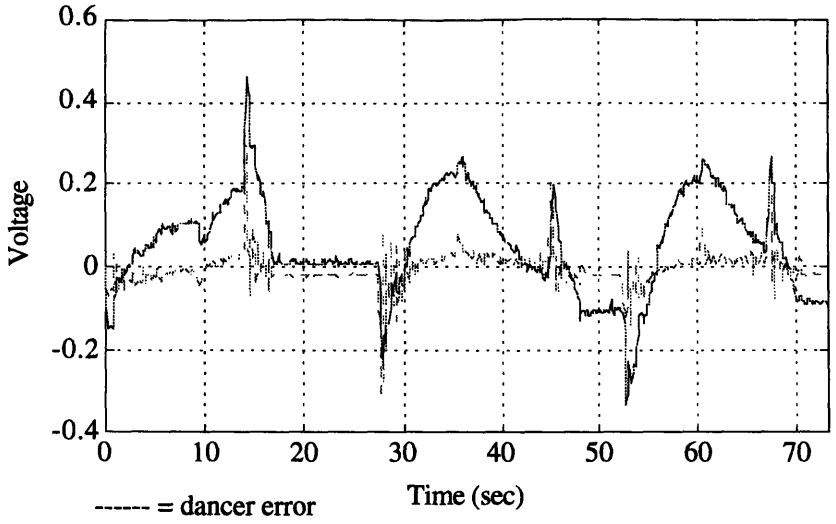

Figure 5.3b: Dancer Motion and Dancer Error During Startups No. 3, No.4 and No.5

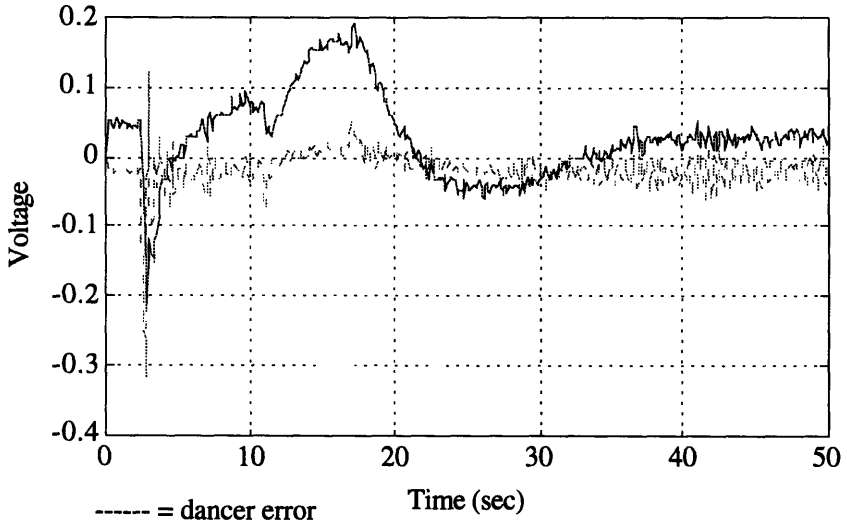

Figure 5.3c: Dancer Motion and Dancer Error During Startups No. 8

The last startup was selected to be used as a validation data set for the linear model described in Chapter 3. This startup is the longest of the ones recorded and did permit the dancer motion to reach steady state as seen in Figure 5.3c. Notice that the duration of the dancer transient is approximately of one minute and coincides with the sharp decrease of the hazard function for the process as mentioned in Chapter 2.

Note that at the beginning of each startup there is a sharp downward peak in the potentiometer's signal. It is possible that this peak occurs because the integrator in the dancer PI controller is not functioning adequately. Given that the controller is analog, it is possible that the capacitor in the circuit is getting discharged.

5.2 Design of Experiments on Prototype Unwind System

A prototype unwind equipment similar to the one tested at the plant was used to conduct a designed experiment. The absence of production schedules made it possible to obtain a large amount of data and also to vary running conditions of the equipment. In a control system sense, the designed experiment is analogous to testing the performance of the closed loop system for a fixed controller setting and a varying plant.

A four variable experiment was performed. The four variables selected were:

- Roll radius -- to determine the effect of a changing inertia on the system.
- Ramp-up time -- to determine the effect of rapid and slow accelerations.
- Belt Loading -- to determine the "rigidity" of the transmission. (belt loading is the pressure of a pneumatic piston that pushes the belt against the roll to insure there is enough surface contact)
- Dancer Initial Position -- to determine the effect of non-linearities and different amounts of stored web.

A full factorial 16 run experiment with two center points was conducted. Table 5.1 summarizes the randomized test run conditions.

Test No.	Pattern	Roll Radius	Line Ref.	Belt Load	Dancer I.C.
DOX 1	+ + - +	0.44 m	1.5 sec	0 psi	1717 count
DOX 2	+ + - -	0.44 m	1.5 sec	0 psi	2317 count
DOX 3	+ - - -	0.44 m	4.5 sec	0 psi	2317 count
DOX 4	+ - - +	0.44 m	4.5 sec	0 psi	1717 count
DOX 9	0 0 0 0	0.31 m	3 sec	10 psi	2017 count
DOX 18	0 0 0 0	0.31 m	3 sec	10 psi	2017 count
DOX 5	- + + +	0.18 m	1.5 sec	20 psi	1717 count
DOX 6	- + - -	0.175 m	1.5 sec	0 psi	2317 count
DOX 7	- + + -	0.175 m	1.5 sec	20 psi	2317 count
DOX 8	- - + -	0.17 m	4.5 sec	20 psi	2317 count
DOX 10	+ + + +	0.46 m	1.5 sec	20 psi	1717 count
DOX 11	+ - + -	0.45 m	4.5 sec	20 psi	2317 count
DOX 12	+ - + +	0.445 m	4.5 sec	20 psi	1717 count
DOX 13	+ + + -	0.435 m	1.5 sec	20 psi	2317 count
DOX 17	- + - +	0.15 m	1.5 sec	0 psi	1717 count
DOX 14	- - - +	0.15 m	4.5 sec	0 psi	1717 count
DOX 15	- - + +	0.145 m	4.5 sec	20 psi	1717 count
DOX 16	- - - -	0.14 m	4.5 sec	0 psi	2317 count

Table 5.1: Designed Experiment Run Conditions

It should be noted that the first four runs were done with the wrong dancer initial condition. The patterns that should have been run and the corresponding dancer initial conditions are:

Test No.	Pattern	Roll Radius	Line Ref.	Belt Load	Dancer I.C.
DOX1	+ + - -	0.44 m	1.5 sec	0 psi	2317 count
DOX2	+ + - +	0.44 m	1.5 sec	0 psi	1717 count
DOX3	+ - - +	0.44 m	4.5 sec	0 psi	1717 count
DOX4	+ - - -	0.44 m	4.5 sec	0 psi	2317 count

The dancer initial condition corresponds to the initial angle and set point of the dancer arm. The initial condition is given in resolver counts where one revolution of the resolver equals 4096 counts and 2017 counts is equal to an angle of zero degrees (dancer perpendicular to the floor). There is a 2:1 gear ratio between the resolver and the actual dancer shaft, so the equation that relates the number of counts to dancer angle is:

$$\theta = \frac{-(\text{count} - 2017)(360)}{(2)(4096)} \tag{5.1}$$

Three variables were selected as outputs of the model. These variables are:

- *Maximum ΔV (m/s)*, that is, the maximum velocity difference between the measured linear web speed and the metering speed. Given that web tension could not be measured directly, it is assumed that tension is directly correlated to this velocity difference.

- *Maximum Web Speed Overshoot (%).* This is a measure of the system's ability to supply "just enough" web and the response of the motor and controller to different process parameters, that is, changes in the plant. It should be mentioned that the gains in the controllers were intentionally mis-tuned so that the dynamic transients in the web and the dancer motion would be more noticeable. This de-tuning procedure included disabling the feedforward signal from the main line reference to the pulse tach controller.

- *Dancer Settling Time (sec).* This time is a measure of the amount of damping in the system and the time required to reach steady state. Note that on most runs collected, the dancer had not completely settled when the data acquisition system was disabled. However, the range of dancer motion was minimum and in fact almost negligible to the naked eye. Therefore, the dancer settling time was defined as the time required for the dancer to cross over its initial position.

During the actual testing several of the run conditions were duplicated. A total of 30 runs were collected. The run conditions and output variables values are summarized in Table 5.2.

Some notes for the table are:

Note #1: Wrong dancer IC should have been 2317 ++--
Note #2: Wrong dancer target.
Note #3: Forgot to switch to small roll
Note #4: Repeat with small roll

Run #	Pattern	Roll Radius (m)	Ramp Time (sec)	Load (psi)	Dancer IC (counts)	Comment	Max Web Speed (m/s)	ss Web Speed (m/s)	Overshoot (%)	Max Delta V (m/s)	Dancer Time (sec)
DOX1	++-+	0.44	1.5	0	1717	Note #1	5.9954	5.075	18.14	2.1927	5.774
DOX2	++--	0.44	1.5	0	2317		5.951	5.0792	17.16	2.5316	6.4756
DOX3	+---	0.44	4.5	0	2317		5.5114	5.0481	9.18	1.3169	6.5713
DOX4	+--+	0.44	4.5	0	1717		5.5195	5.0487	9.33	1.3256	7.2482
DOX9	0000	0.31	3	10	2017		5.5558	4.9657	11.88	0.92805	5.8696
DOX 18	0000	0.31	3	10	2017		5.5558	4.9826	11.50	1.3764	6.1248
DOX9	0000	0.31	3	10	2017		5.5396	4.9783	11.27	1.363	5.7519
DOX 18	0000	0.31	3	10	2017		5.5396	4.976	11.33	1.2952	5.6144
DOX5	-+ + -	0.18	1.5	20	2317	Note #2	5.7614	4.945	16.51	2.4129	7.3369
DOX5	-+++	0.18	1.5	20	1717		1.2402	•	•	6.0021	•
DOX6	- + - -	0.175	1.5	0	2317		5.7453	4.927	16.61	2.2945	6.6407
DOX7	- + + -	0.175	1.5	20	2317		1.2402	•	•	6.0849	•
DOX8	- - + -	0.17	4.5	20	2317		5.3299	4.9056	8.65	1.3714	6.5394
DOX 10	++++	0.46	1.5	20	1717		6.0518	5.0381	20.12	2.9329	5.2635
DOX 11	+ - + -	0.45	4.5	20	2317		5.5517	5.0475	9.99	1.3182	6.3161
DOX 12	+ - + +	0.445	4.5	20	1717		5.5437	5.04	9.99	1.324	6.5713
DOX 13	+ + + -	0.435	1.5	20	2317	Web broke	5.9792	5.0469	18.47	2.2291	9.0256
DOX 14	+ - - +	0.435	4.5	0	1717	Note #3	5.5396	5.1057	8.50	1.389	6.1905
DOX 15	+ - + +	0.435	4.5	20	1717	Note #3	5.5316	5.016	10.28	1.3931	6.1905
DOX 16	+ - - -	0.43	4.5	0	2317	Note #3	5.5074	5.3029	3.86	1.0717	6.37
DOX 16	+ - - -	0.43	4.5	0	2317	Note #3	5.5275	5.01	10.33	1.2975	6.1636
DOX 16	+ - - -	0.43	4.5	0	2317	Note #3	5.5235	5.0271	9.87	1.2956	6.1586
DOX 17	+ + - +	0.425	1.5	0	1717	Note #3	6.0155	•	•	2.5107	3.9835
DOX 17	- + - +	0.15	1.5	0	1717	Note #4	5.8461	5.0827	15.02	2.2182	8.269
DOX 17	- + - +	0.15	1.5	0	1717	Note #4	5.8945	5.0823	15.98	2.3891	9.0276
DOX 14	- - - +	0.15	4.5	0	1717	Note #4	5.4348	5.0595	7.42	1.1401	7.4157
DOX 15	- - + +	0.145	4.5	20	1717	Note #4	5.4832	5.0302	9.01	1.3371	7.2313
DOX 15	- - + +	0.145	4.5	20	1717	Note #4	5.4912	5.0463	8.82	1.2415	7.6878
DOX 16	- - - -	0.14	4.5	0	2317	Note #4	5.4428	5.0672	7.41	1.1542	7.6729
DOX 16	- - - -	0.14	4.5	0	2317	Note #4	5.4348	5.0744	7.10	1.1293	7.5114

Table 5.2: Design of Experiments Results Summary

5.2.1 Maximum Delta V Response Model

The response of the maximum velocity difference between the web unwind and the metering point was evaluated using multiple linear regression analysis. None of the interactions between the four variables being evaluated were significant. Only the roll radius and the ramp time seem to contribute to the response of delta V. Of these two variables, however, the ramp time is much more significant than the roll radius. As seen in the effects test the probability that the effect of roll radius on delta V is due to noise is 27.96%.

The linear model for the maximum delta V is given by:

$$Max\ \delta V = 2.078 + (0.437)\ Roll\ Radius - (0.365)\ Line\ Ramp \qquad (5.2)$$

The statistics on the regression are:

Response: Max delta V (m/s)

Summary of Fit

Rsquare	0.787947
Root Mean Square Error	0.272097
Mean of Response	1.634984
Observations (or Sum Wgts)	28

Parameter Estimates

Term	Estimate	Std Error	t Ratio	Prob>|t|
Intercept	2.7085709	0.18426	14.70	0.0000
Roll Radius (m)	0.4373087	0.39572	1.11	0.2796
Line Ramp (s)	-0.365175	0.03807	-9.59	0.0000

Effect Test

Source	Nparm	DF	Sum of Squares	F Ratio	Prob>F
Roll Radius (m)	1	1	0.0904162	1.2212	0.2796
Line Ramp (s)	1	1	6.8130850	92.0231	0.0000

Analysis of Variance

Source	DF	Sum of Squares	Mean Square	F Ratio
Model	2	6.8776460	3.43882	46.4475
Error	25	1.8509176	0.07404	Prob>F
C Total	27	8.7285636		0.0000

The general trend of the response is captured by the model as seen in Figure 5.4 but the points around the middle of the plot suggest that a non-linear fit might be more adequate.

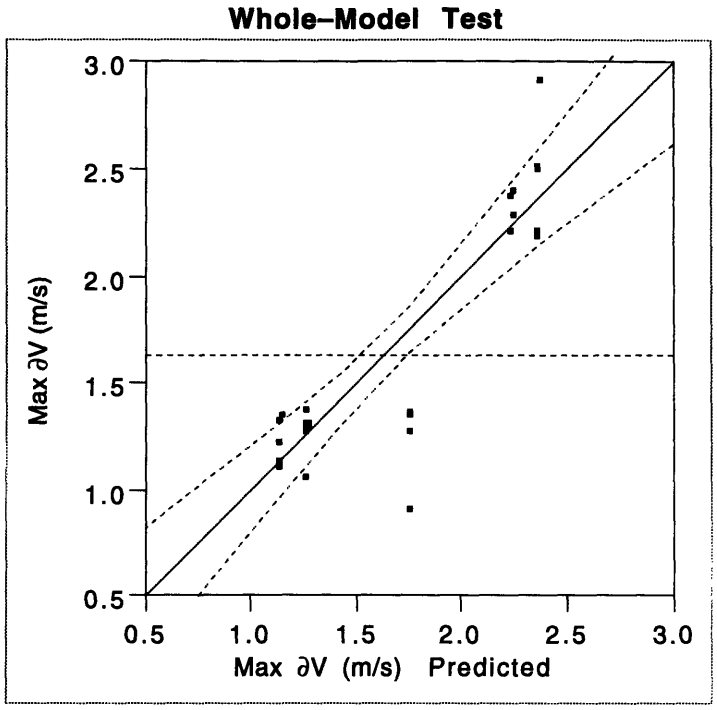

Figure 5.4: Multiple Linear Regression Model on Maximum Delta V

5.2.2 Overshoot Response Model

The overshoot of the web linear speed is more sensitive to roll radius and transmission (load in psi) than the maximum delta V was. In the case of the overshoot, there is only a 1.19% probability that the effect of roll radius is due to noise and 2.55% probability that the effect of transmission load is due to noise.

The response of the overshoot in the web speed is given by:

$$Overshoot = 19.05 + (5.4)\ Roll\ Radius - (2.86)\ Line\ Ramp + (0.068)\ Transmission \tag{5.3}$$

And the statistics are:

Response: Overshoot (%)	
Summary of Fit	
Rsquare	0.907034
Root Mean Square Error	1.340302
Mean of Response	11.61959
Observations (or Sum Wgts)	27

Parameter Estimates

Term	Estimate	Std Error	t Ratio	Prob>|t|
Intercept	19.055651	0.94012	20.27	0.0000
Roll Radius (m)	5.3990687	1.97756	2.73	0.0119
Line Ramp (s)	-2.859358	0.19452	-14.70	0.0000
Transmission (psi)	0.0681472	0.02853	2.39	0.0255

Effect Test

Source	Nparm	DF	Sum of Squares	F Ratio	Prob>F
Roll Radius (m)	1	1	13.39008	7.4538	0.0119
Line Ramp (s)	1	1	388.17611	216.0845	0.0000
Transmission (psi)	1	1	10.24727	5.7043	0.0255

Analysis of Variance

Source	DF	Sum of Squares	Mean Square	F Ratio
Model	3	403.11690	134.372	74.8005
Error	23	41.31741	1.796	**Prob>F**
C Total	26	444.43431		0.0000

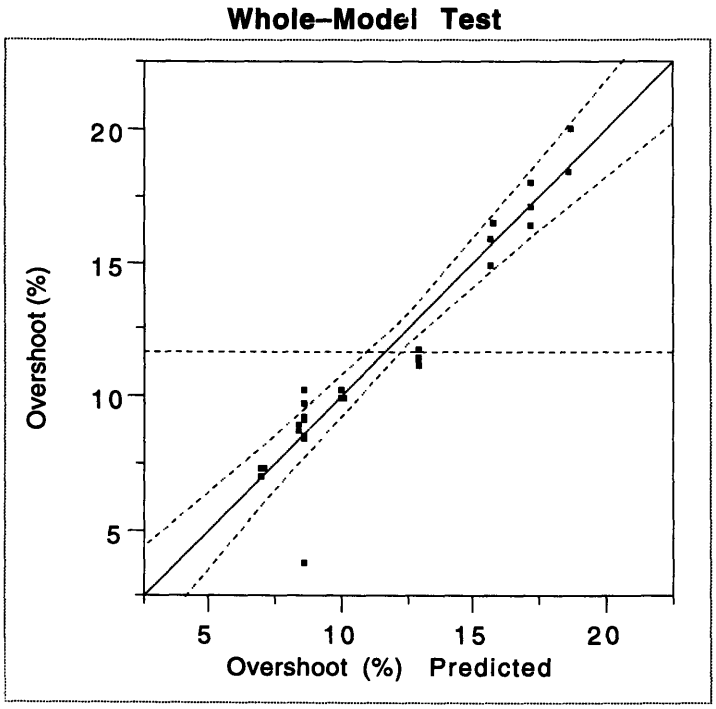

Figure 5.5: Multiple Linear Regression Model on Overshoot

The fit for the overshoot model is a lot better (R^2=90%). The line ramp remains as the dominant variable, but the roll radius (1.19% probability of effect due to noise) and the transmission (2.55% probability of effect due to noise) are also significant. The fact that the roll radius, i.e. the inertial load seen by the motor, is a significant factor in the system's overshoot indicates that the surface belt drive is not completely immune to changes in load.

5.2.3 Dancer Time Response Model

The damping in the system as measured by the "settling time" of the dancer is significantly affected by both roll radius and ramp time. Only 0.17% and 1.56% probability of the respective effects due to noise. Unlike the first two variables, the time response of the dancer is also affected by three interactions between variables. These interactions are: roll radius and transmission, roll radius and dancer initial condition, and line ramp and transmission. In no case does the probability of noise-related response exceed 5.42%.

The regression model for the dancer settling time with three interactions between variables are present is given by:

$$\begin{aligned} \textit{Dancer time} = {} & 8.09 - (23.35)\,\textit{Roll Radius} + (1.71)\,\textit{Line Ramp} \\ & + (0.19)\,\textit{Rad*Trans} + (0.009)\,\textit{Rad*DanceIC} \\ & - (0.019)\,\textit{Ramp*Trans} - (0.0008)\,\textit{Rad*DanceIC} \end{aligned} \tag{5.4}$$

And the statistics are:

Response: Overshoot (%)

Summary of Fit

Rsquare	0.52539
Root Mean Square Error	0.853385
Mean of Response	6.678418
Observations (or Sum Wgts)	28

Parameter Estimates

Term	Estimate	Std Error	t Ratio	Prob>|t|
Intercept	8.0955043	0.57928	13.98	0.0000
Roll Radius (m)	-23.34504	6.49386	-3.59	0.0017
Line Ramp (s)	1.7094637	0.64947	2.63	0.0156
Roll Rad*Transmis	0.1930277	0.09464	2.04	0.0542
Roll Rad*Dancer I	0.0086818	0.00314	2.76	0.0117
Line Ram*Trans	-0.018913	0.00921	-2.05	0.0528
Line Ram*Dancer I	-0.000775	0.00031	-2.52	0.0198

Effect Test

Source	Nparm	DF	Sum of Squares	F Ratio	Prob>F
Roll Radius (m)	1	1	9.4118216	12.9236	0.0017
Line Ramp (s)	1	1	5.0452827	6.9278	0.0156
Roll Rad*Transmis	1	1	3.0295479	4.1599	0.0542
Roll Rad*Dancer I	1	1	5.5526334	7.6245	0.0117
Line Ram*Transmis	1	1	3.0689224	4.2140	0.0528
Line Ram*Dancer I	1	1	4.6315281	6.3597	0.0198

Analysis of Variance

Source	DF	Sum of Squares	Mean Square	F Ratio
Model	6	16.929907	2.82165	3.8745
Error	21	15.293584	0.72827	Prob>F
C Total	27	32.223491		0.0093

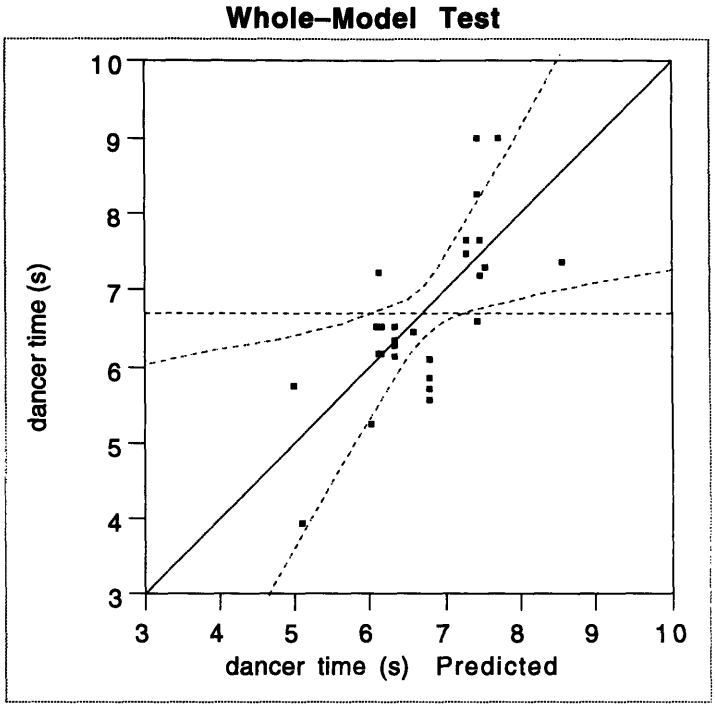

Figure 5.6: Multiple Linear Regression Model on Dancer Settling Time

All interactions are significant. The interaction with the highest probability of effects due to noise being only 5.42%. Once again, roll radius and ramp time dominate the response. In this case however, the response is dominated by the roll radius (i.e., inertial load). Physically this means that higher loads increase the overall damping of the system and dancer motion settles in shorter times. The effect of the ramp time has a positive slope for this model. That is, as the ramp time increases, the duration of the dancer oscillations is greater. It was observed during the tests that dancer motion indeed takes longer to settle for long ramp times, but that the damped frequency of the oscillations is lower than for short ramps.

In general, we can conclude the following from the DOX:

- Tension is directly correlated to ramp time. Increasing ramp time will significantly reduce peak tension.

- Surface belt drive does not completely mask the effect of a changing inertial load as seen by the motor. Increased inertial load and lower "grip" of the belt drive (lower loading pressure) increase the overshoot of the system's response.

- Dancer dynamic transients (oscillations) are directly correlated to ramp time and inertial load. The transient increases with increased ramp time and decreased load.

Chapter 6

Model Validation and Simulation Results

The two models that were developed are intended to be used to estimate the tension in the web that cannot be measured directly. These estimates can be used to determine the shape and location of the stress distribution that induce system failures. The results obtained from the simulations show that the estimated tensions are not in the region where material strength data suggests that interference occurs. This region is in the 30 N range while the tensions estimated from the DOX simulations are in the 15 N range. As expected from these two ranges, no material ruptures occured during the designed experiments.

6.1 Linear Model Parameters and Assumptions

6.1.1 Motor, Transmission, and Roll.

It was assumed that for the web supply model shown in Figure 3.3, the inertia of the motor and transmission are negligible compared to the inertia of the large roll of material. The web has a density $\rho=365$ kg/m^3. The inner core of the roll has a diameter Di=8 3/4 " and an outer diameter Do=58". The width of the material is w=4 3/4". The total inertia of the roll is given by:

$$J_{roll} = J_{solid} - J_{hole}$$

$$J_{roll} = \frac{1}{2}\rho\left[(\pi)\left(\frac{Do^2}{4}\right)(w)\right]\left[\frac{Do^2}{4}\right] - \frac{1}{2}\rho\left[(\pi)\left(\frac{Di^2}{4}\right)(w)\right]\left[\frac{Di^2}{4}\right] \qquad (6.1)$$

Given the values for density and roll dimensions, the roll inertia is:

$$J_{roll} = 20.53\,\mathrm{N}\cdot\mathrm{m}\cdot\mathrm{s}^2.$$

At steady state the DC motor speed is set to 1370 rpm. The transmission ratio between the DC motor speed and the roll angular speed is given by:

$$TR = \frac{143 \text{ rad/s}}{4.8 \text{ rad/s}} = 29.87$$

From the bond graph in Figure 3.2 we see that the equivalent inertia reflected into the motor is:

$$J_{eq} = J_4 = \frac{J_{roll}}{TR^2} = \frac{20.53 \text{ N} \cdot \text{m} \cdot \text{s}^2}{29.87^2} = 2.3 \text{ x } 10^{-2} \text{ N} \cdot \text{m} \cdot \text{s}^2$$

The time constant of the first order web supply model is given by the ratio of the equivalent inertia to the equivalent viscous damping. Assuming that the settling time of the first order system is one second, that is,

$$4\tau = 1 \text{ sec} = 4\frac{J_{eq}}{b_{eq}}$$

the equivalent viscous damping is given by:

$$b_{eq} = b_4 = 4\, J_{eq} = 9.2 \text{ x} 10^{-2} \text{ N} \cdot \text{m} \cdot \text{s}$$

The DC motor is rated at 1750 rpm at 180 V and 9.5 A. Its corresponding torque constant is given by:

$$K_t = \left(\frac{180 \text{ V}}{1750 \text{ rpm}}\right)\left(\frac{60 \text{ sec}}{1 \text{ min}}\right)\left(\frac{1 \text{ rev}}{2\pi \text{ rad}}\right)\left(\frac{1 \text{ N} \cdot \text{m}}{1 \text{ V} \cdot \text{A} \cdot \text{sec}}\right)$$

$$K_t = 0.9827 \text{ N} \cdot \text{m/A}$$

6.1.2 Idlers

Idlers have an approximate mass, m=0.5 kg, which includes the bearing that is mounted on both sides of the idlers. Their outer diameter, Do=2" and their inertia is:

$$J = \frac{1}{2} m \frac{Do^2}{4} = 1.61 \text{ x } 10^{-4} \text{N} \cdot \text{m} \cdot \text{s}^2$$

It has been assumed (because it was not possible to remove the idlers from the equipment and test them) that when subject to a step change in torque, the idlers reach a steady state velocity in one second. This estimate is high and results in tension losses across each idler that are approximately three times their nominal value. The bearing drag on the idlers using this assumption is:

$$b = 4\,J = 6.45\ \text{x}10^{-4}\ \text{N}\cdot\text{m}\cdot\text{s}$$

6.1.3 Spans of Material

The approach used in modeling the material was to treat each individual span as a discrete and massless spring. The constitutive equation for such elements is given by Hook's law:

$$F = K\,x \tag{6.2}$$

Where the spring constant K is given by:

$$K = \frac{EA}{L} \qquad \text{with} \begin{cases} E = 5\ \text{kpsi} \\ A = 4.75'' \times .003'' \\ L = \text{span length} \end{cases} \tag{6.3}$$

For a span length of 1 meter the spring constant K=316 N/m.

6.2 Linear Model Simulations

Using the parameter estimates of Section 6.1 startup transients were simulated. The actual line reference measured in the production equipment was used to drive the model. As seen in Figures 6.1 and 6.2, the model is able to reproduce the web linear speed and the DC motor angular speed.

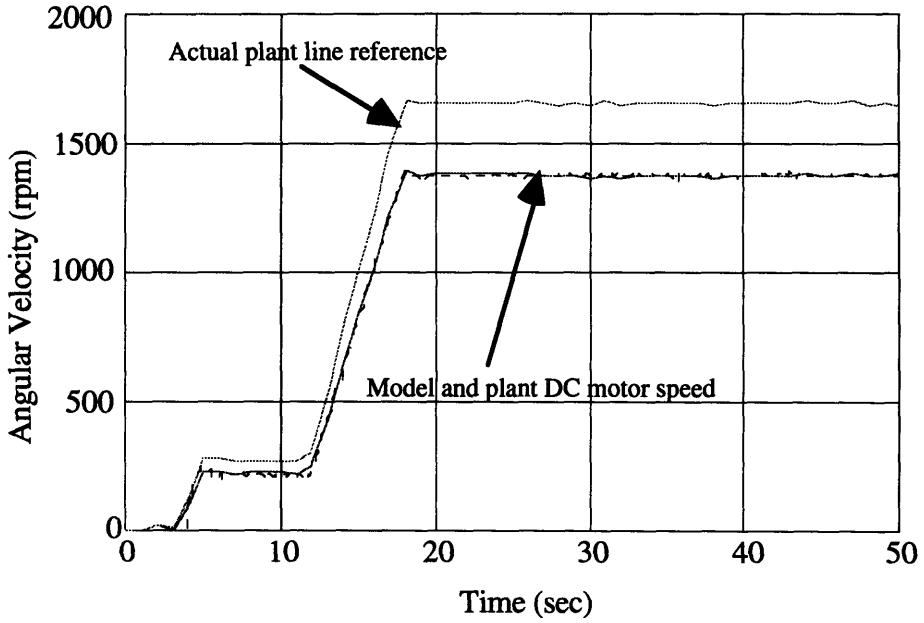

Figure 6.1: Linear Model and Plant Angular Velocities

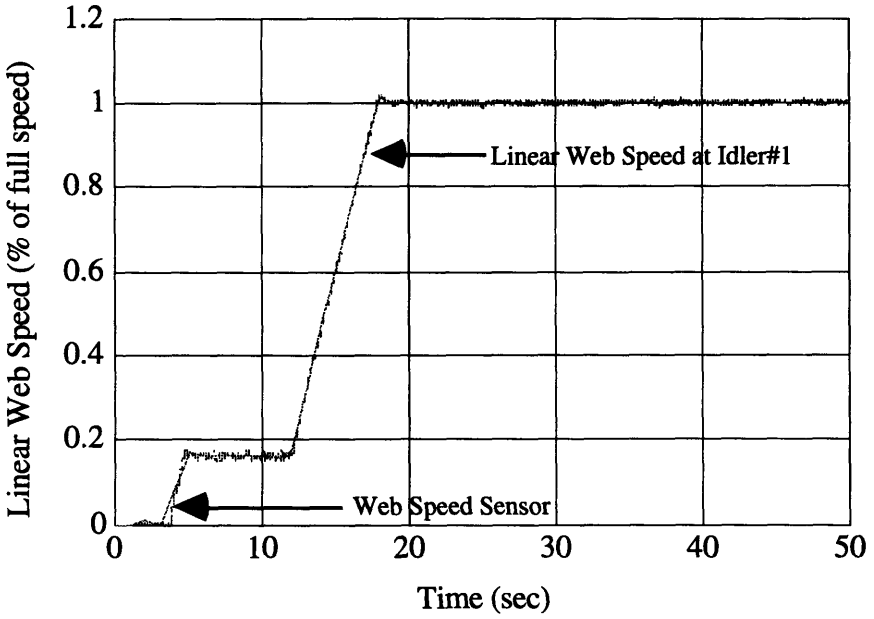

Figure 6.2: Plant Web Speed and Linear Model Web Speed vs. Time

The dancer motion is less accurately reproduced, but the range of motion is similar as seen in Figure 6.3. (Dancer position was estimated using 0.2V=10 deg. as an approximation based on the observed motion and the range of the voltage mesaured)

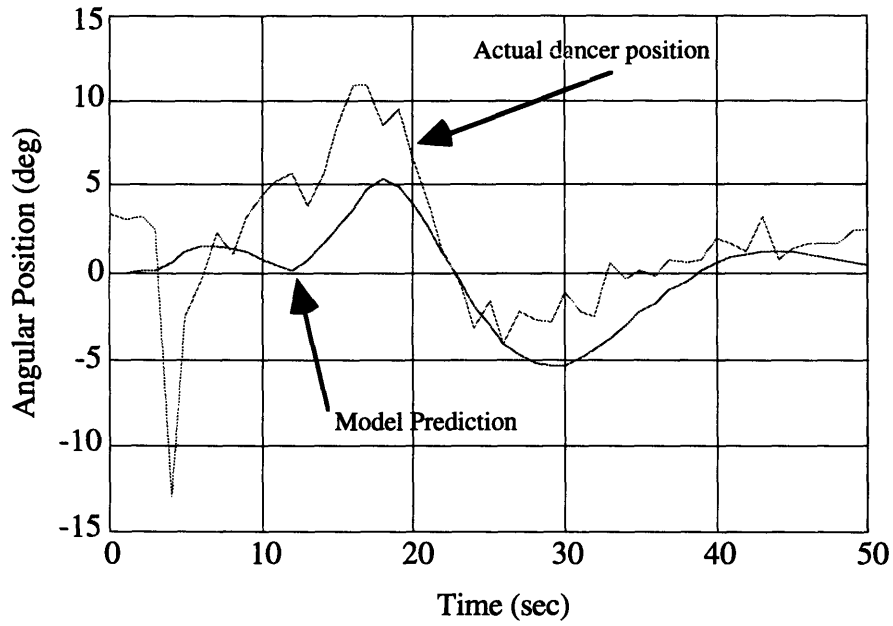

Figure 6.3: Dancer Motion of Production Equipment During Startup Transient

From the preceding plots we can conclude that the model is fairly accurate in reproducing two machine states (dancer position and unwind motor speed) and one material state (web linear speed) that were recorded during experimental runs. If it is assumed that the model accurately describes process physics, it can be speculated that the model's predictions of tension are equally accurate. These tensions are shown in Figure 6.4.

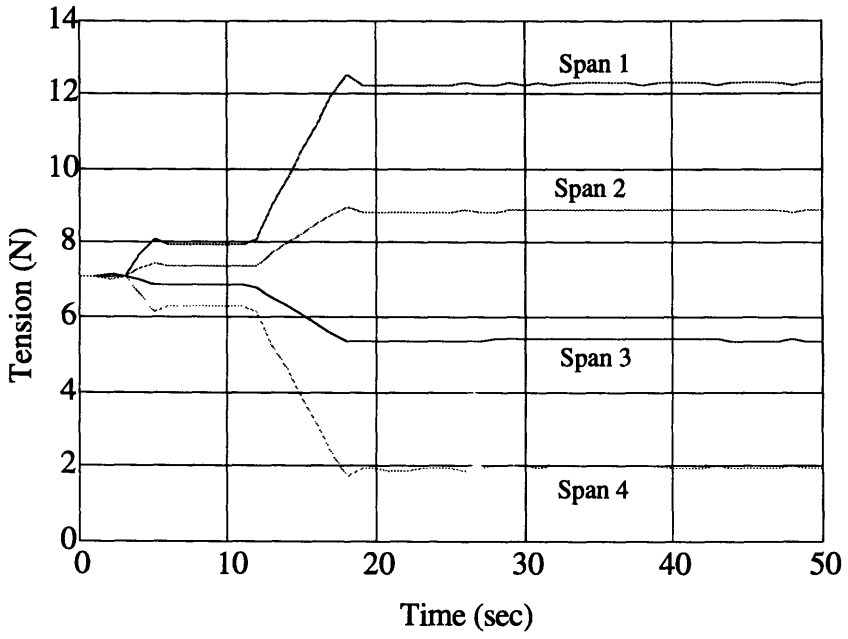

Figure 6.4: Simulated Web Tension Transients

A simulation was also run with a small roll of outer diameter Do=0.4 meters. The smaller roll has a higher angular velocity than the larger roll because the linear web speed is kept constant by the surface drive. Thus the transmission ratio of the system changes to:

$$TR = \frac{143 \text{ rad/s}}{17.75 \text{ rad/s}} = 8.056$$

and the equivalent inertia of the system to:

$$J_{eq} = J_4 = \frac{J_{roll}}{TR^2} = \frac{.0765 \text{ N} \cdot \text{m} \cdot \text{s}^2}{8.056^2} = 1.18 \times 10^{-3} \text{ N} \cdot \text{m} \cdot \text{s}^2$$

The equivalent damping of the system can be assumed to remain the same as with the large roll or can be assumed to decrease proportionately with the system's inertia. That is, b_4=9.2 x 10^{-2} Nms (high damping) or b_4=4.72 x 10^{-3} Nms (low damping).

In all cases, the tensions in the web remain approximately the same. The DC motor speed and the linear speed of the web are also approximately constant for both large and small inertias. Only the difference between web supply and web demand and consequently the dancer motion were significantly different as seen in Figures 6.5 and 6.6.

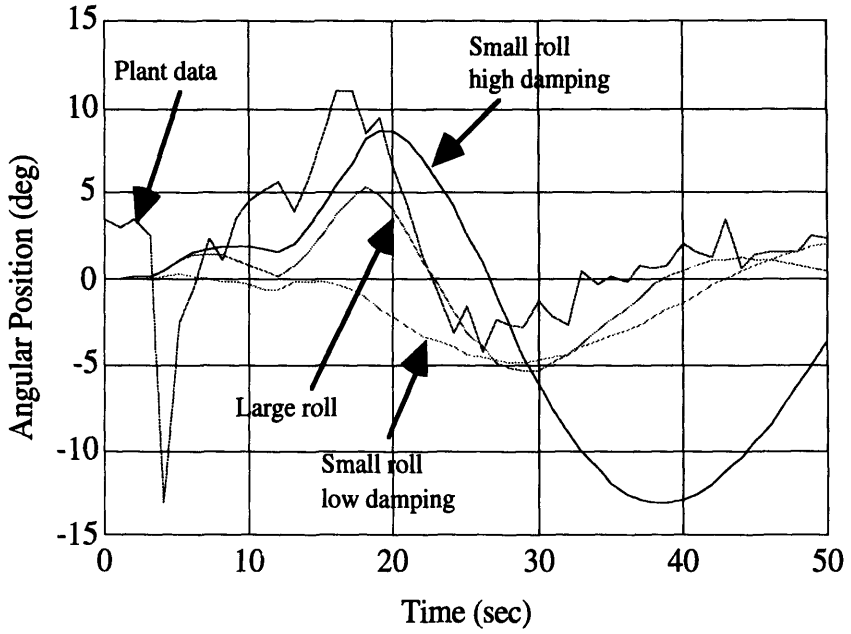

Figure 6.5: Dancer Motion for Different Inertial Loads and Damping Coefficients

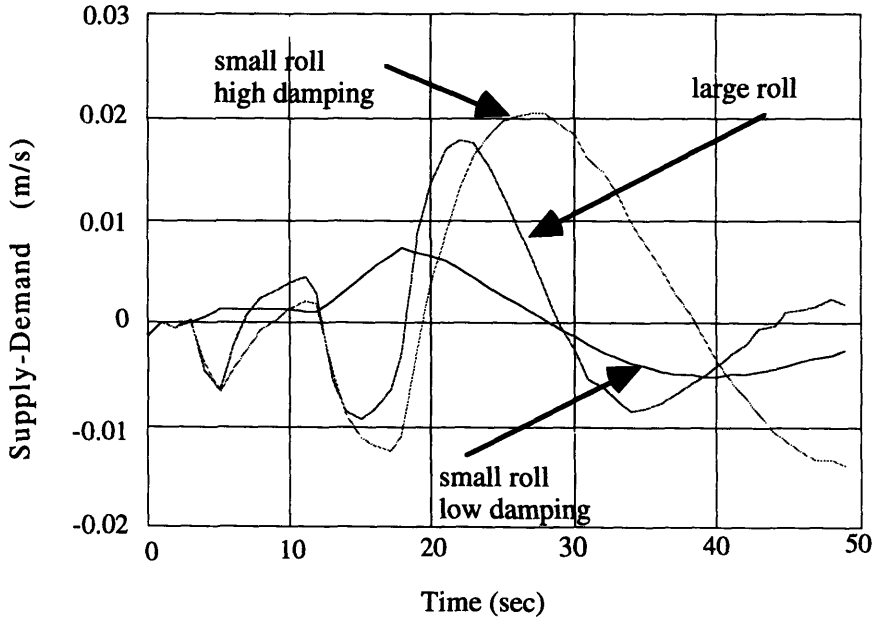

Figure 6.6: Web Balance for Different Inertial Loads and Damping Coefficients

It is clear from Figures 6.5 and 6.6 that the dancer motion directly follows the difference in web velocity seen at its endpoints. When the difference is negative, the dancer needs to give up web and it rotates in the positive direction. Similarly when the difference is positive, a web surplus exists and the dancer drops. The simulation run with a small roll and low damping results in the smallest difference between supply and demand and the least dancer motion. However, the simulations indicate that the tension in the web does not decrease proportionately. That is, no dancer motion does not necessarily guarantee lower tensions and lower probability of breaking the web. The tension necessary to overcome the inertia of the idlers and the bearing drags in them can still be sufficient to cause a breakout.

6.2.1 System Sensitivity to Modulus Variations

The tensions in the spans of the linear lumped parameter model do not exhibit significant sensitivity to variations in the material modulus. That is, the predicted peak tension is not affected by variation in the modulus if all other parameters remain constant. The eigenvalues of the A matrix in Equation (3.12) were calculated for ten different spring constants ranging from K=100 N/m to K=1000 N/m, and three different values of idler bearing frictions. Figure 6.7-6.9 indicate how the eigenvalues of the system do not change their real component, ie, their time response and different modulus simply affect the damped natural frequencies of the system. The changes in bearing friction, though, shift the location of the eigenvalues along the real axis. Thus, bearing friction does affect the time response.

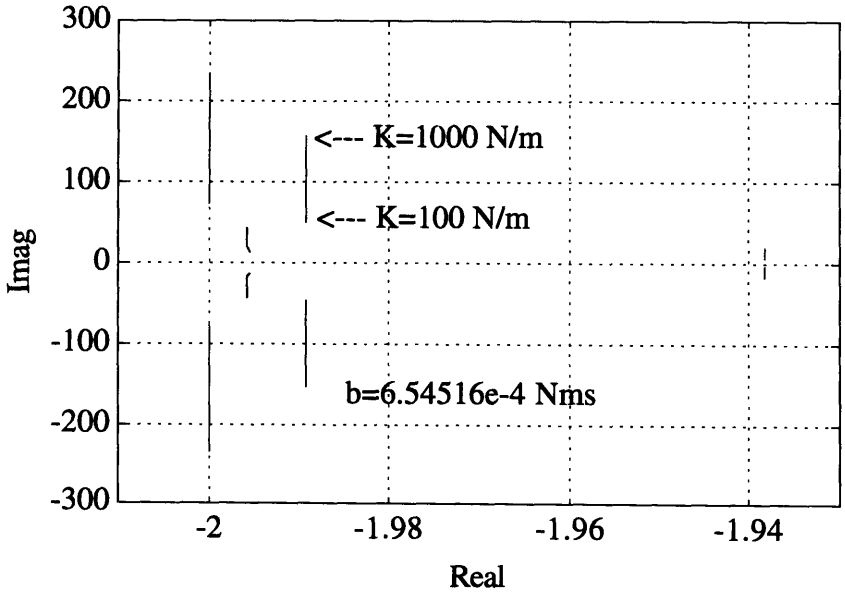

Figure 6.7: Eigenvalues of the A Matrix with Low Bearing Friction

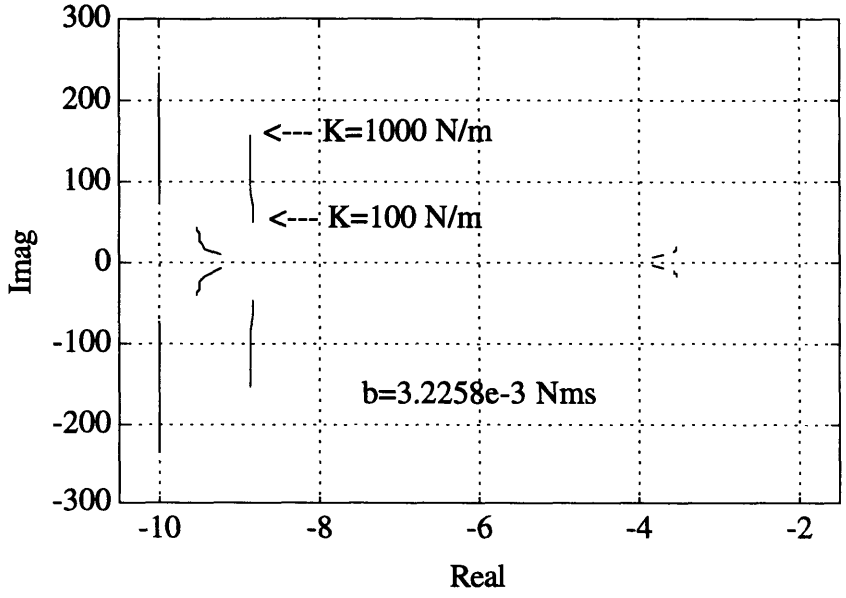

Figure 6.8: Eigenvalues of the A Matrix with Medium Bearing Friction

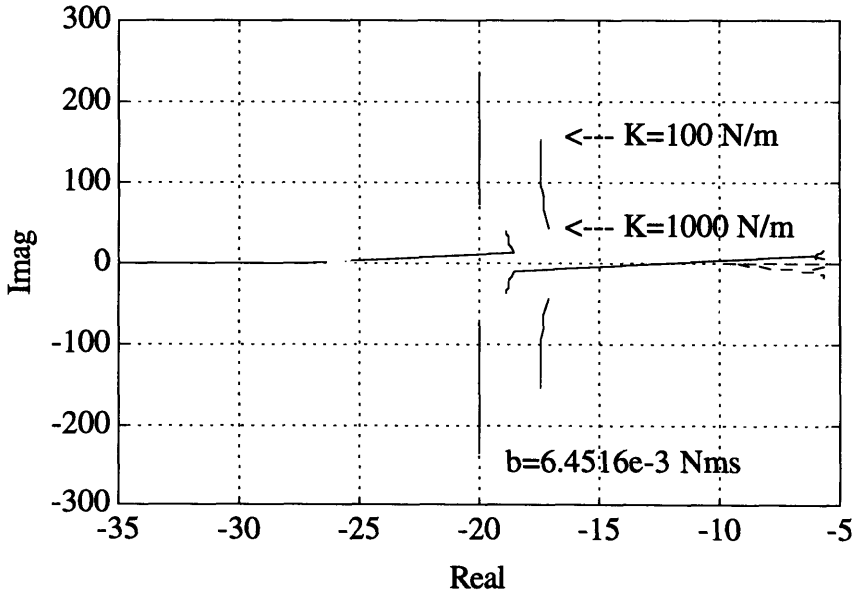

Figure 6.9: Eigenvalues of the A Matrix with High Bearing Friction

6.2.2 System Sensitivity to Bearing Friction Variations

When the material modulus is fixed and the bearing friction varied from b=6.4516e-4 Nms to b=6.4516e-3 Nms, it is clear the system is more sensitive to changes in friction than to changes in modulus. When the friction varies, the real part of the eigenvalues changes significantly, but the imaginary

component remains approximately constant. Figures 6.10-6.12 show the eigenvalues of the A matrix as a function of idler bearing friction for three values of material modulus (K=100 N/m, K=316 N/m, and K=1000 N/m).

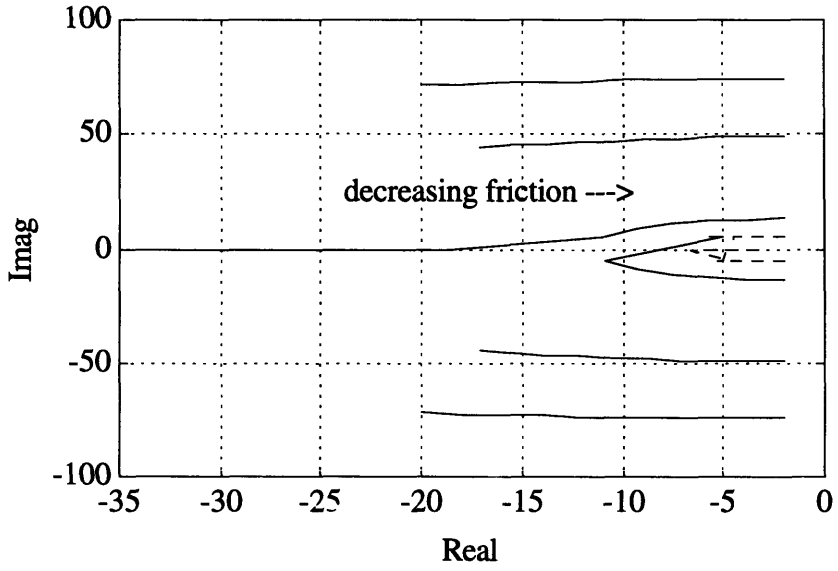

Figure 6.10: Eigenvalues of the A matrix for K=100 N/m

Notice how in Figure 6.10, as the friction decreases two of the eigenvalues converge and become complex conjugates that further induce oscillations in the system.

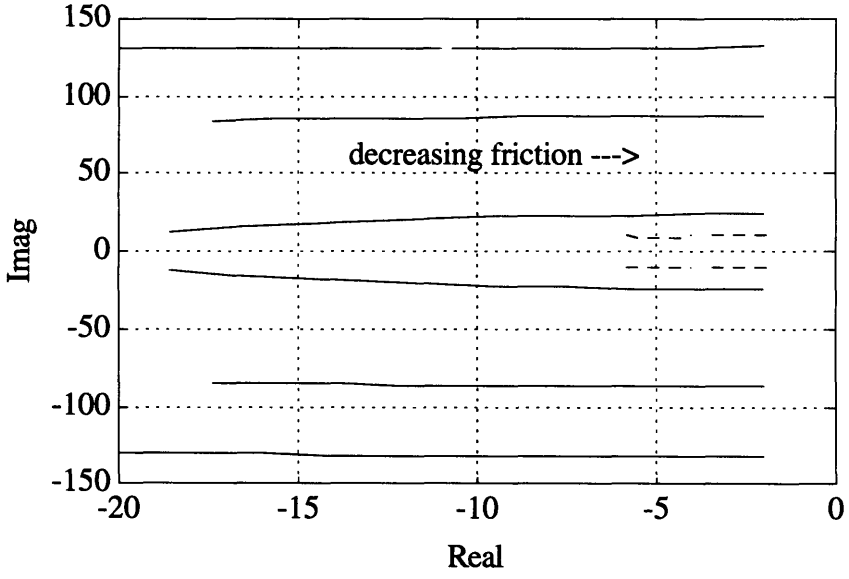

Figure 6.11: Eigenvalues of the A matrix for K=316 N/m

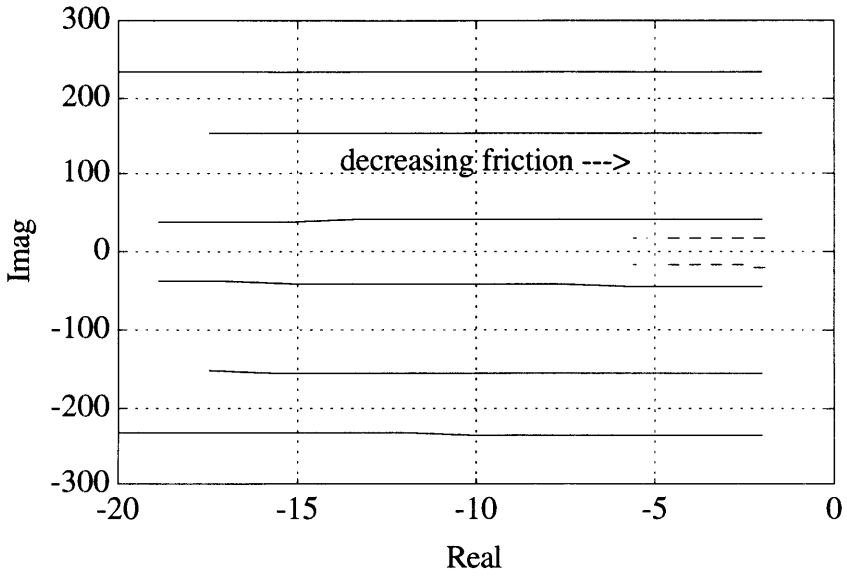

Figure 6.12: Eigenvalues of the A matrix for K=1000 N/m

6.2.3 Peak Tension Sensitivity to Ramp Time.

Several time traces for span tensions were simulated for different material moduli, bearing friction (damping coefficient), and ramp times. Table 6.1 summarizes the different simulation scenarios. Note that case#10 is equal to case#2 and case#7 is equal to case#5.

Case No.	K	Damping	Ramp Time	Peak Tension
1	100 N/m	6.4516 e-4 Nms	7.5 sec	12.61 N
2	316 N/m	6.4516 e-4 Nms	7.5 sec	12.63 N
3	1000 N/m	6.4516 e-4 Nms	7.5 sec	12.63 N
4	100 N/m	6.4516 e-4 Nms	2.0 sec	13.21 N
5	316 N/m	6.4516 e-4 Nms	2.0 sec	13.22 N
6	1000 N/m	6.4516 e-4 Nms	2.0 sec	13.21 N
7*	316 N/m	6.4516 e-4 Nms	7.5 sec	12.63 N
8	316 N/m	3.2258 e-3 Nms	7.5 sec	33.85 N
9	316 N/m	6.4516 e-3 Nms	7.5 sec	60.42 N
10*	316 N/m	6.4516 e-4 Nms	2.0 sec	13.22 N
11	316 N/m	3.2258 e-3 Nms	2.0 sec	34.19 N
12	316 N/m	6.4516 e-3 Nms	2.0 sec	60.45 N

Table 6.1: Summary of Tension Transient Simulations on Linear Model

It is clear that bearing friction is most responsible for peak values in tension. Ramp time, however, is also a significant factor. When bearing friction is not "too" high and the inertial effects of accelerating idlers dominate, short ramp times increase the peak tension in the system as seen in Figure 6.13. For example if we look at case#2 and case#5 both of which where run with low friction and "nominal" modulus, a decrease in ramp time from 7.5 sec to 2 sec result in a peak tension increase of nearly 5%. Furthermore, the amplitude of tension oscillations also increases. The higher tension and added "ringing" of the system tend to increase the probability of the material breaking.

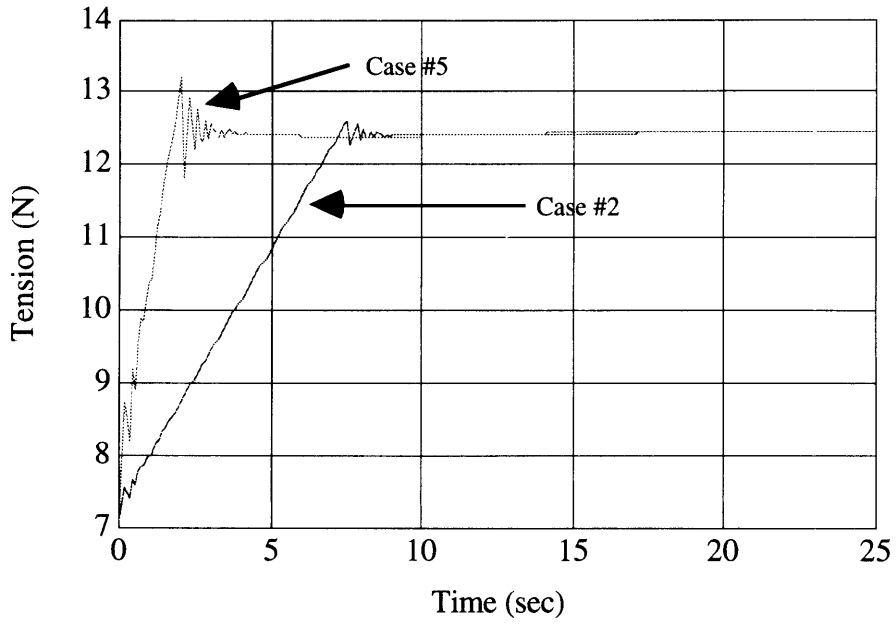

Figure 6.13: Effect of Decreased Ramp Time on Peak Tension

However, as bearing friction increases it begins to dominate over inertial effects and decreases in ramp time become less significant. Figure 6.14 shows that a decrease in ramp time from case#8 to case#11 only results in 1% increase in peak tension. For cases 9 and 12, shown in Figure 6.15, friction is ten times that of cases 5 and 2, and the increase in peak tension is only 0.03%. Notice how as the friction increases, changes in ramp time become less significant, but the final steady state value of tension is considerably higher (i.e. notice difference in scales).

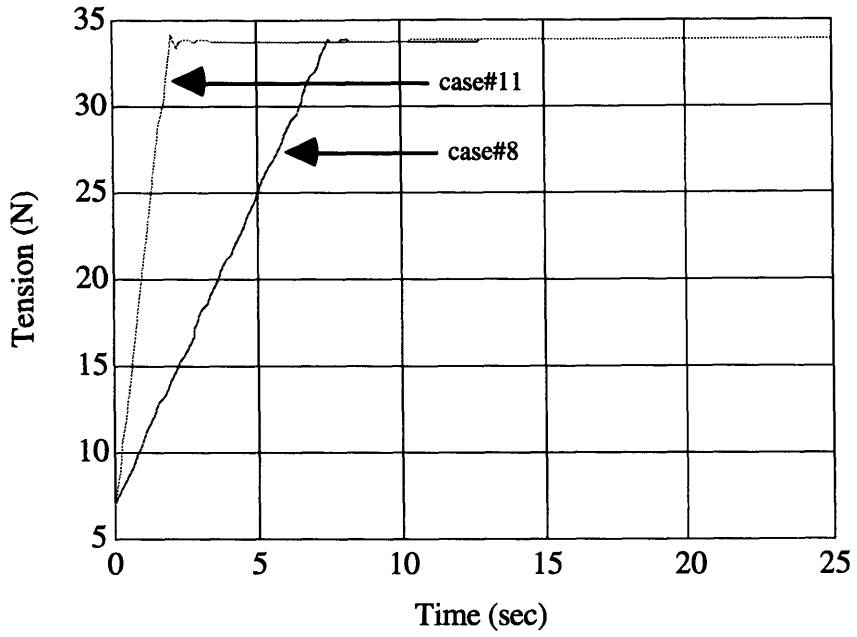

Figure 6.14: Decreased Overshoot in Peak Tension Due to Increased Friction

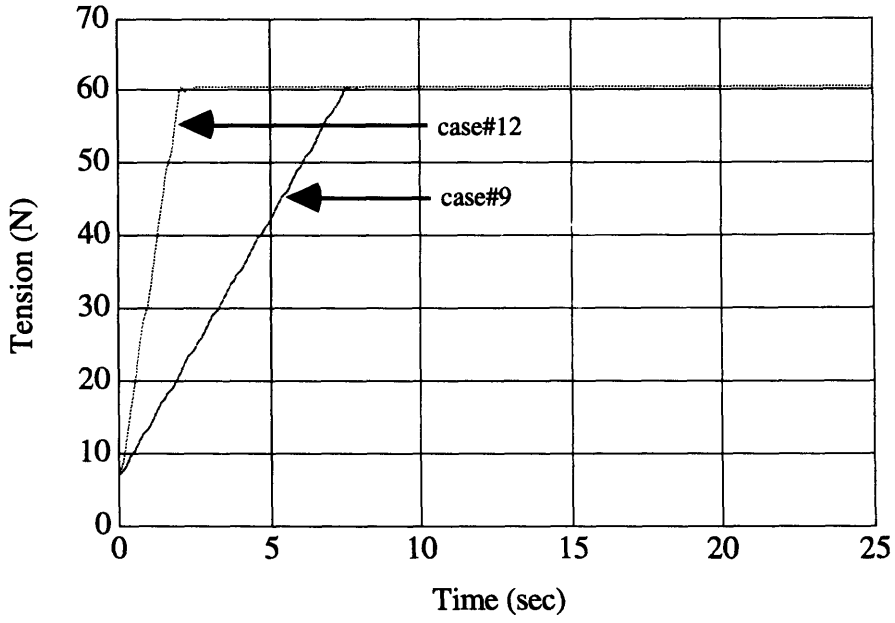

Figure 6.15: Peak Tensions for Heavily Damped Idlers

6.3 Linear Model Limitations

The tensions estimated by the model (Figure 6.4) do not exhibit significant spikes, oscillations or unusually high values, that is, failure is not predicted. Nonetheless, the actual system still experiences failures 3.42% of the time.

This leads to believe that localized phenomena might lead to material breakouts. Thus, one of the limitations of this model is that it treats tension only as a function of time for each span and it cannot predict localized phenomena. In reality the continuous web exhibits tension transients that are a function of time and position for which a lumped parameter model is limited.

Another major limitation of the lumped parameter model approach is shown in Figure 6.16. The figure shows a plot of the four span tensions, in which two of the spans reach a negative tension at steady state. This occurs because the spring model formulation allows for the springs to be in compression. However, the real system is not capable of doing that because, the web can't be compressed and "push" on the idlers. From physical insight of the process we know that is imposible and negative tension means a slack web.

The model requires that at steady state the linear velocity of the web be 100% of its intended value. The difference in tension seen across an idler so that this velocity is maintained is given by the final value theorem. Assuming a step change in tension, the steady state angular velocity of the idlers is given by:

$$\dot{\theta}_{ss} = \lim_{s \to 0} s \frac{\Delta T}{s} \left(\frac{\cdot}{Js + b} \right) = \frac{\Delta T r}{b} \tag{6.4}$$

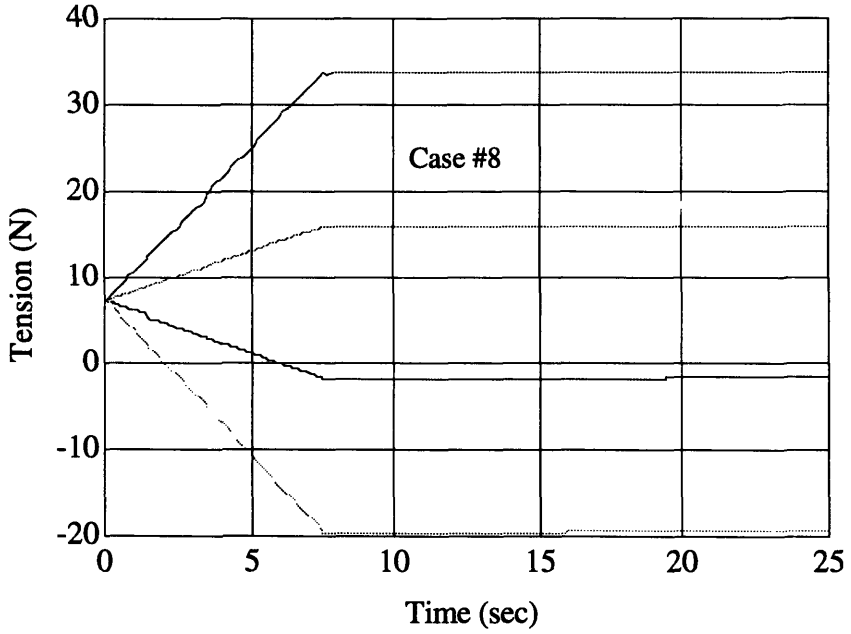

Figure 6.16: Tension Transients for Case#8

Solving for ΔT in Equation (6.4) it can be seen that the difference in tension seen across an idler at steady state is directly proportional to the

bearing friction. Assuming that the idlers' radius r=0.0254m, and b=3.2258 x 10^{-3} Nms (case#8), the required tension to keep the idlers rotating is:

$$\Delta T = \frac{\dot{\theta}_{ss} b}{r} = 17.75 \text{ N}$$

When the bearing drag was increased the tensions in span 1 and span 2 increased. However, for the dancer to reach an equilibrium position, the net torque on the dancer has to be balanced, and thus T3 and consequently T4 decrease. Before the startup, all the tensions in the spans are the same because there is no motion. This tension is the necessary tension to keep the dancer horizontal. Doing a balance of forces, this tension is:

$$F_o = \frac{(w_a R_{cm}) - (c_w - R_w)}{2 R_d} \tag{6.5}$$

With the parameters chosen (Section 6.1), Fo=7.12 N. For the net torque acting on the dancer arm to be zero, T2+T3=14.24 N. Figure 6.17 shows a plot of the net force acting on the dancer arm due to span tensions in case #8.

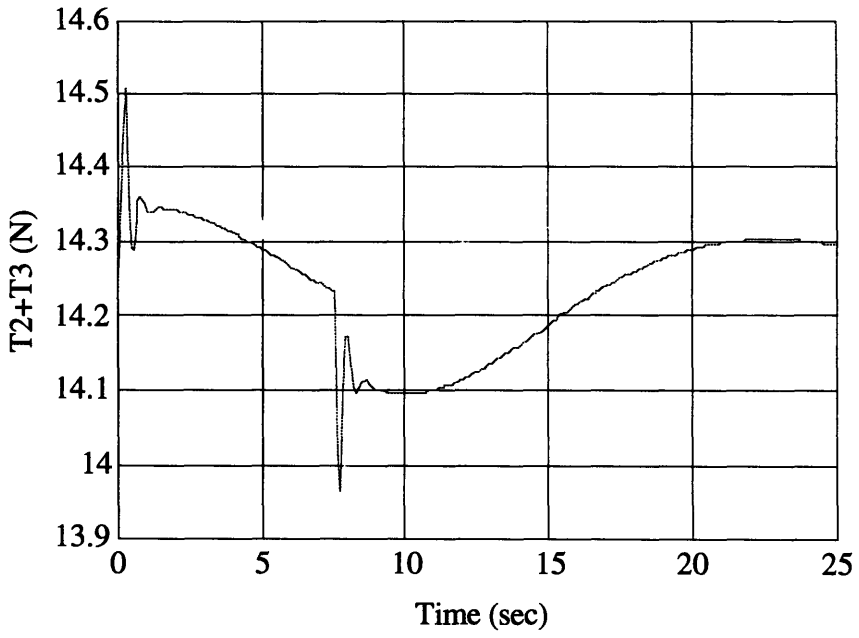

Figure 6.17: Span Tensions Acting on Dancer Arm

As the force approaches 14.24 N the dancer approaches an equilibrium position as seen in Figure 6.18.

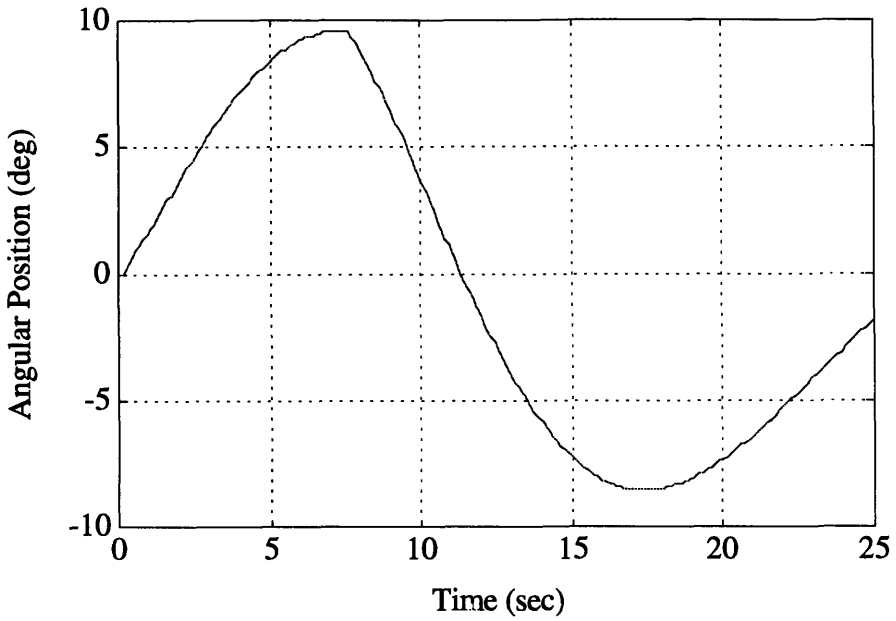

Figure 6.18: Dancer Motion for Case#8

The peak tension for this case was T1=33.85 N. However, the minimum tension in span 4 was T4= -19.80 N. This means that span four is actually pushing on idler#2 with T4. We know that is not the case and at best T4=0 N. This would require an increase in the tension of the following spans of 19.80 N, so that the peak tension in span 1 would really be T1=53.65 N.

For case#9 the required tension across an idler ΔT=35.43, which, as we expected, is directly proportional to the change in bearing damping. With increasing damping, the peak tension T1=60.42 N, but the minimum tension in span 4 decreases to T4= -46.88 N. The actual peak tension would then be T1=107.30 N.

Notice that aside from the limitation of the model (in relation to allowing for compression), increasing bearing friction has a very significant effect in increasing web tension. As will be discussed in Chapter 7, an idler bearing maintenance program is a very viable short-term solution to increasing the probability for successful startups.

6.4 Non-Linear Model Parameters and Assumptions

The non-linear model of the prototype tissue unwind was validated using experimental data from the design of experiments. Eight of the sixteen run conditions were evaluated (DOX 10,15,17,3,7,1,11,16) In all cases, the model is able to accurately reproduce the variables that were recorded on the test stand.

The configuration used to validate the model is shown in Figure 4.2. The belt drive and transmission have been modeled as an equivalent first order system. A discussion of the modeling of these components and the equivalent inertia and damping reflected into the motor is found in Appendix B. For the purpose of the current discussion it will suffice to say that Figure 6.19 shows a "web supply" block diagram that results from the modeling mentioned above.

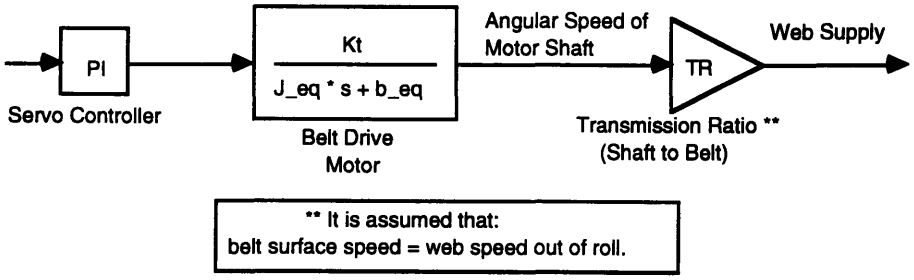

Figure 6.19: Block Diagram for "Web Supply Model"

6.4.1 Equivalent Inertial Loads

As seen from Equation B.3 (Appendix B), the equivalent inertia seen by the motor is given by:

$$J_{eq} = J_{motor} + J_{gear\#1} + \frac{J_{gear\#2}}{T_2^2} + \frac{J_{belt\ rollers}}{T_2^2} + \frac{J_{roll}}{T_1^2 T_2^2} \tag{6.6}$$

Where:

$$T_1 = \frac{R_{roll}}{r_{belt} + t_{belt}} = \frac{R_{roll}}{3.25''} \tag{6.7}$$

$$T_1 = \frac{90\ \text{teeth}}{32\ \text{teeth}} = 2.8125 \tag{6.8}$$

The gears and belt rollers are cast aluminum and will be assumed to be cylindrical. Then the inertia of the gears is given by:

$$J_{gear\#1,2} = \tfrac{1}{2}\pi r^4 \rho t$$

$$J_{gear\#1} = \tfrac{1}{2}\pi(1.75")^4(2.7 \times 10^3)(.75") = 3.15 \times 10^{-4}\, Nms^2 \qquad (6.9)$$

$$J_{gear\#2} = \tfrac{1}{2}\pi(4.5")^4(2.7 \times 10^3)(.75") = 1.3789 \times 10^{-2}\, Nms^2$$

Similarly, the inertia for the rollers is:

$$J_{belt\ rollers} = \tfrac{1}{2}\pi r^4 \rho t$$

$$J_{belt\ rollers} = 2\left[\tfrac{1}{2}\pi(3")^4(2.7 \times 10^3)(9")\right] = 8.279 \times 10^{-3}\, Nms^2 \qquad (6.10)$$

The specifications for the motor are:

$$K_t = 3.2\ \frac{\text{lb in}}{\text{A}} = 0.3616\ \frac{\text{N m}}{\text{A}}$$

$$J_{motor} = 0.041\ \text{lb in sec}^2 = 4.63 \times 10^{-3}\ \text{N m sec}^2 \qquad (6.11)$$

Using Equation 6.6 we can plot the total equivalent inertia seen by the motor and the contribution to that inertia due to the roll of material . Figure 6.20 shows both Jeq (total inertia) and J_roll_eq (inertia of roll reflected on the motor) as a function of roll radius.

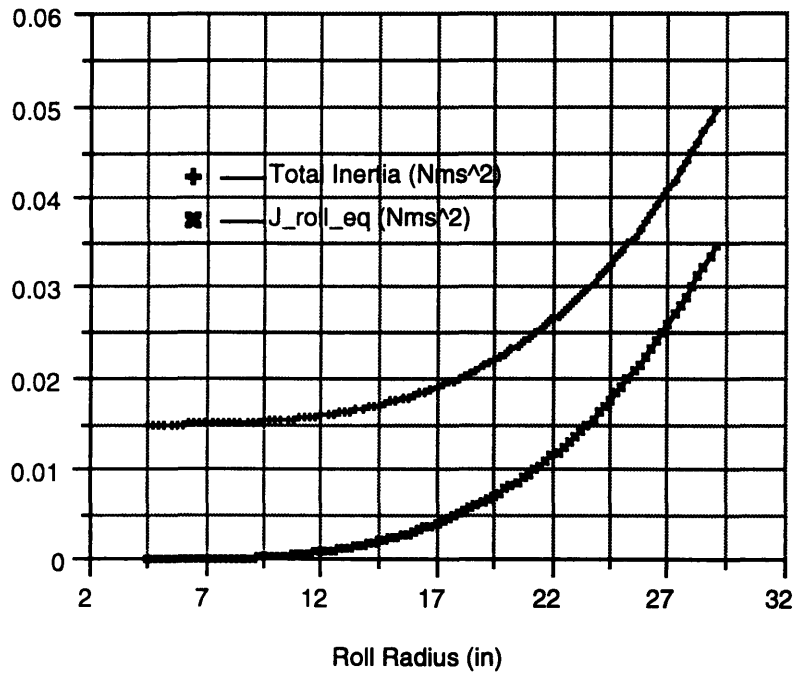

Figure 6.20: Inertial Loads on Belt Drive Motor (Prototype Unit)

6.4.2 Equivalent Bearing Friction

A step response for a small change in target unwind motor speed was performed and the 98% settling time (4 time constants) was seen to be approximately 3.5 sec. Given the equivalent first order system in Figure 6.19, the bearing friction is given by:

$$b_{eq} = b_{motor} + \frac{b_{beltrollers}}{T_2^2} + \frac{b_{rollmandrel}}{T_1^2 + T_2^2} \tag{6.12}$$

6.4.3 Dancer Arm Inertia

A key parameter for the model simulations is the numerical value of the dancer arm inertia. This value was estimated by subjecting the dancer arm to a step response. To do so, the pneumatic piston that pre-tensions the web was loaded so that the dancer arm would be fixed at its maximum negative position. The valve on the piston was then closed and the dancer arm was free to fall due to its own weight as seen in Figure 6.21.

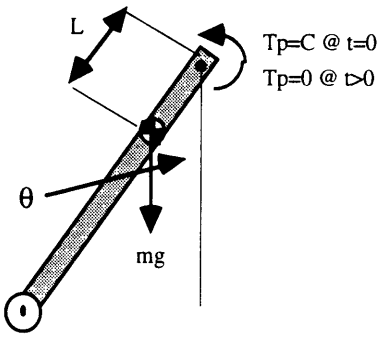

Figure 6.21: Configuration to Determine Dancer Arm Inertia

The equations of motions for the dancer arm is given by:

$$\ddot{\theta} = \frac{1}{J_{dancer}}\left[T_w + b_{dancer}\dot{\theta} - T_p\right] \qquad \dot{T}_w = mgL\dot{\theta}$$

Where:

$Tp = 8.46Nm$

$L = 22.5in.$

$m = 2.4kg$

(6.13)

The values of J_{dancer} and b_{dancer} were adjusted iteratively to obtain a good match between the dancer data and a simulation. Figure 6.22 shows data and model time traces for J_{dancer} = 2 Nms^2 and b_{dancer} = 5.2 Nms. These values were used in the DOX simulations. Note that the discrepancy in the model is mainly due to Coulomb (static) friction that has not been modeled in the dancer arm or in the idler bearings. It should be incorporated in future revisions of this model.

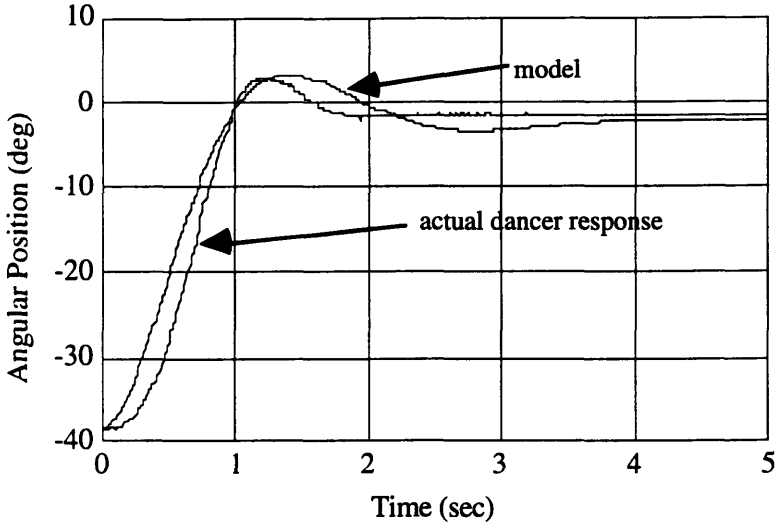

Figure 6.22: Dancer Arm Step Response

6.5 Non-linear Model Simulations

The following plots demonstrate the accuracy of the non-linear model in predicting the process parameters that were recorded during the DOX. No statistical analysis of the simulation results was performed because as seen in the plots the results of the DOX in the simulation would be very similar to the actual measurements. However, it is important to realize that the value of the model is that it allows the user to vary parameters that cannot be easily changed in the physical system and perform DOX's without using the actual equipment.

Each of the figures shown contains five plots. The first plot is the unwind motor speed. The dashed time trace is the model simulation which can be seen to match the measured data very well. The second plot is of linear web speeds. Metering speed is shown as the dotted trace (it does not overshoot), while predicted web speed is shown as the dashed line. The solid line is the measured web speed with a non-contact velocity sensor. The third plot is the predicted velocity difference between the web speed out of the roll (predicted) and the metering speed (measured). The fourth plot is the dancer position, that is, the angle θ_a between the dancer arm and the vertical (the orientation of the dancer arm in the prototype equipment is as seen in Figure 3.5).

Included in these figures (fifth plot) are the tension predictions for the eight spans in the dancer. The top trace corresponds to the last span in the dancer (prior to the metering point), while the first span in the dancer corresponds to the bottom trace (remaining spans are in decreasing order). The high-frequency oscillations are noticeable. They are due to the combination of light idlers and low modulus material which results in high natural frequencies.

DOX 10

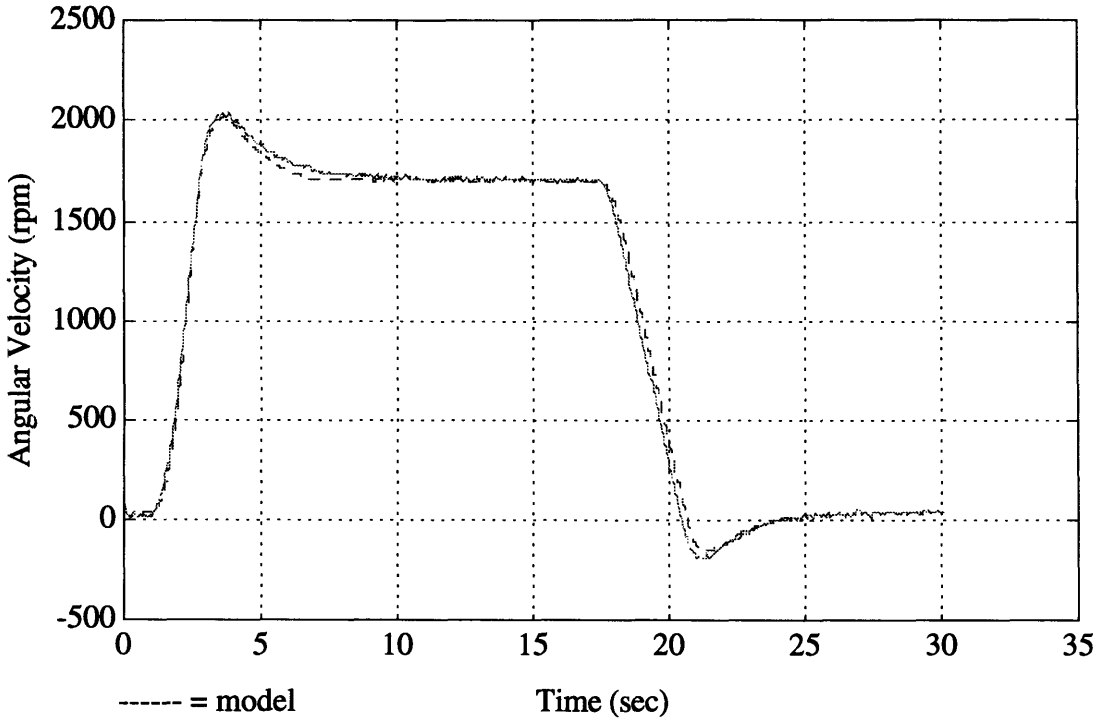

Figure 6.23a: Motor Speeds

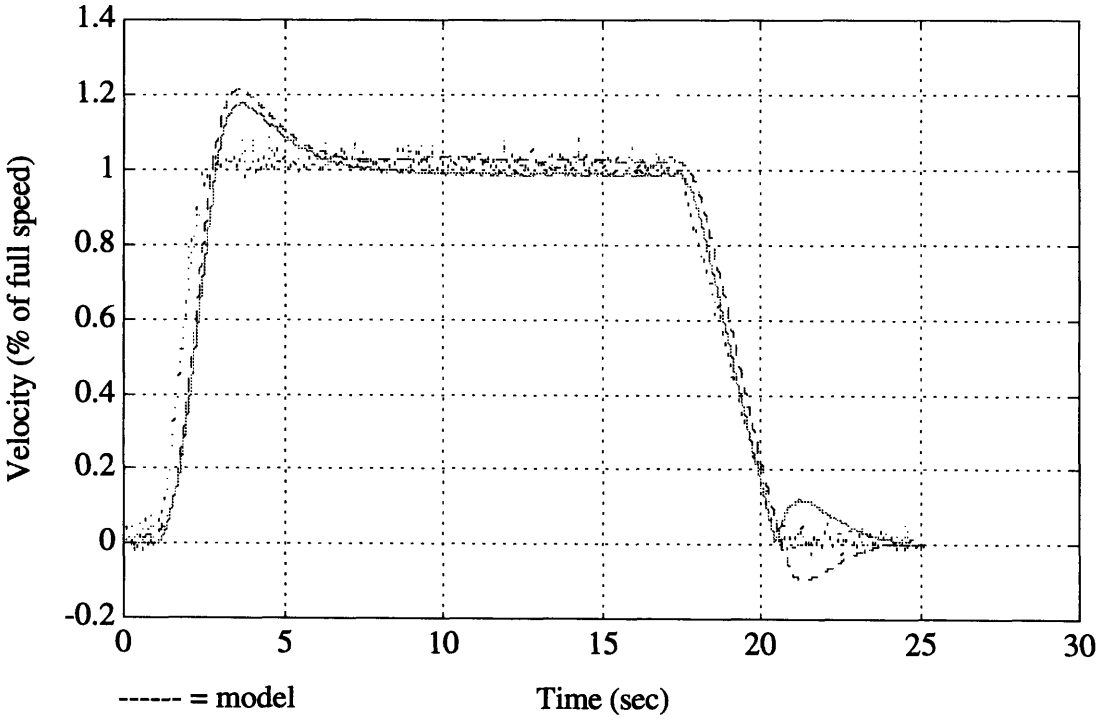

Figure 6.23b: Linear Web Speed and S-Wrap Metering Speed

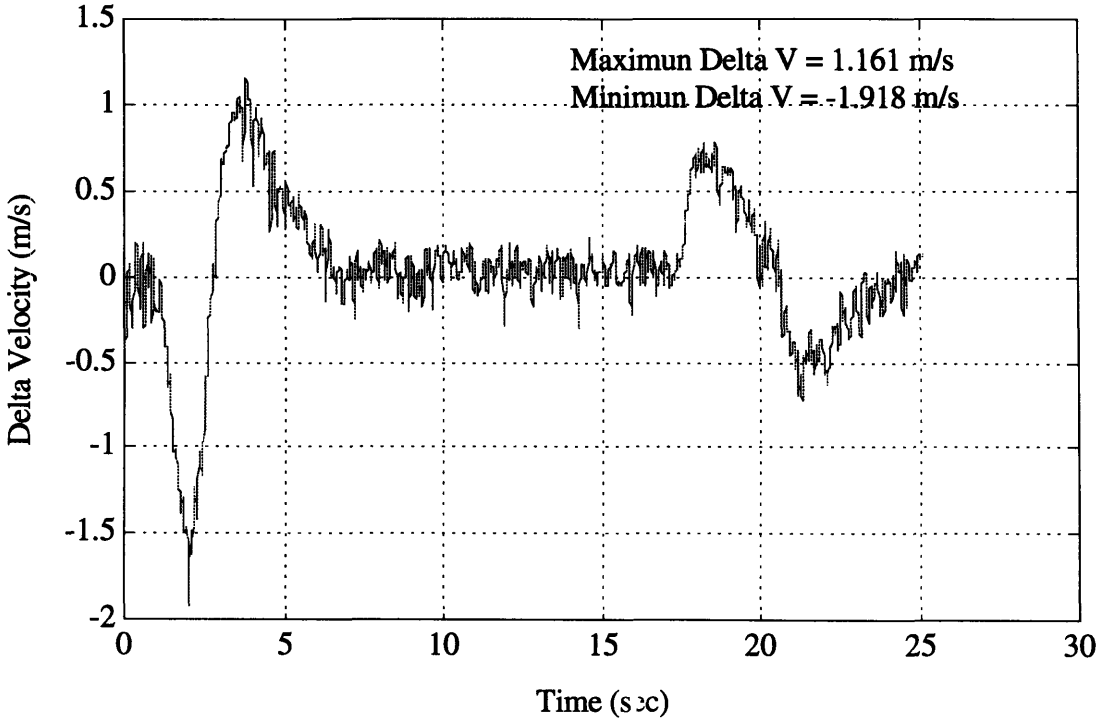

Figure 6.23c: Web Velocity Difference Seen Across Dancer

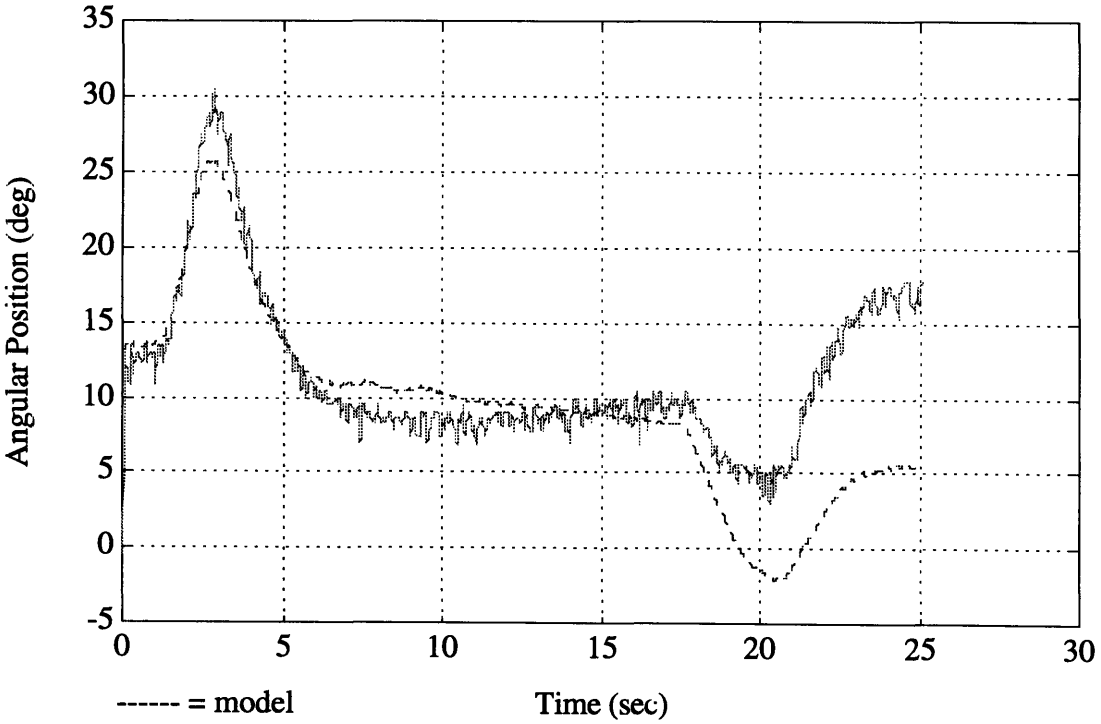

Figure 6.23d: Dancer Dynamic Transient (Model vs Actual)

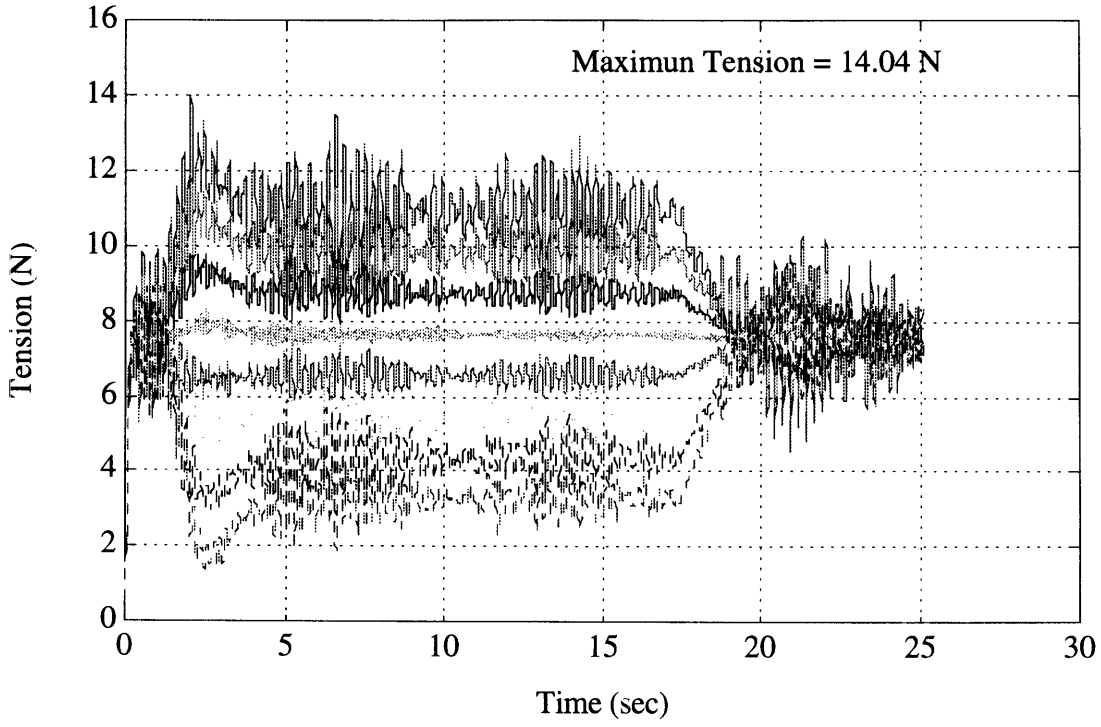

Figure 6.23e: Predicted Span Tensions

DOX 15

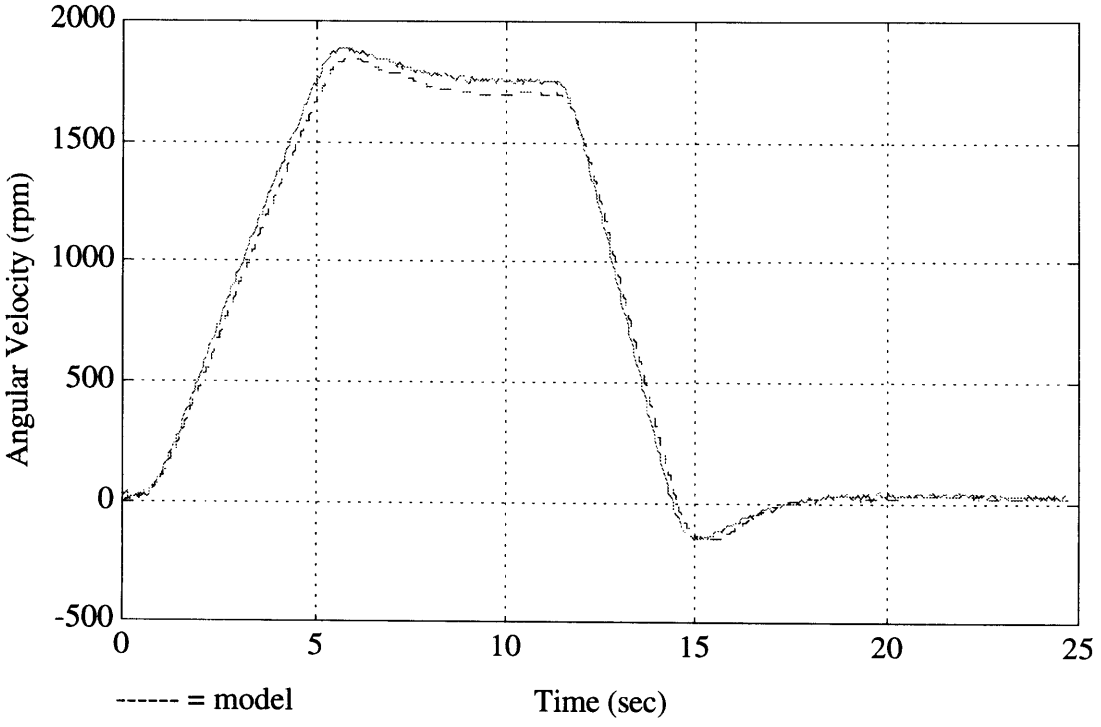

Figure 6.24a: Motor Speeds

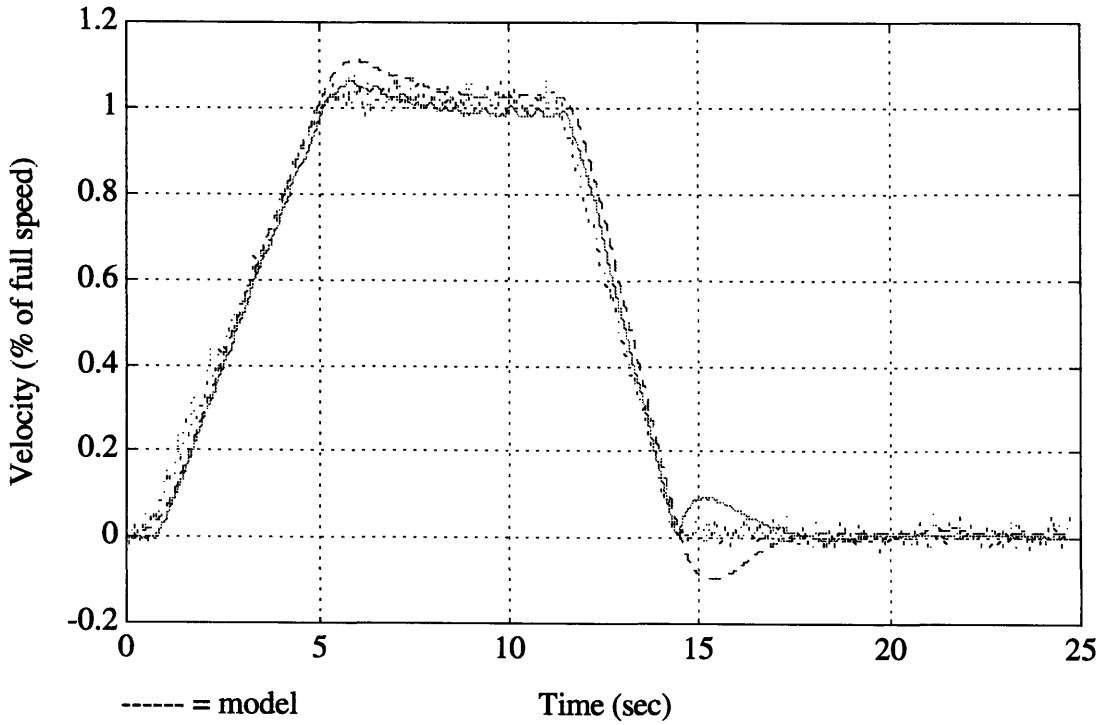

Figure 6.24b: Linear Web Speed and S-Wrap Metering Speed

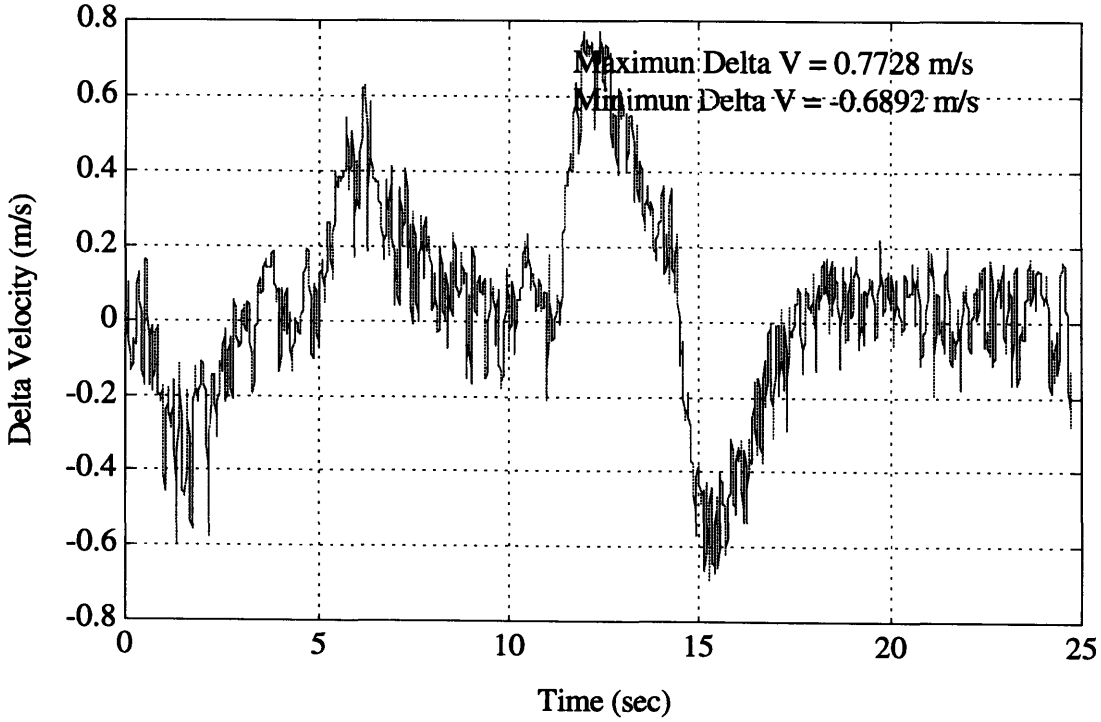

Figure 6.24c: Web Velocity Difference Seen Across Dancer

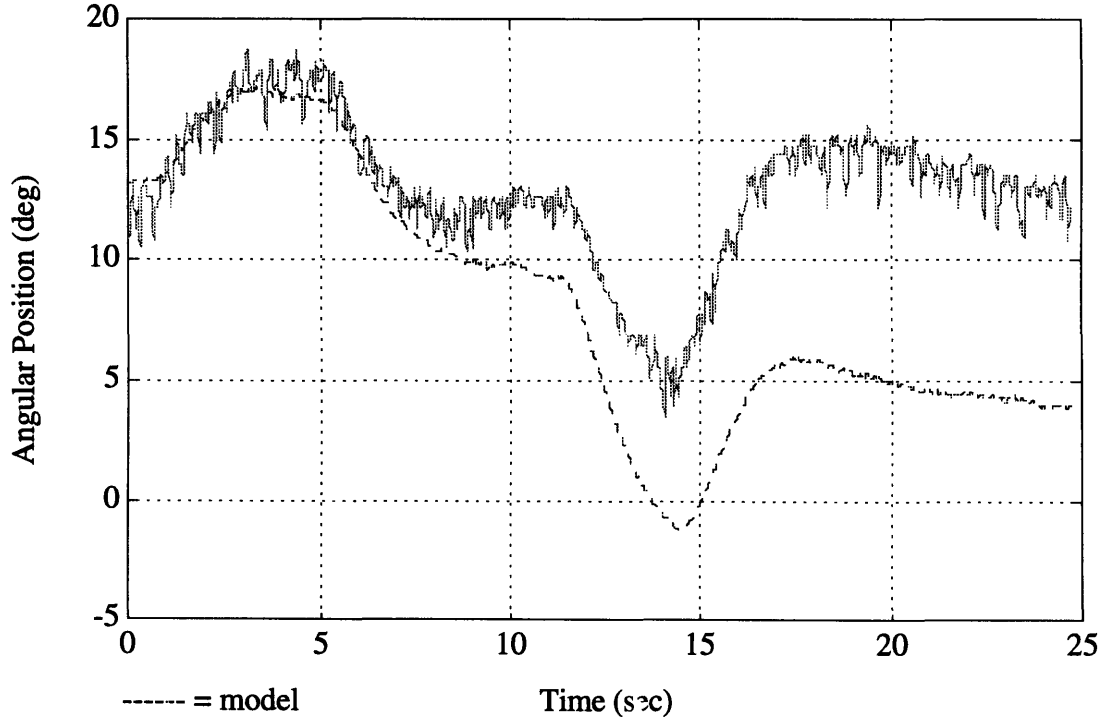

Figure 6.24d: Dancer Dynamic Transient (Model vs Actual)

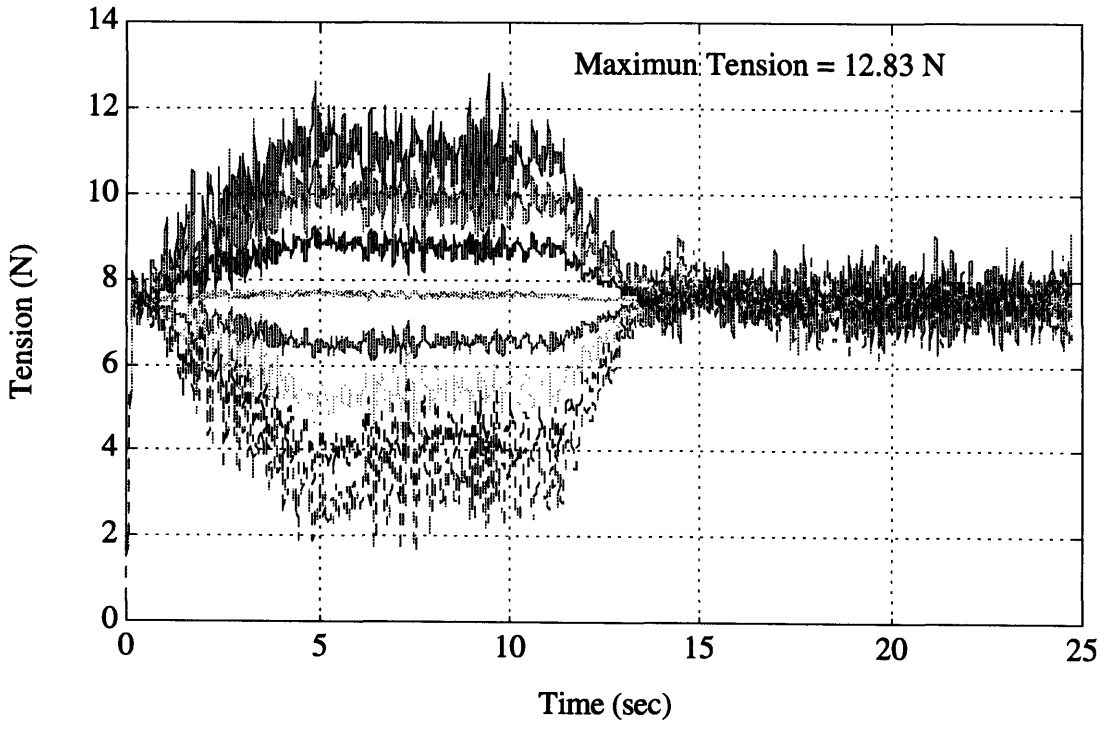

Figure 6.24e: Predicted Span Tensions

DOX 17

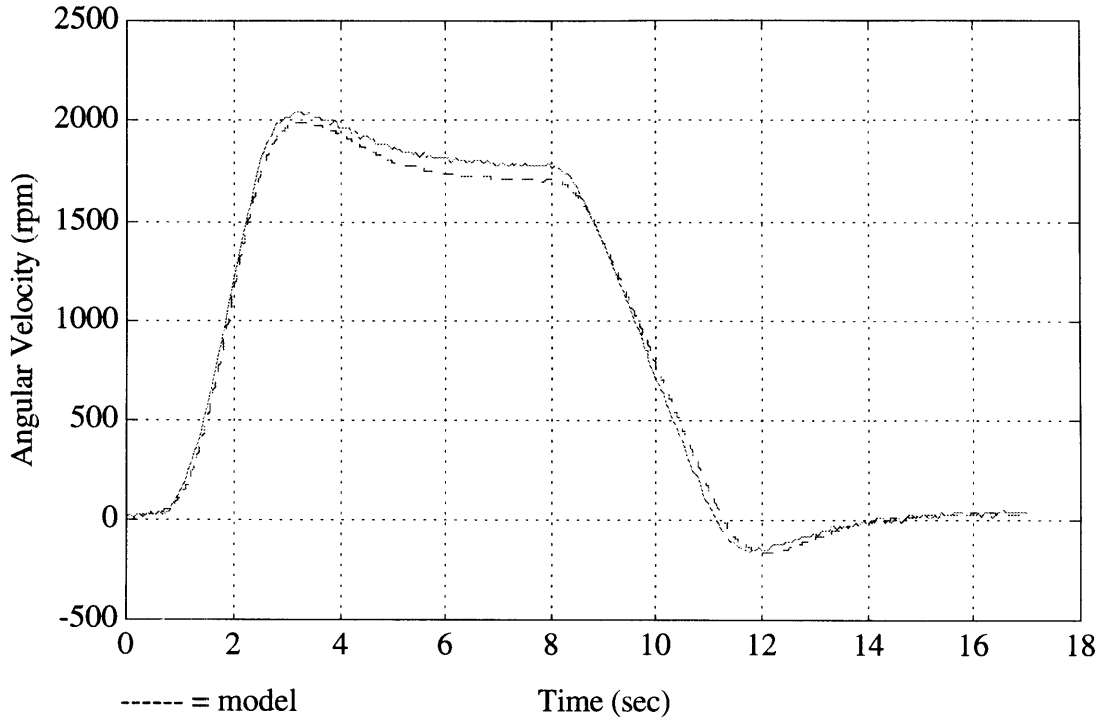

Figure 6.25a: Motor Speeds

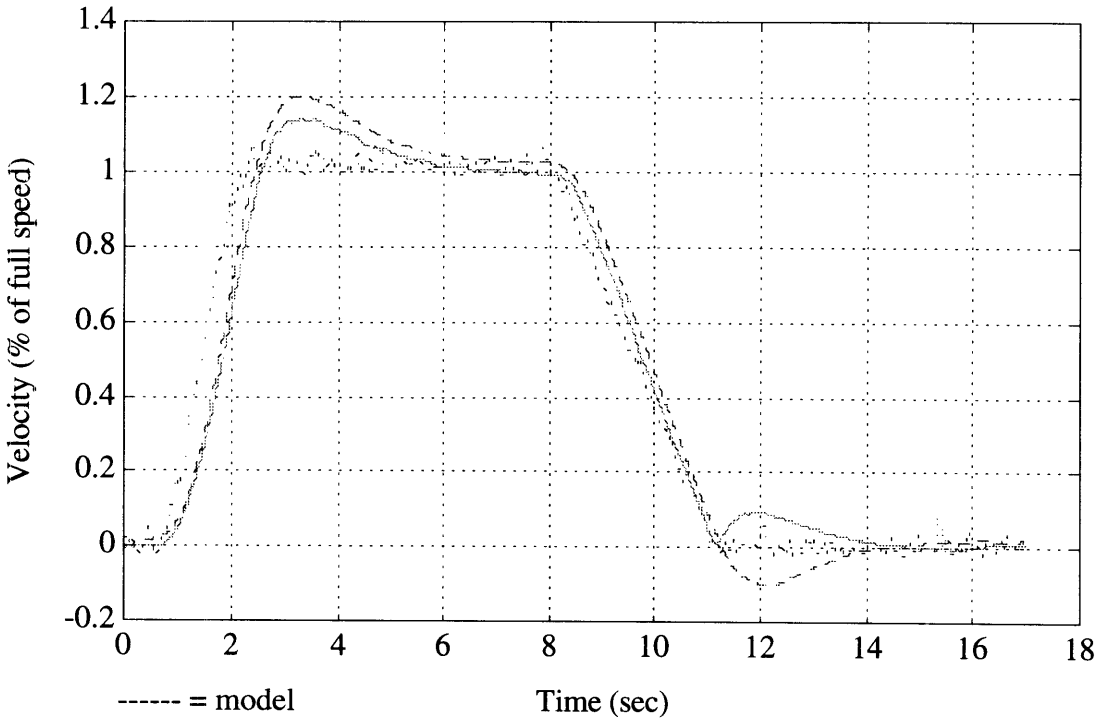

Figure 6.25b: Linear Web Speed and S-Wrap Metering Speed

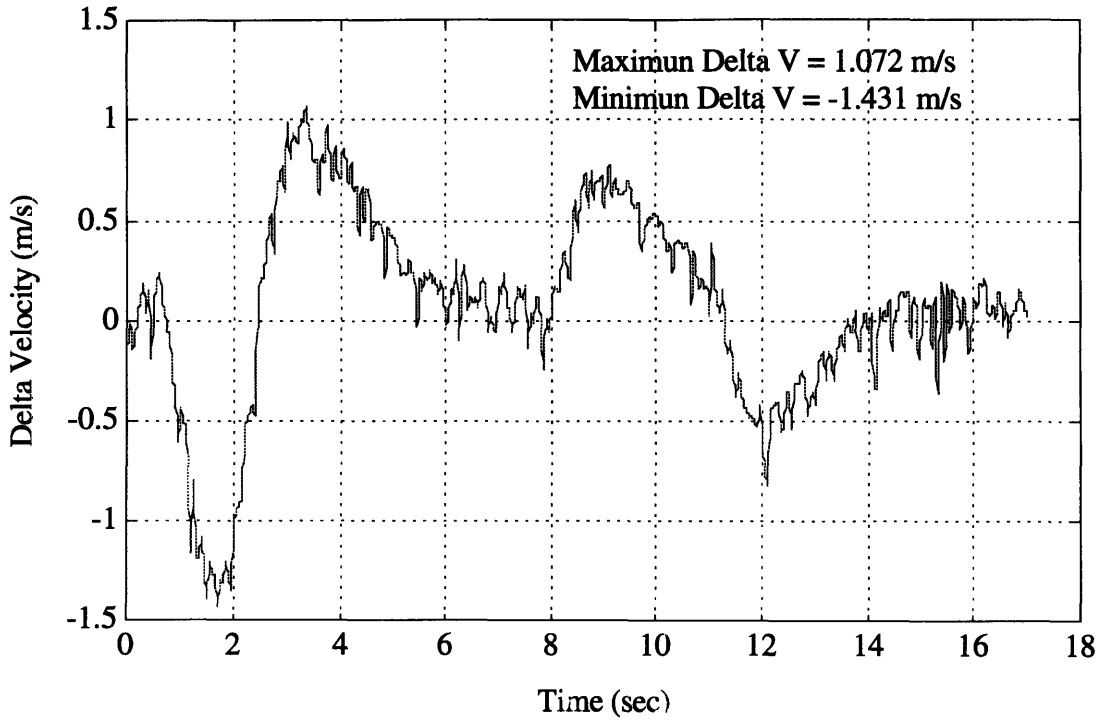

Figure 6.25c: Web Velocity Difference Seen Across Dancer

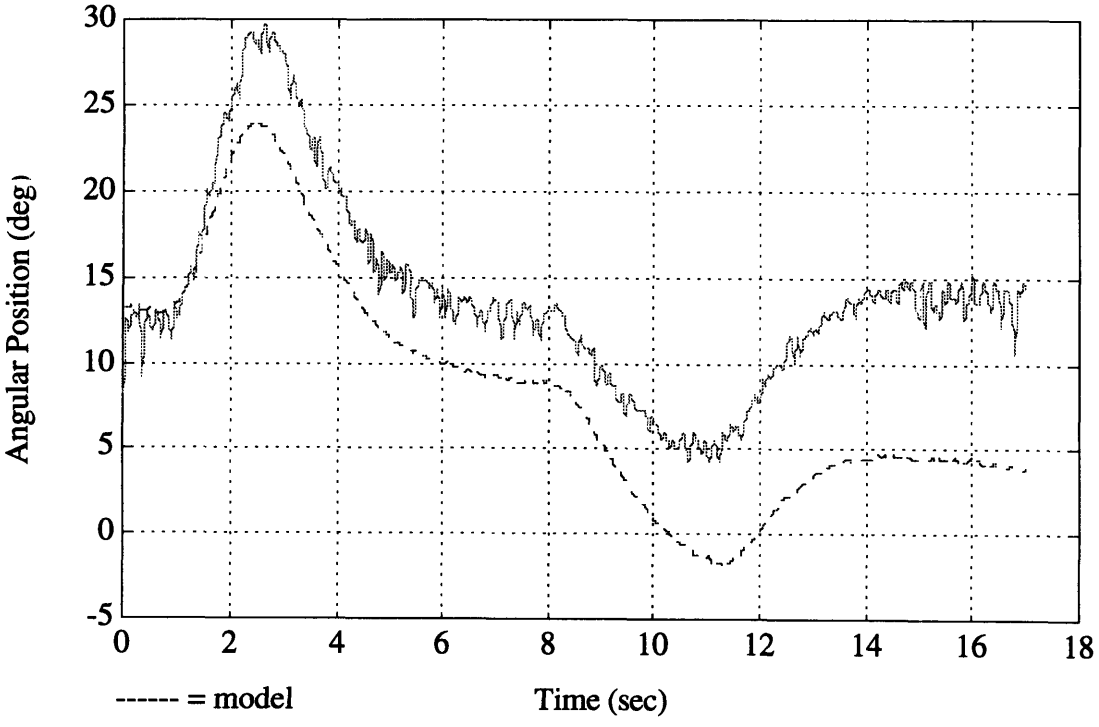

Figure 6.25d: Dancer Dynamic Transient (Model vs. Actual)

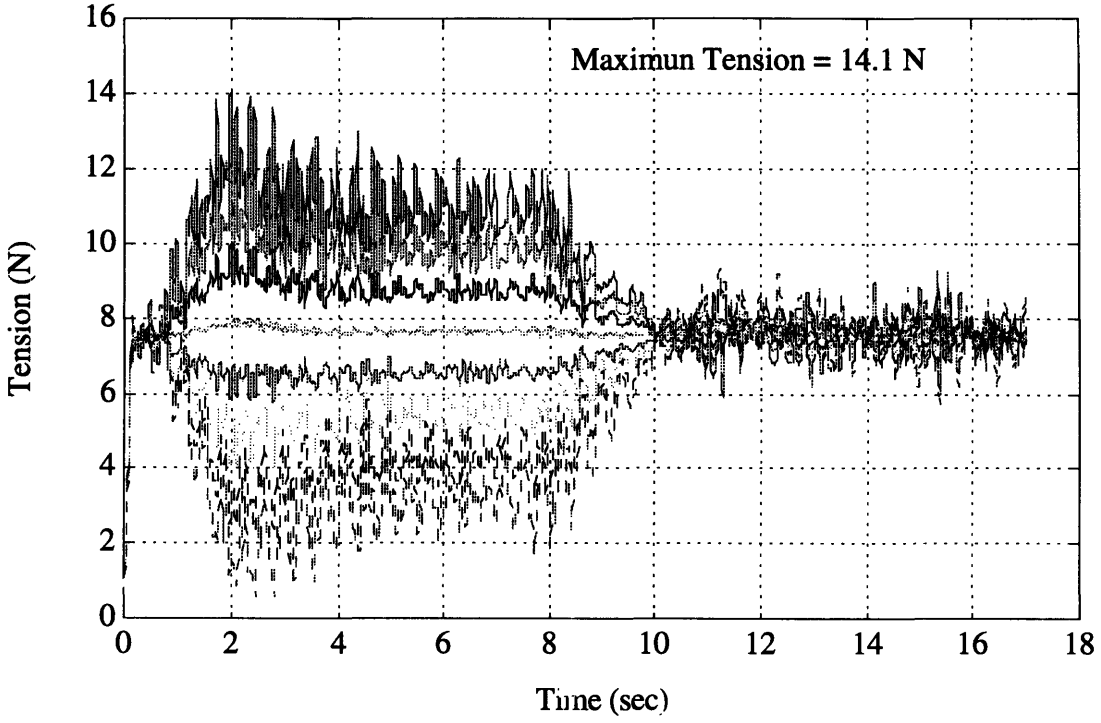

Figure 6.25e: Predicted Span Tensions

DOX 3

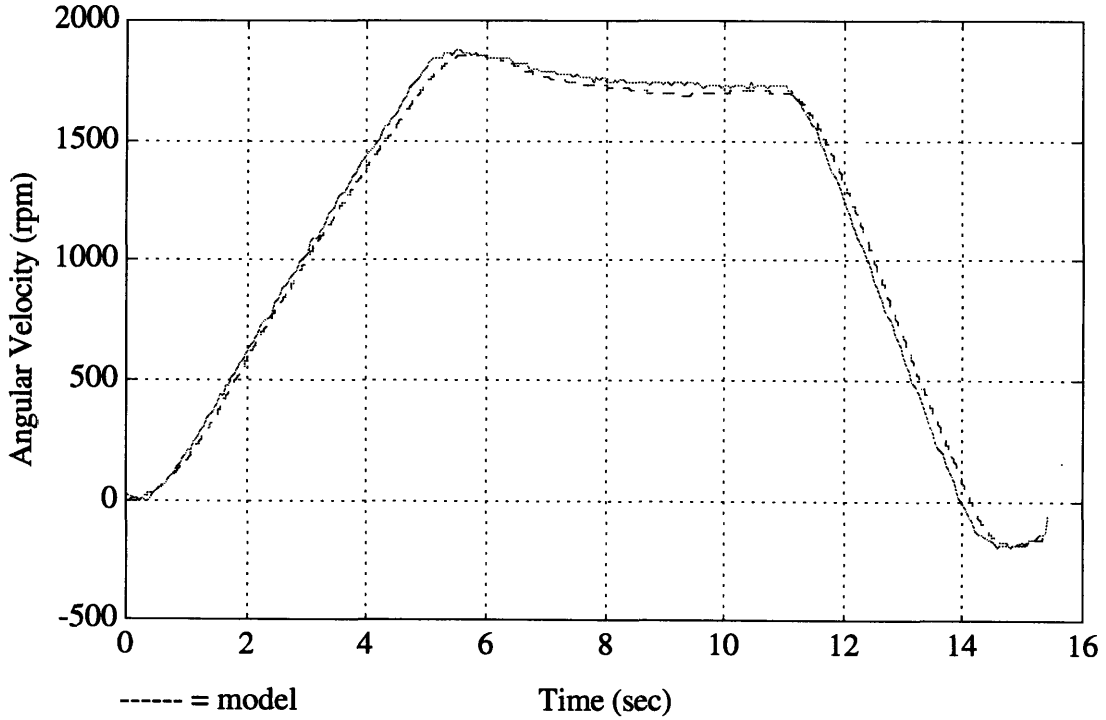

Figure 6.26a: Motor Speeds

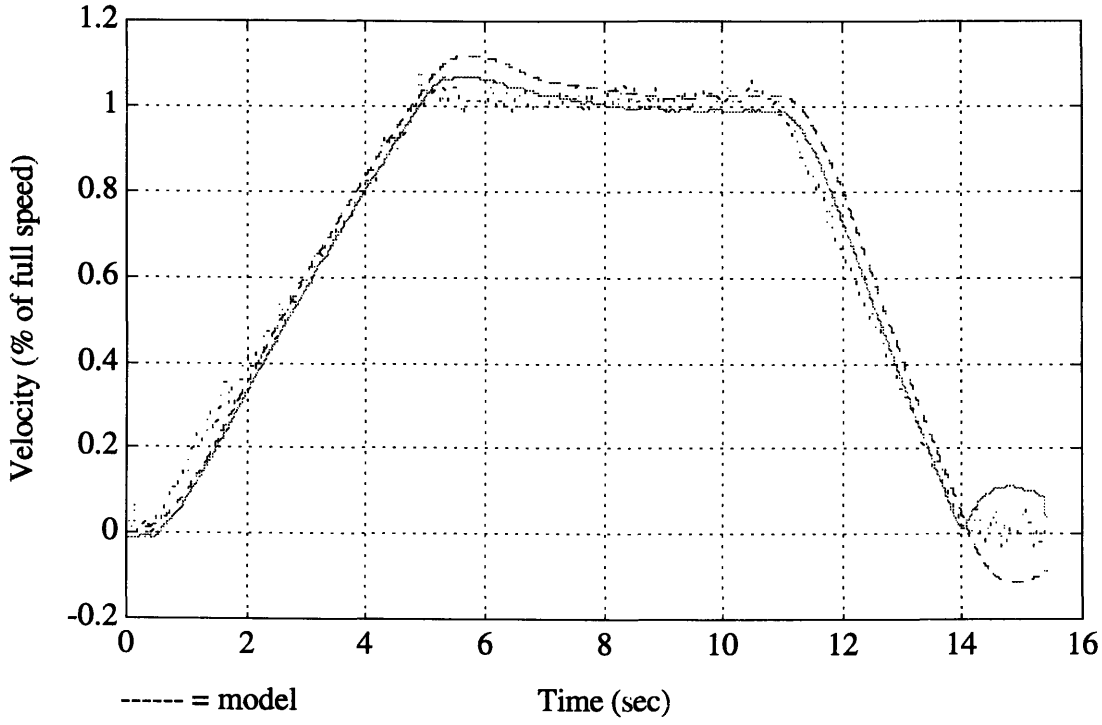

Figure 6.26b: Linear Web Speed and S-Wrap Metering Speed

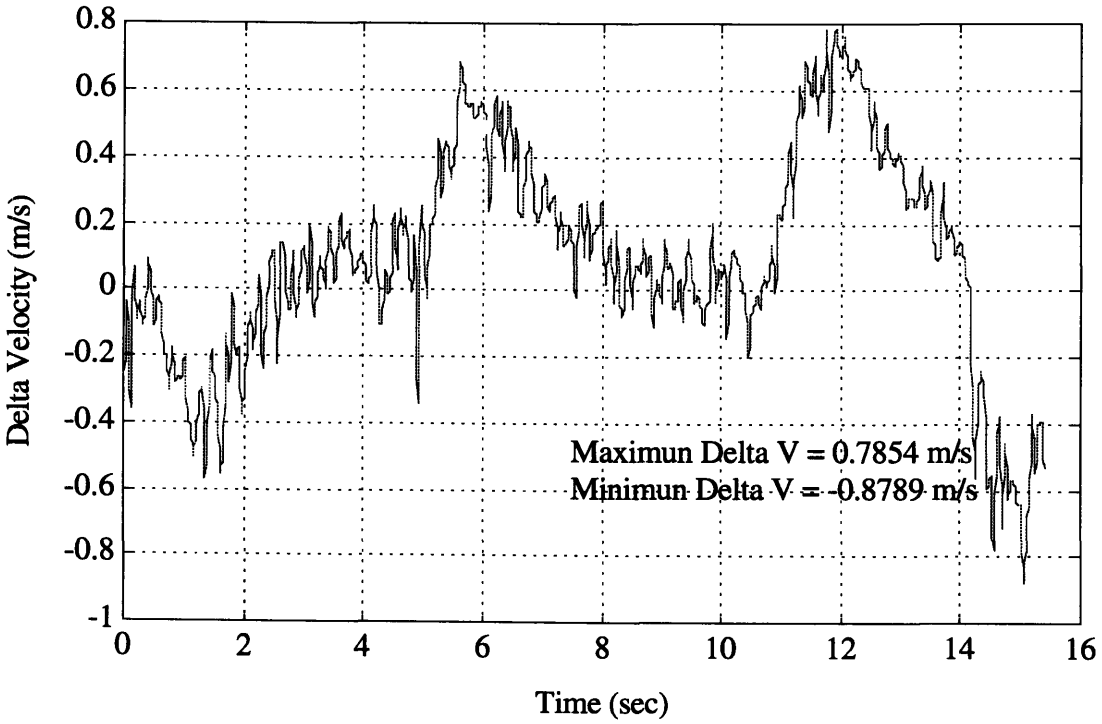

Figure 6.26c: Web Velocity Difference Seen Across Dancer

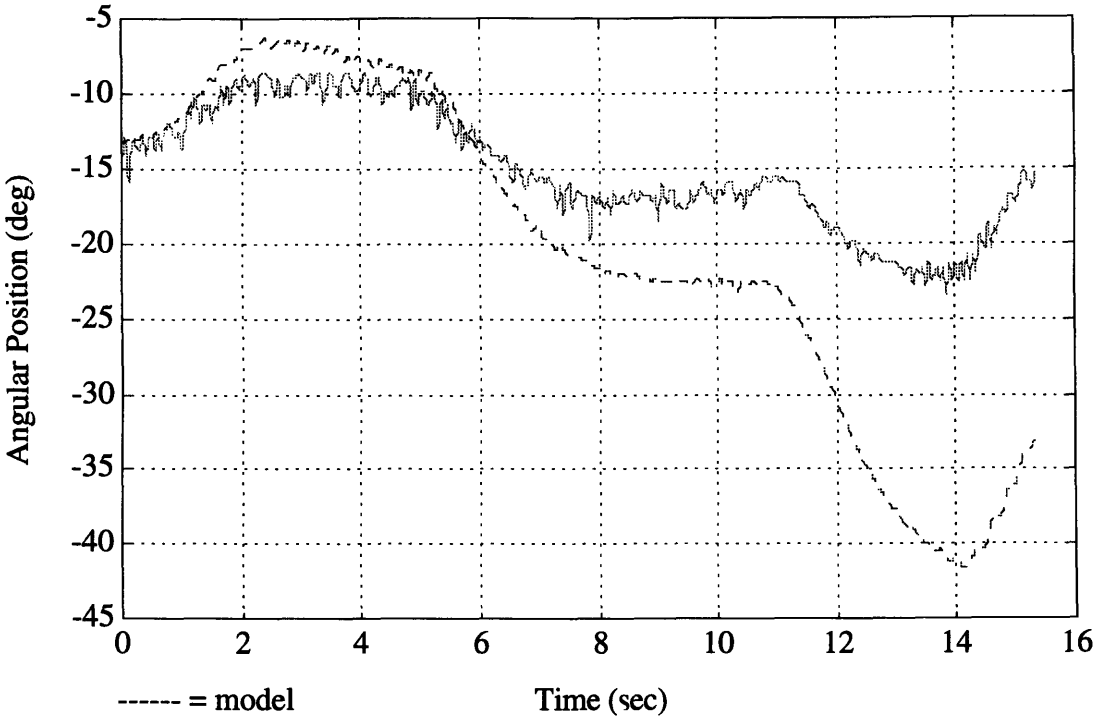

Figure 6.26d: Dancer Dynamic Transient (Model vs. Actual)

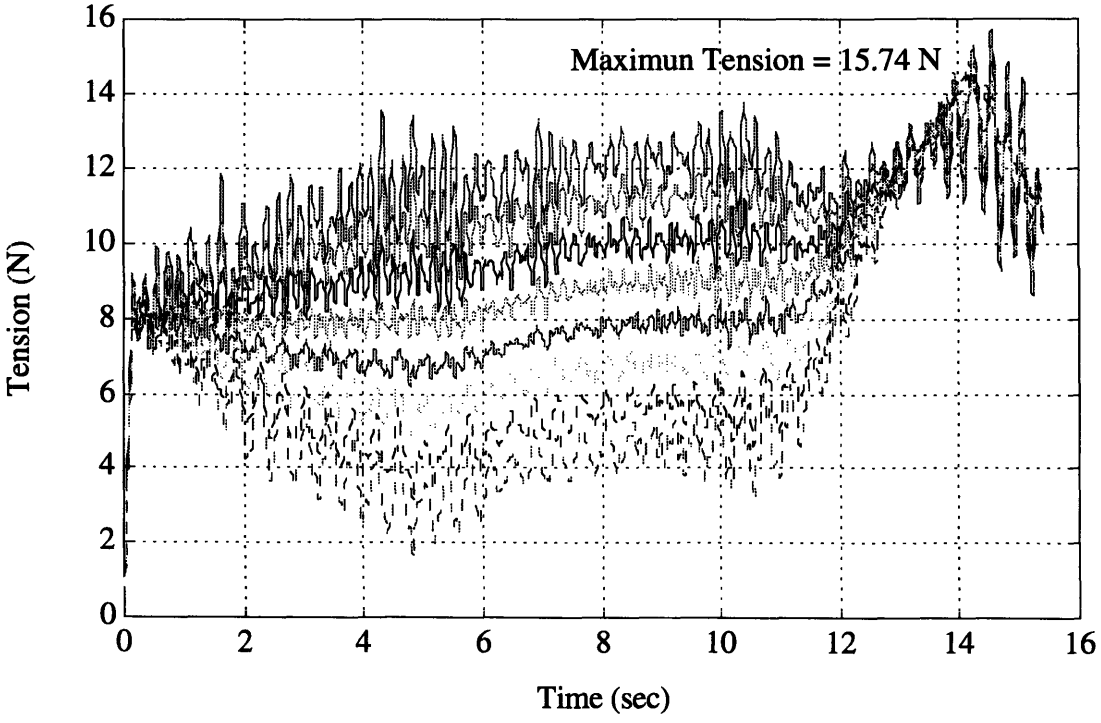

Figure 6.26e: Predicted Span Tensions

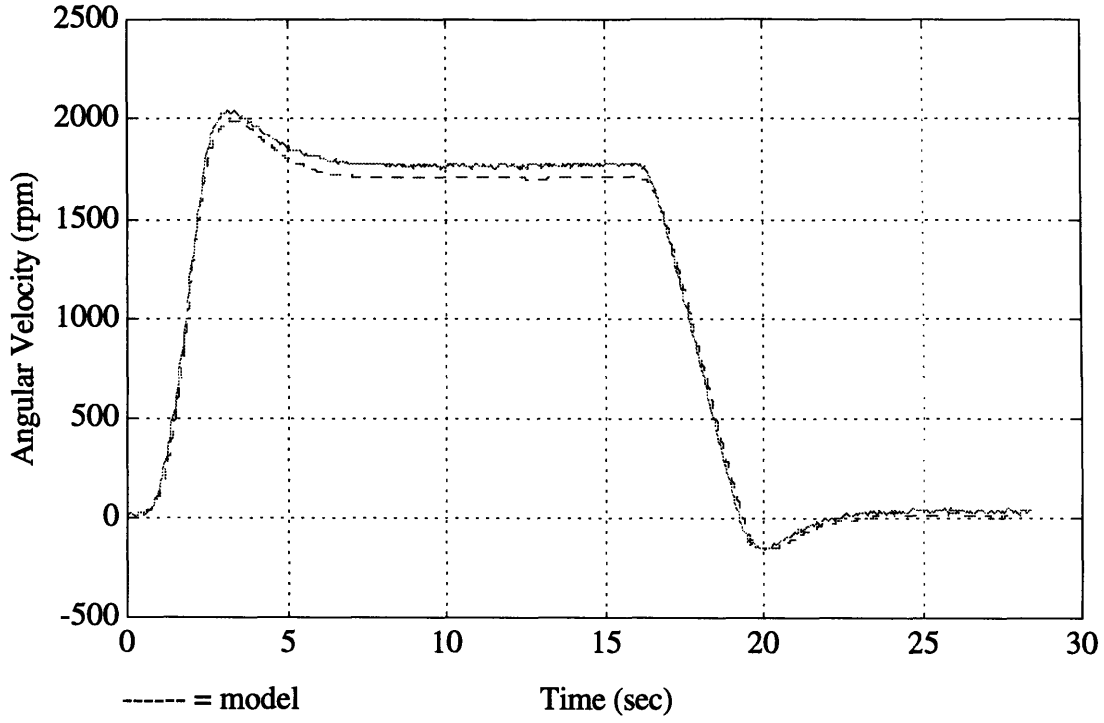

Figure 6.27a: Motor Speeds

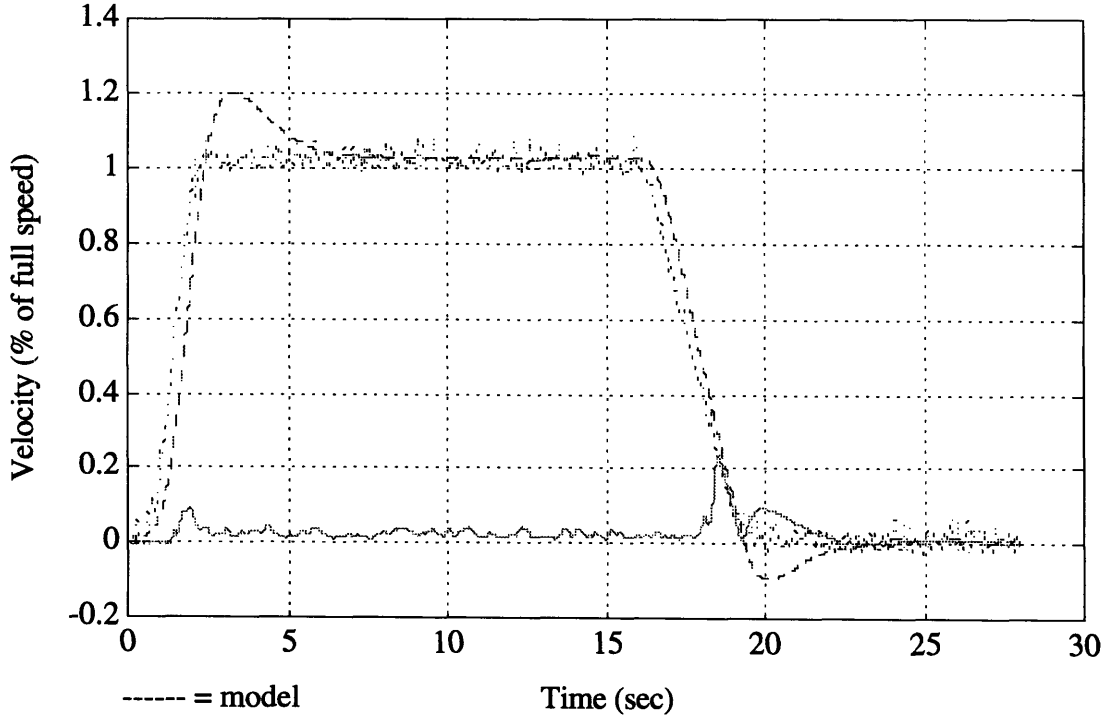

Figure 6.27b: Linear Web Speed and S-Wrap Metering Speed

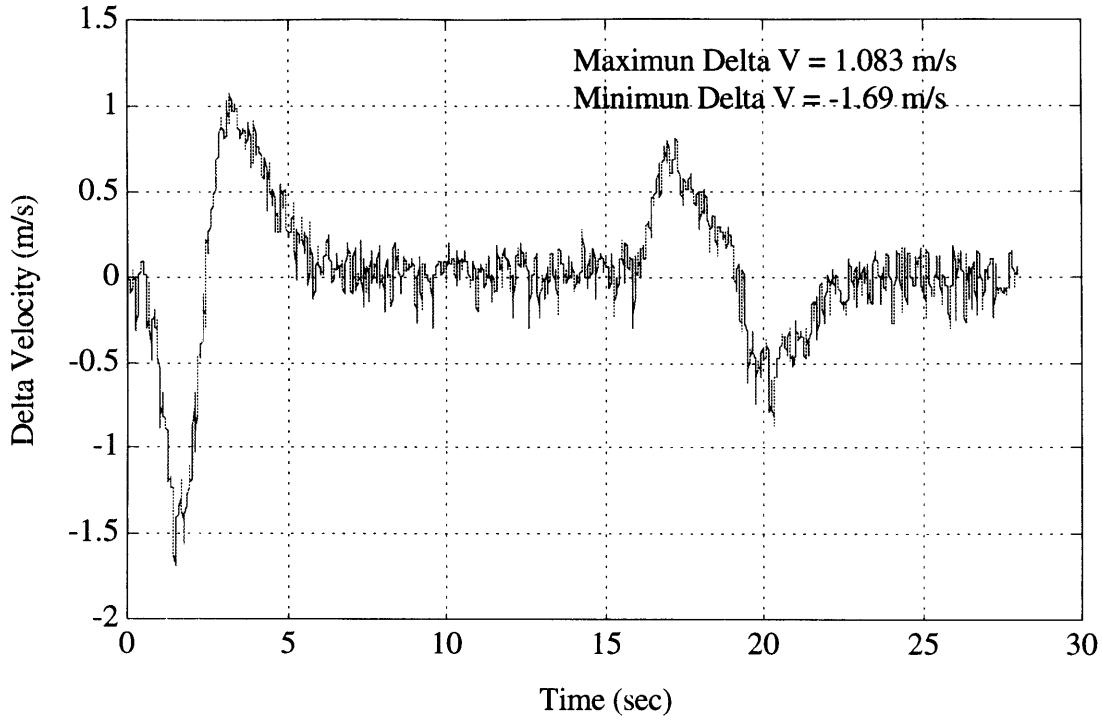

Figure 6.27c: Web Velocity Difference Seen Across Dancer

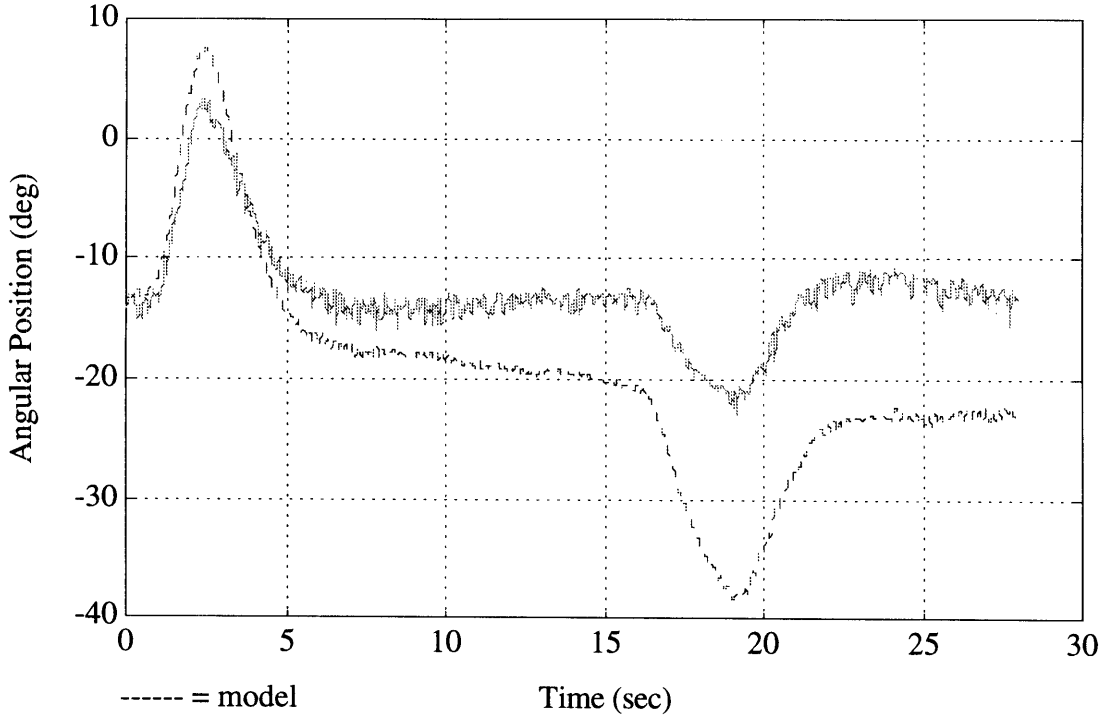

Figure 6.27d: Dancer Dynamic Transient (Model vs. Actual)

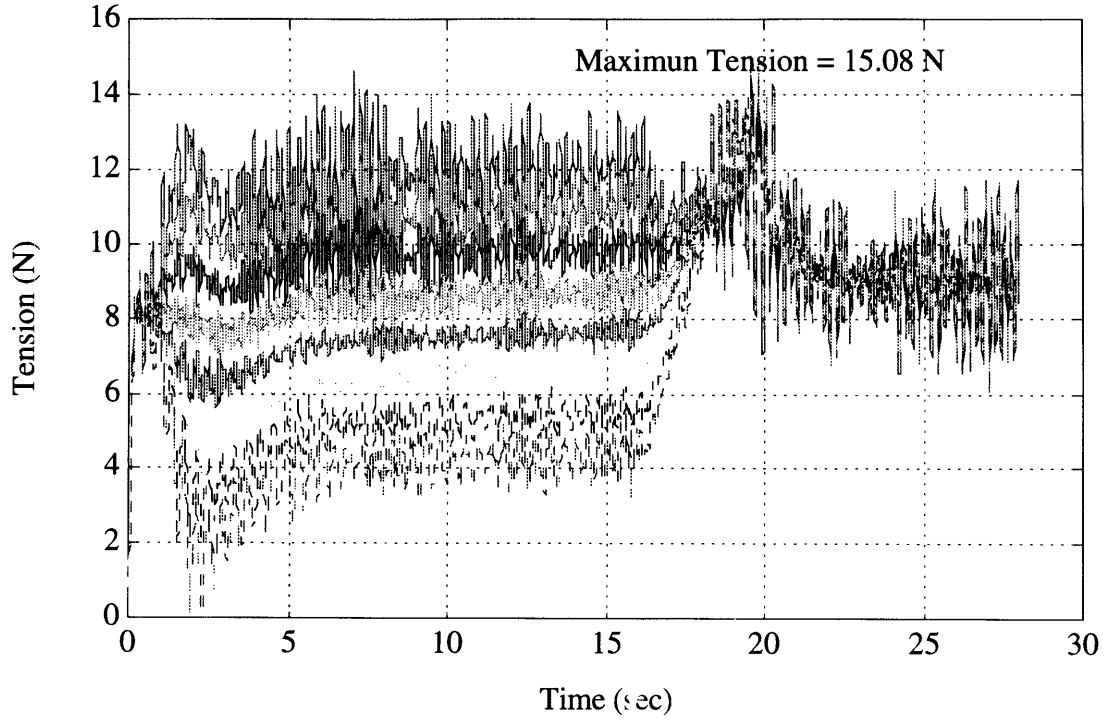

Figure 6.27e: Predicted Span Tensions

DOX 1

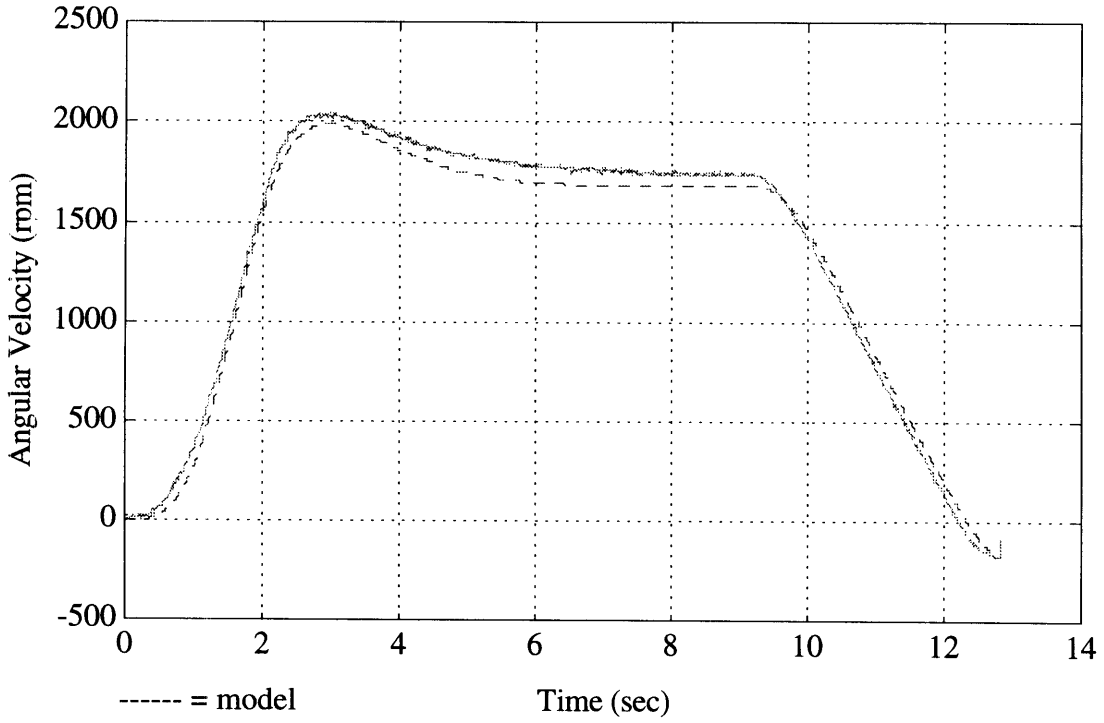

Figure 6.28a: Motor Speeds

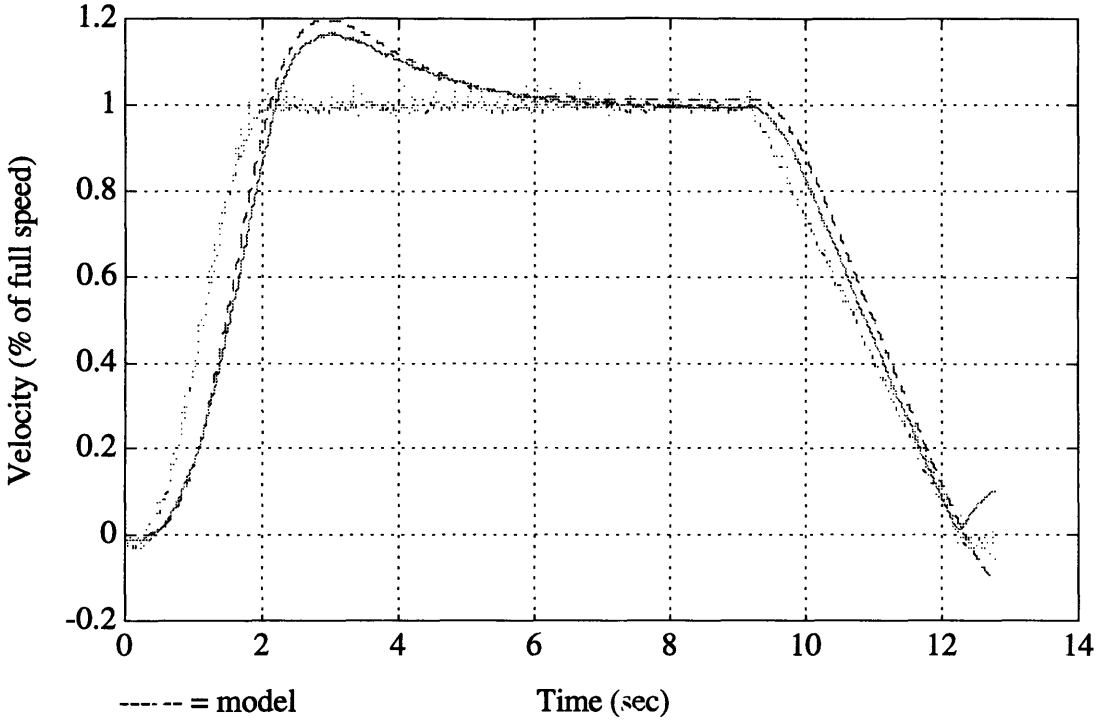

Figure 6.28b: Linear Web Speed and S-Wrap Metering Speed

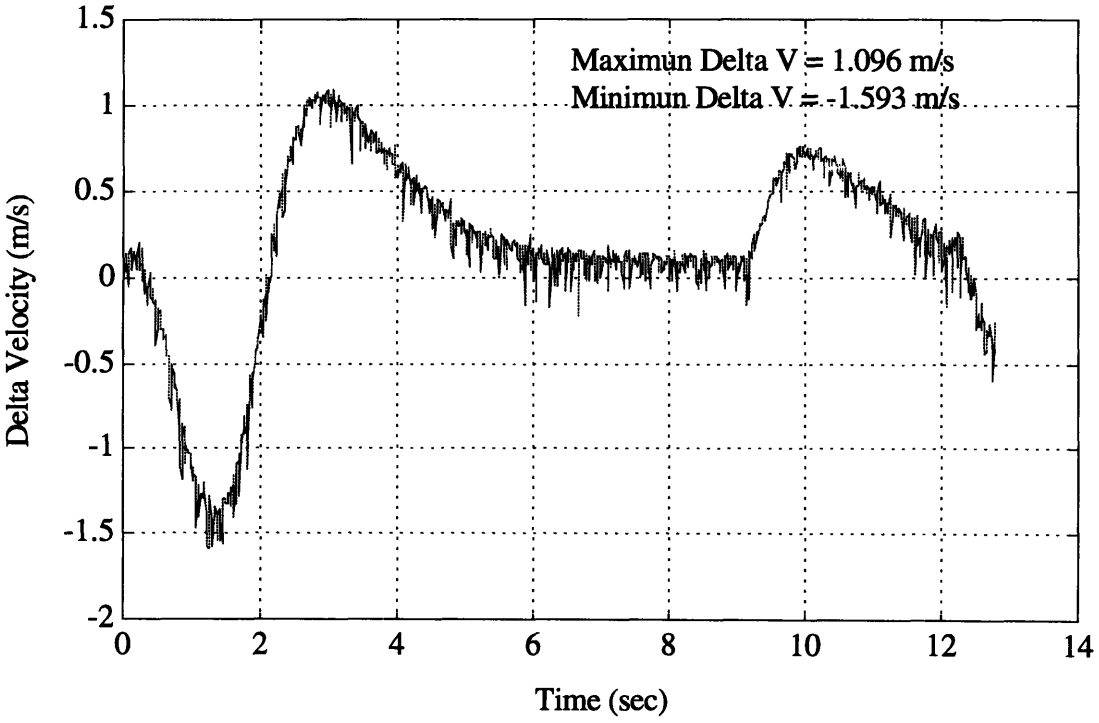

Figure 6.28c: Web Velocity Difference Seen Across Dancer

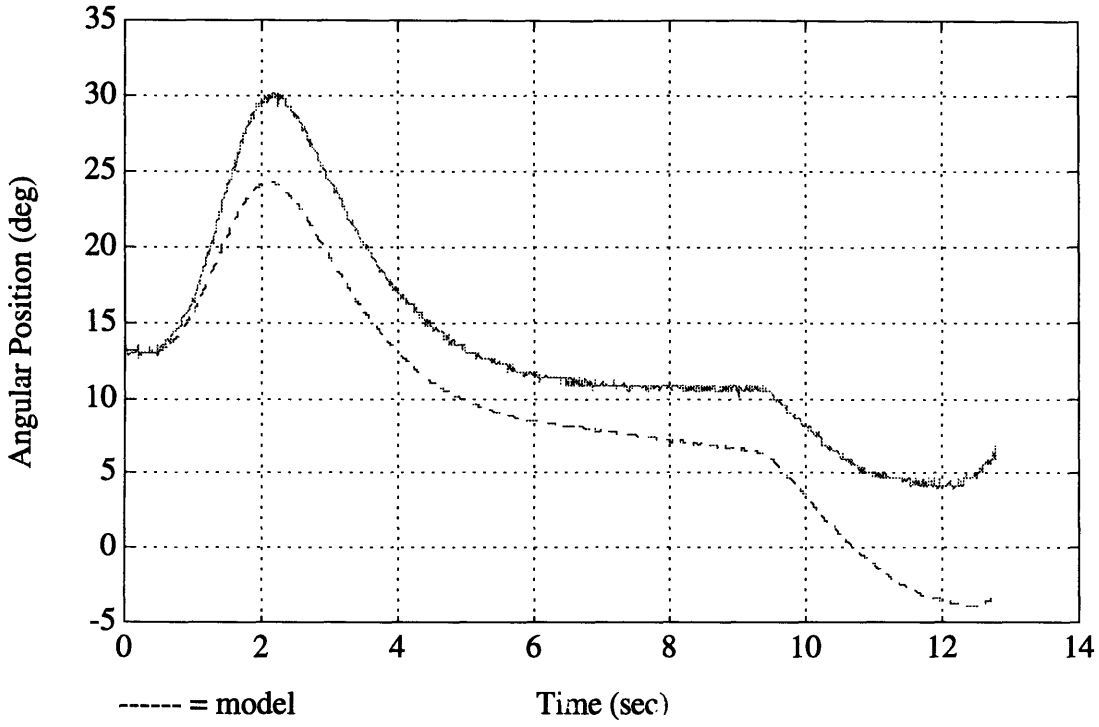

Figure 6.28d: Dancer Dynamic Transient (Model vs Actual)

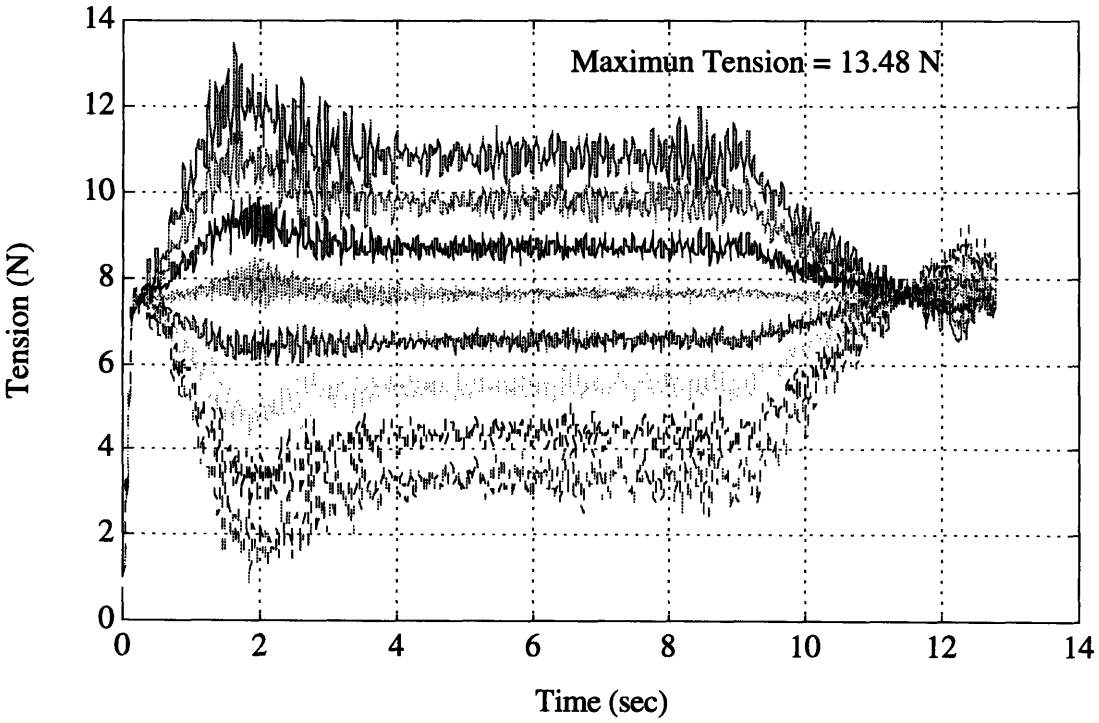

Figure 6.28e: Predicted Span Tensions

DOX 11

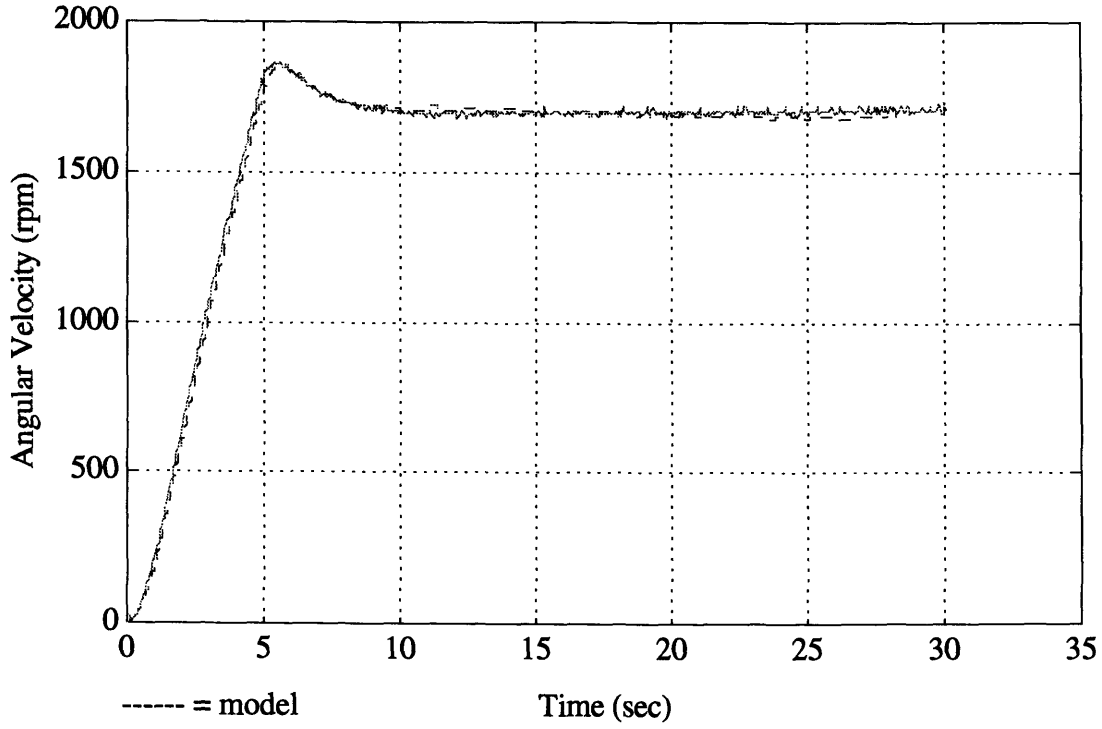

Figure 6.29a: Motor Speeds

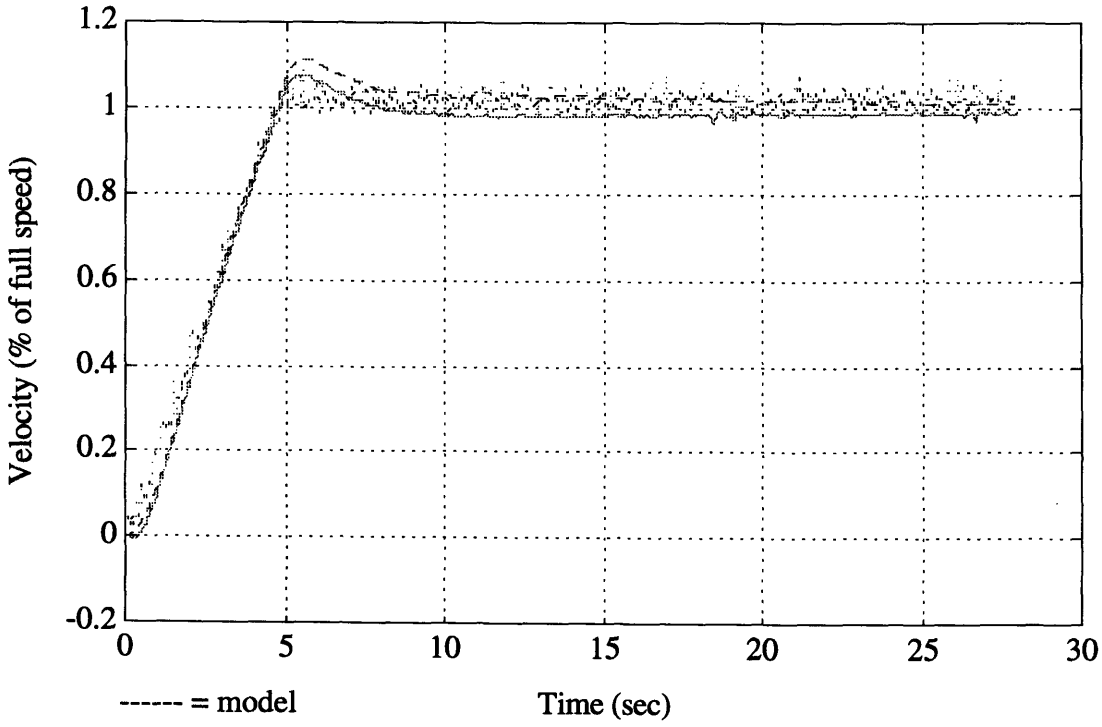

Figure 6.29b: Linear Web Speed and S-Wrap Metering Speed

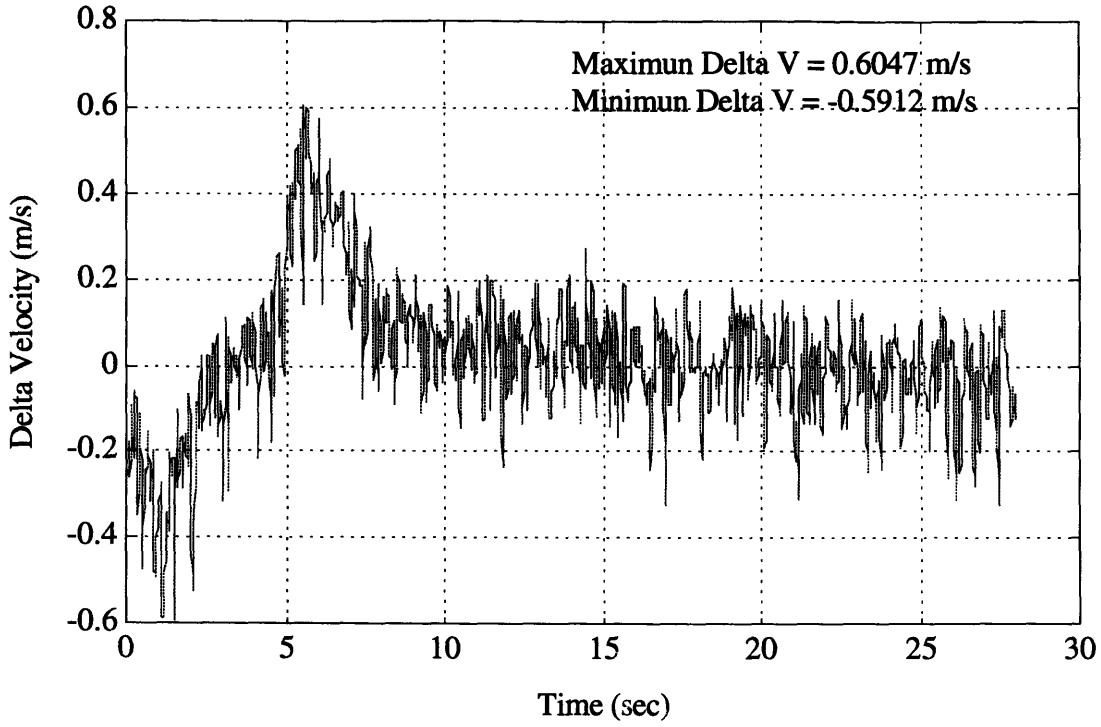

Figure 6.29c: Web Velocity Difference Seen Across Dancer

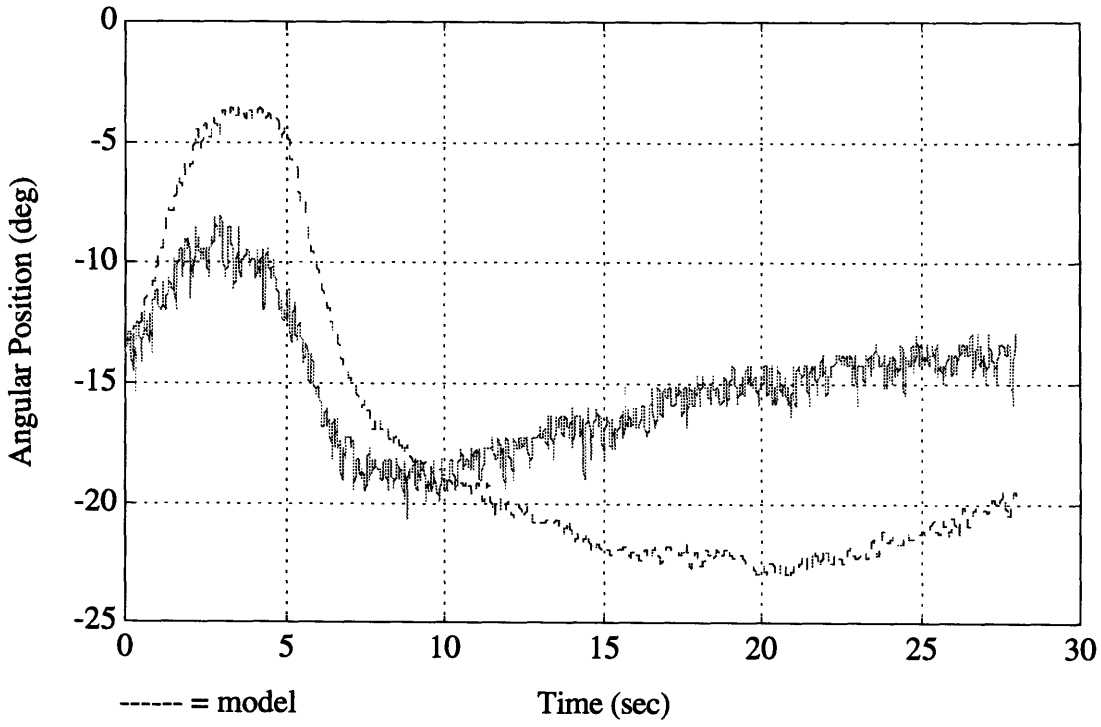

Figure 6.29d: Dancer Dynamic Transient (Model vs Actual)

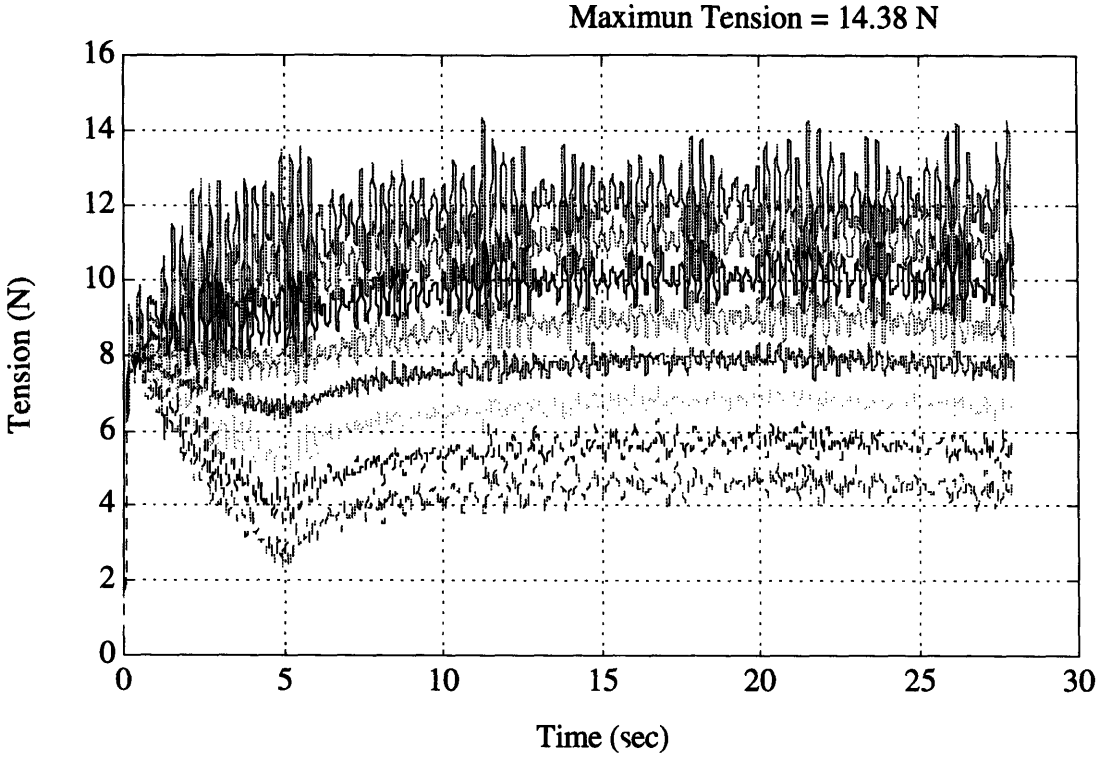

Figure 6.29e: Predicted Span Tensions

DOX 16

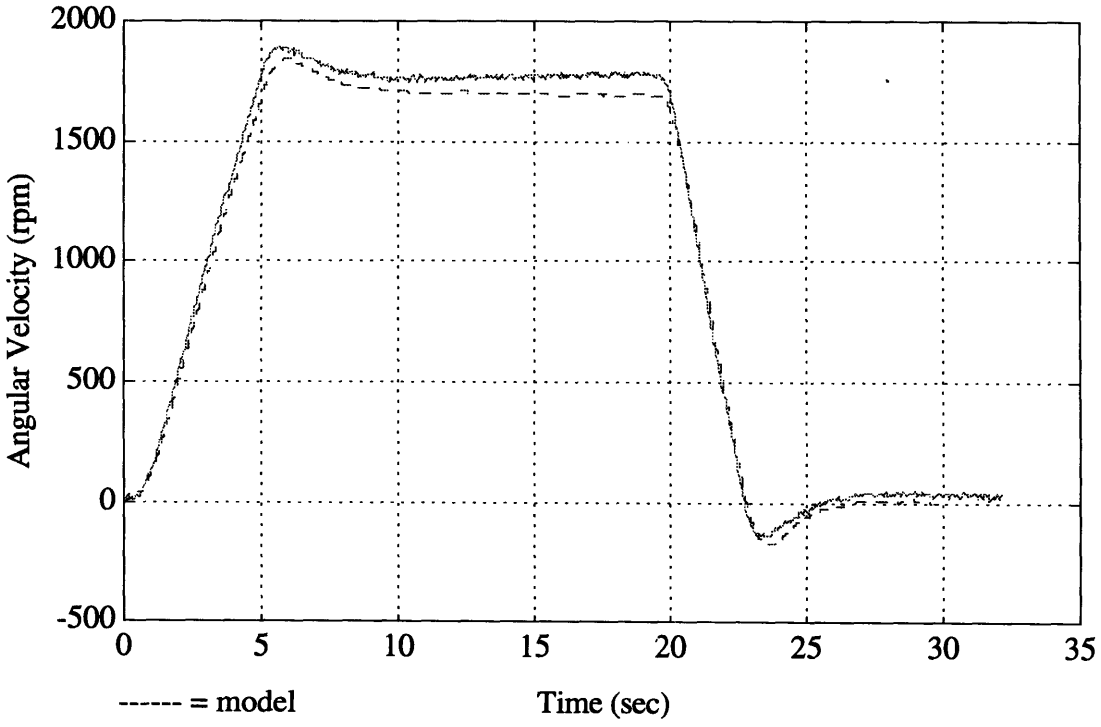

Figure 6.30a: Motor Speeds

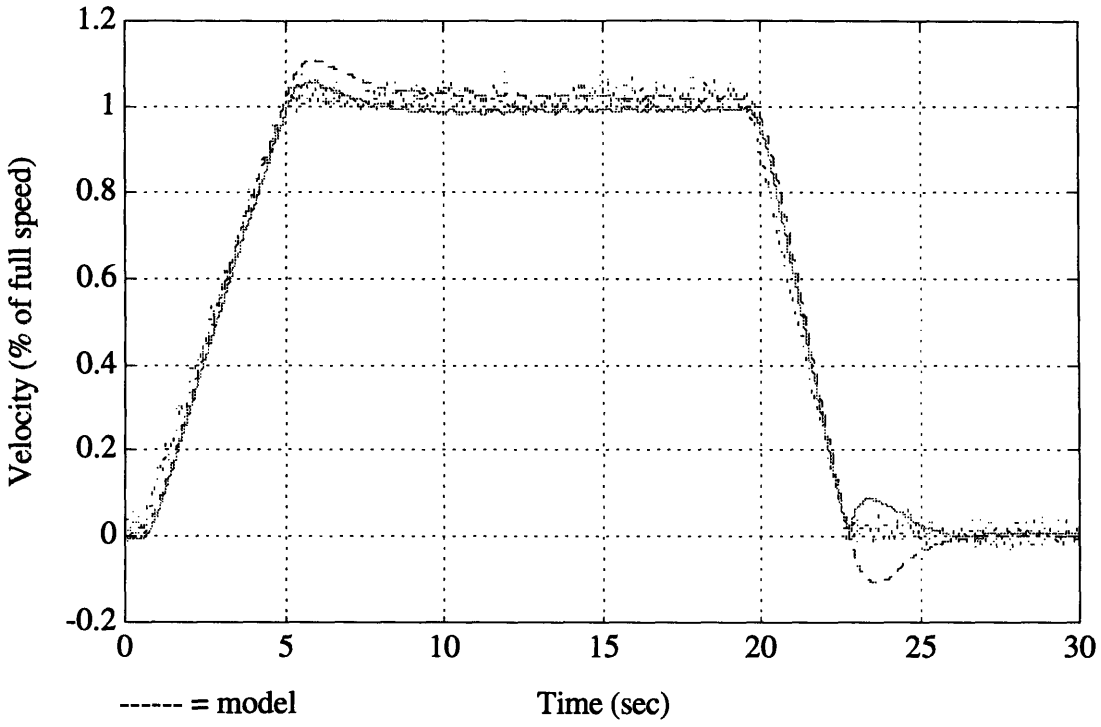

Figure 6.30b: Linear Web Speed and S-Wrap Metering Speed

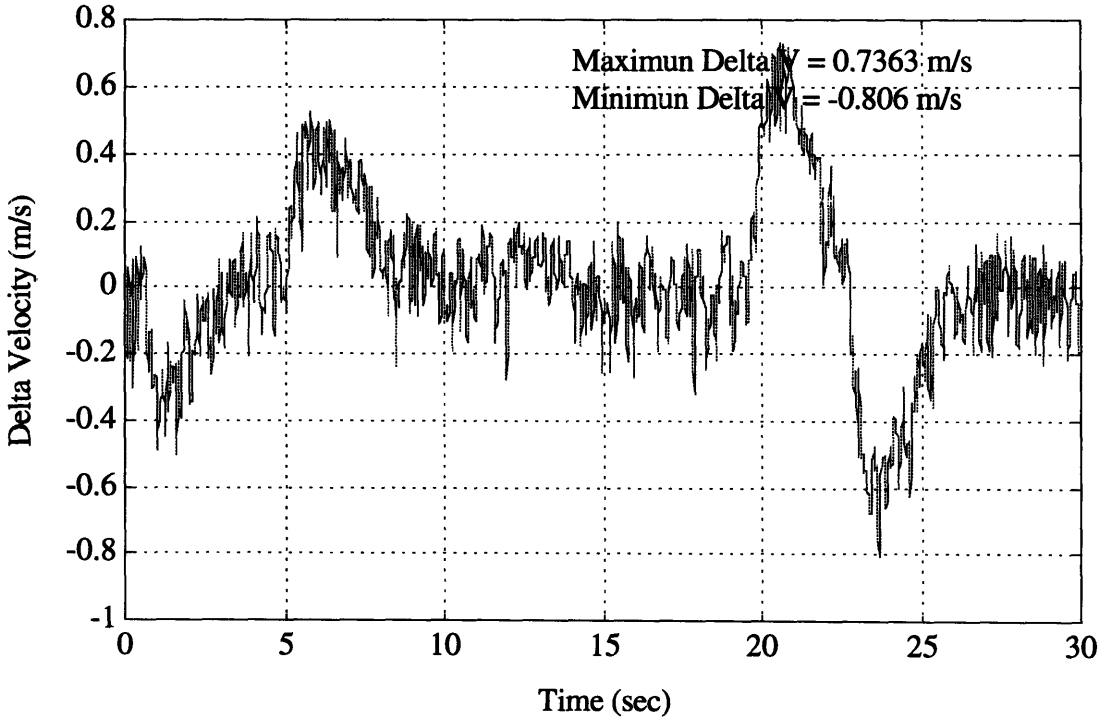

Figure 6.30c: Web Velocity Difference Seen Across Dancer

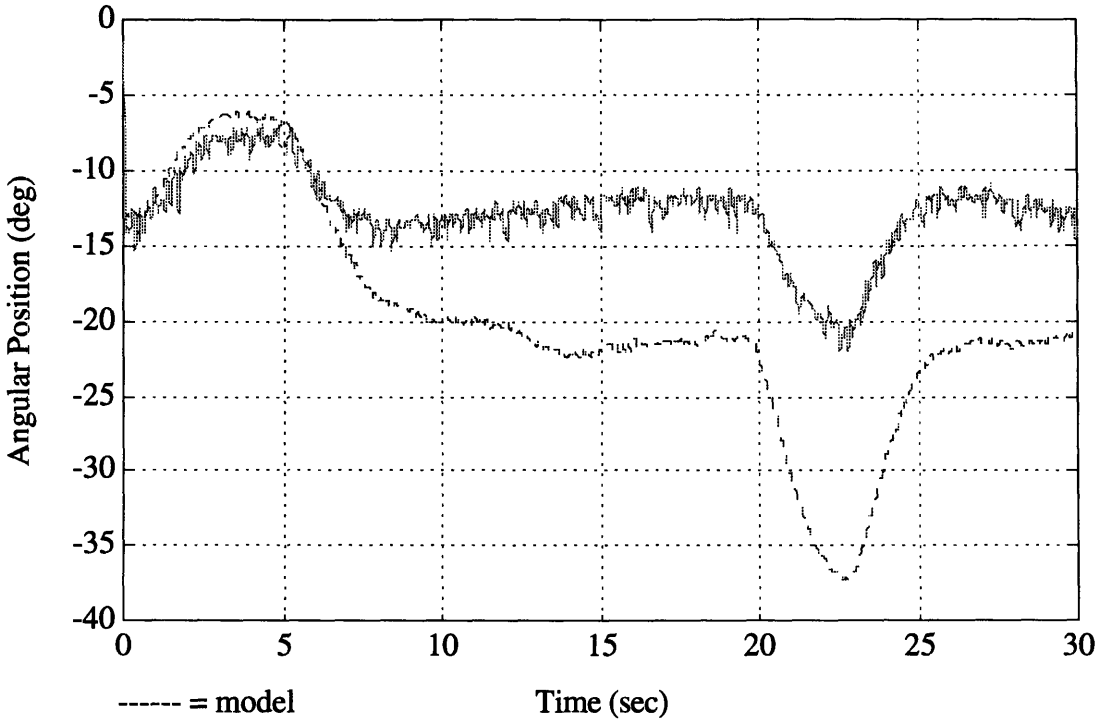

Figure 6.30d: Dancer Dynamic Transient (Model vs Actual)

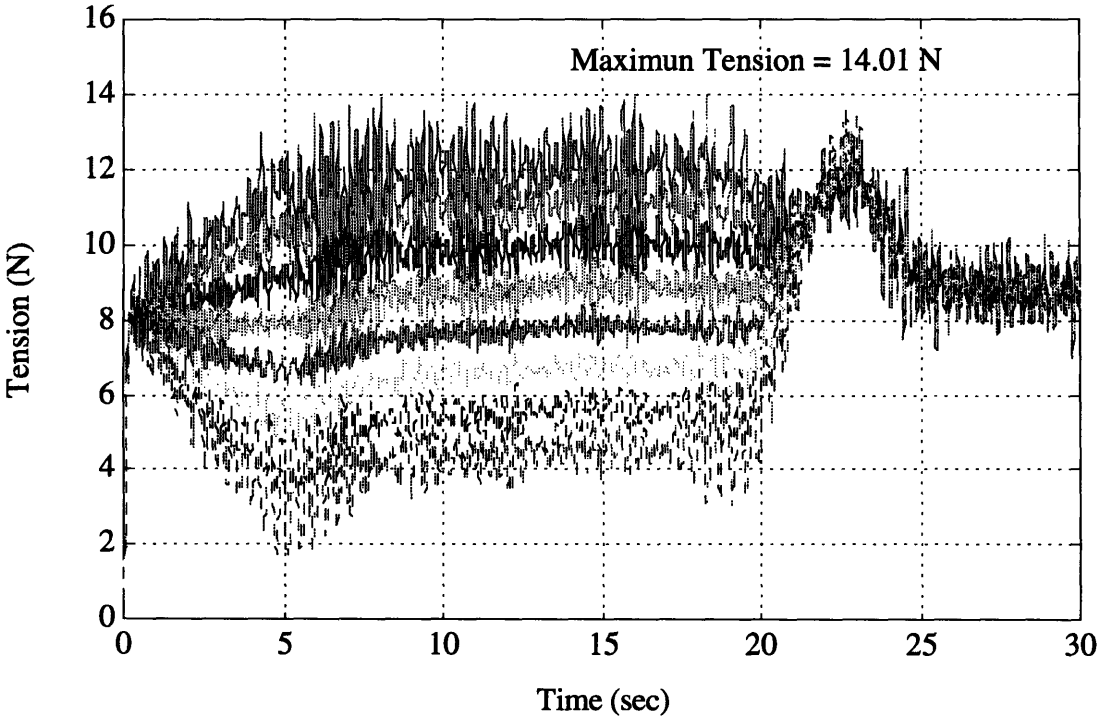

Figure 6.30e: Predicted Span Tensions

One of the main limitations of the model is very visible in the tension plots. The first four spans of the dancer experience a negative tension at steady state. This is tolerated by the model because the spans are modeled as non-linear, but discrete springs. In the actual process, we know that the web cannot be under compression and cannot push on the idlers. Thus we can conclude that it is very likely that in the actual process all the tensions are offset upwards so that the lowest tension is still positive.

All of the tension estimate plots present high frequency oscillations. This is due to the combination of low inertia idlers and low material modulus which results in high natural frequencies. These sharp peak in the tensions hint at one of the causes for the unreliability of the unwind unit. If the values of the tensions for a given instant in time are compared, in some cases the highest tension in the web will not be in the span prior to the metering point, but might occur in a span prior to that point. That is, there are localized peak stresses in the web as well as high frequency oscillations that travel along the material. When these localized stresses coincide with a spot of low strength in the material strength distribution a breakout occurs.

An alternate modeling approach will be presented in the conclusions of this thesis. This distributed parameter model captures the localized nature of stress distributions in the material and can be used as a material state estimator. Estimating material states enables a controller design that regulates material states rather than machine states and insures higher reliability.

Chapter 7

Conclusions and Recommendations

7.1 Benefits of Statistic and Dynamic Modeling

The combination of reliability analysis and deterministic dynamic modeling and control system analysis is a valuable tool for the improvement of complex manufacturing systems. Two methods for characterizing system failures have been successfully applied.

The first method, suspended item analysis, can be used to determine failure rates as a function of time as well as instantaneous and cumulative failure probability distributions. It has been shown that when the time domain in which hazard functions decrease coincides with the time domain of dynamic transients, premature failure can be attributed to uncontrolled dynamics. This is evident if the sharp decrease in the 0-1 min. region of the hazard function of the unwind unit (Figure 2.16) is compared with the 50 second transient of the dancer motion (Figure 5.3c).

Once the connection that exists between decreasing hazard functions (premature failure) and start-up transients was identified, a method to determine the stress distribution that induces failures was developed. This second method is an interference model that based on system unreliability, and system strength distributions gives an estimate on the region of stress that results in failures (refer to Figure 2.16). With these stress distributions available, control system designs can be evaluated and their effect on stress distributions and reliability assessed.

The value of the interference model is that it provides the link between the probabilistic characterization of system behavior and a dynamic model. The interference model maps the unreliability of the system into a stress region that can be compared to the stress region predicted by a dynamic model. Reliability improvement goals then depend on insuring that control systems maintain stress levels in the system below the ones predicted by the interference model.

For example, the current unreliability of the system is 3.4% and given the strength distribution of the material, this unreliability maps into a stress region between 30 and 40 Newtons. Thus, reliability can be improved using a

dynamic model to design a control system that will insure that the stress region induced in the system falls below the 30-40 N region.

There are some caveats in this approach, though. First, it is necessary to evaluate how well the material strength data obtained from the supplier matches the actual strength of the material while it is being processed. Second, the unreliability model is based on the assumption that every time the strength and stress distributions overlap there is a system failure. That is, the area of overlap (the convolution integral of the two distributions) is equivalent to the unreliability of the system (a known function of time). A better relationship between the convolution integral and the reliability function are needed.

Finally, it should be noted that in none of the cases when data was recorded did a system failure occur. Thus, it is not exactly known what the process parameters where in those occasions when the strength and stress distributions did overlap. It would be invaluable to have a data acquisition system for continuous process variables, such as positions or velocities. The file could be constantly overwritten and only saved after a failure has occurred. This would allow for a mapping of failures to process variables and to better correlate the interference and dynamic models.

Currently, it is difficult to determine the location and shape of the stress distribution curve if no points that are located in that area have been collected. Furthermore, the ability to develop models that predict discrete events from physical descriptions will depend to a great extent on the availability of both continuous and discrete event data.

7.2 Short Term Solutions to Enhance System Reliability

7.2.1 Increased Ramp Times

The analysis of the designed experiment (Section 5.2) clearly reveals that the system is very sensitive to ramp times. For the three output variables that where selected (maximum velocity difference between web demand and web supply, maximum web speed overshoot, and dancer settling time) ramp time was always the most significant factor affecting the output variable. This result confirms the intuitive feel that if the system is accelerated to full speed in a longer period, the probability of successful start-ups is higher. The apparent downside of increasing ramp time is that the amount of scrap that is produced during the startup will be higher. However, this problem is counteracted by increased startup reliability. That is, if the ramp time is increased and start-ups are more successful, then there will less start-ups during which scrap is produced. Furthermore, increased ramp times leading to increased reliability is the first step towards insuring that the process will be able to produce good products at any speed, including startup.

Even more important than ramp time is the actual shape of the ramp-up profile. Figure 5.1c show the sharp discontinuities that occur in both the line reference speed and the unwind motor speed. These "sharp corners" induce unnecessary strain on the hardware (motors, belts, gears, etc.) and the material itself. Besides, it is difficult to mathematically handle these discontinuities when performing controller design. Using an S-shaped ramp-up curve eliminates these unnecessary discontinuities. The digital controller used in the prototype unwind unit uses such curves.

7.2.2 Idler Bearing Maintenance

Friction has a significant effect on the performance of a control system. In the unwind unit application, increased bearing friction results in higher web tensions, that is, the web has to do more work (higher tension) to overcome the drag in the bearings. If bearing friction becomes excessive, the peak tension in the web can reach the 30-40 N range that was identified as the stress region where unreliability occurs. Table 6.1 clearly shows how an increase in bearing friction from its nominal value by a factor of 5 increases peak tension from the 10 N range to the 30 N range. Similarly, an increase by a factor of 10 raises the peak tension up to the 60 N range (guaranteed system failure). Three cases included in table 6.1 are reproduced here. Notice that the nominal bearing friction value is 6.4516 x 10^{-4} Nms

Case No.	K	Damping	Ramp Time	Peak Tension
7	316 N/m	6.4516 e-4 Nms	7.5 sec	12.63 N
8	316 N/m	3.2258 e-3 Nms	7.5 sec	33.85 N
9	316 N/m	6.4516 e-3 Nms	7.5 sec	60.42 N

Table 7.1: Effect of increasing bearing friction on peak web tension

Increasing bearing friction should be avoided at all costs. Implementing a bearing maintenance program that insures periodic revisions is highly recommended. A nominal target value for bearing friction should be determined and bearings that exceed this value by a factor of three or more should be replaced. This simple procedure can significantly reduce the probabilities of peak tensions resulting in material breakouts.

7.2.3 Controller Platform Enhancements

Process control would benefit from the use of digital control platforms. The benefits are seen when the experimental results of the prototype unwind unit are compared with production equipment. The former uses a digital control system; the latter has an analog system.

The first obvious advantage of the digital controllers is its inherent flexibility; control algorithms can be easily implemented in software.

Similarly, the algorithms are easily interfaced with PLC sequences that are implemented on the process for safety reasons.

Second, in digital controllers references do not drift over time. Figure 5.3a and 5.3b show how the initial position of the dancer prior to a start-up was not constant. As a consequence of this result, it is possible that on certain occasions the initial dancer position is too high (not enough web accumulation) and the possibility of a breakout goes up. A digital controller with a reference set in software and adequate integral control would insure that the reference would not drift and that the position error of the dancer would go to zero. Eliminating the possibility of having high initial (prior to a startup) dancer positions contributes to increase the startup reliability of the web handling process.

Figure 5.3c and Figure 6.3 show the dancer startup transient during the last startup that was recorded off the production equipment. There is a sharp peak at the onset of the startup which corresponds to a drop of the dancer arm. It is very likely that this corresponds to the integrator in the analog controller getting saturated and then quickly discharging after the startup. A digital controller would eliminate this peak first by eliminating the need for a capacitor (analog integrator) and second by being able to provide with integrator anti-windup if necessary.

If digital controllers are not implemented, it is necessary to monitor the performance of the analog controllers. Both the drift in reference signal and the saturation of the integrator should be eliminated. Periodic maintenance checks where a couple of startup transients are recorded should be enough to verify whether the controller is performing as intended.

7.3 Limitations of Machine Control and Dynamic Models

The current state of unwind controllers is focused on machine control. Controlling machine states can be very accurate and is well understood. It attempts to keep two machine states under control: dancer position and unwind motor speed. Lumped parameter models that accurately predict these two states have been developed and have proven to give good results. Unfortunately, the control of these two states is done with the expectation that by insuring accurate machine state control, the states of the material (specially tension) will also be controlled. Generally speaking that is the case; that is why reliabilities have reached the 90% region.

However, in spite of good unwind velocity and dancer position control 3.42% of all startups result in failed attempts. That is why it is important to understand the fundamental difference between machine control and process control. The former controls machine states and "hopes" that at the same time material states will be controlled. The latter measures or estimates material states and has set points to control these variables. Notice, though, that even when material states are being controlled, it is only through the machine that

the material can be accessed. Thus, taking the existing systems to reliabilities in the high 90% will require deeper understanding of machine-material interactions.

Figure 7.1 illustrates the difference between machine control and process control for the unwind unit. Notice that in the current control platforms, the only output out of the dancer block is the dancer position. However, we know that imbedded in that block, material states (tensions) are available. If these tension estimates are used in a feedback loop, then process (material state) control will be achieved.

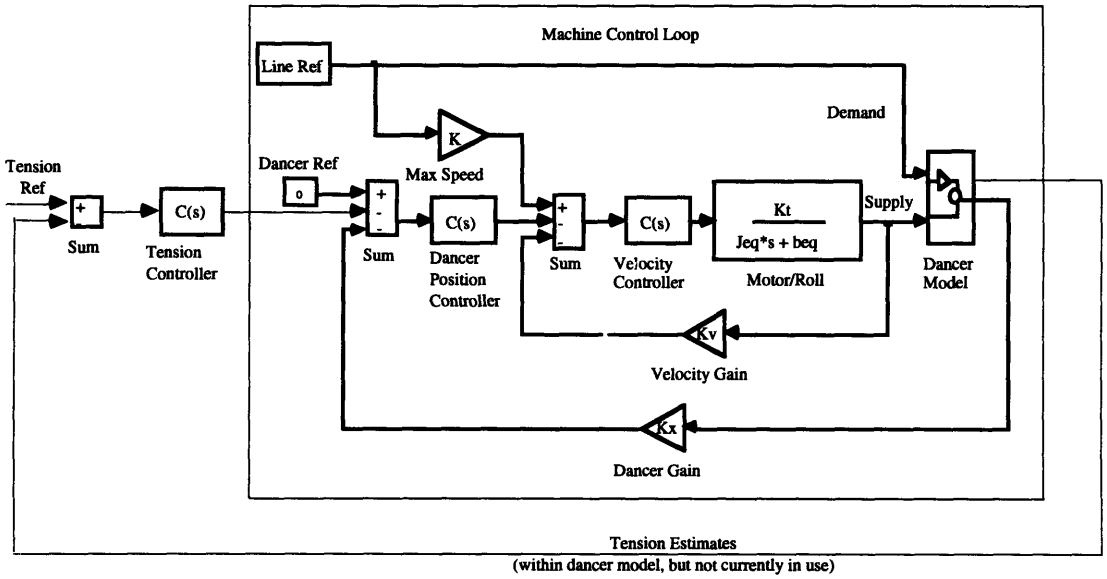

Figure 7.1: Machine and Process Control for Unwind Units

Unfortunately, making the jump from machine to process control is not as simple as it seems in principle. Notice that the main caveat lies in the relationship between machine and material, that is, in how changes in machine states translate into changes in material states.

The linear dynamic model is a reasonable approximation as a tool for performing machine control. Similarly, the detailed non-linear model execution that includes all machine components and all significant non-linearities provides greater accuracy as seen by the process simulation of the designed experiments. Thus, non-linear modeling is the first step towards a better understanding of machine material interaction and process control. Unfortunately, both models limit the prediction of material tension to a single value across a span, that is, tension is only a function of time and not of position within a span.

In reality it is known that within a span there exists a stress distribution in both the machine direction (along the length of the web) and the cross-machine direction (across the web). It is also known that even with accurate machine control there is still a 3.42% probability that the web will break during a startup. Thus we can conclude that localized stress distributions in

the web are responsible for material breakouts. That is, on 3.42% of all startups there is a localized stress somewhere along the web that overlaps with the strength of the material and breaks the web. This conclusion is also supported by the fact that if localized phenomena where not present, then the web would always break just before the metering point (according to the linear model tension is always highest at the span that is further "downstream of the roll). However, breakouts do not always occur just before the metering point.

In order to achieve process reliabilities in the high 90's, it is necessary to reduce or eliminate the 3.42% probability of material breakouts during startup.[1] One way of achieving this goal is to develop a distributed parameter model of the web that accounts for the fact that stresses are distributed in both time and space along the material. With this model, it will be possible not only to predict machine states (such as dancer position or unwind motor speed), but also to predict tensions in the material at different locations along the web path. Having the estimates for the material tension enables the design of a feedback loop where one of the references will be tension, a material state not a machine state.

7.4 Distributed Parameter Model for Process Control

7.4.1 Partial Differential Equation Formulation

As mentioned earlier, the lumped parameter model (linear and non-linear) presented in this thesis ignores the fact that the material is distributed in space and that its states (tension/stress) are not only time, but also space dependent. An alternative way of modeling the web is to treated as a collection of infinitesimal elements of mass as shown in Figure 7.2.

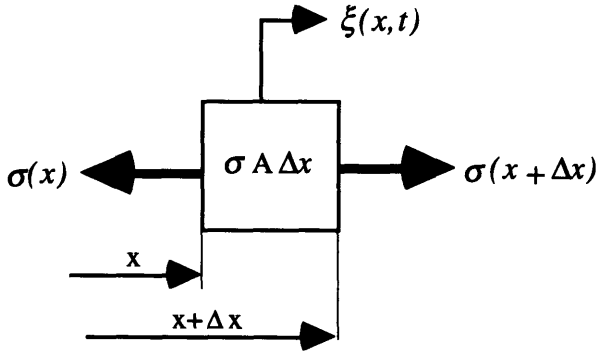

Figure 7.2: Distributed Parameter Web Model

[1] The 3.42% unreliability of the unwind unit might not seem like a significant percentage. However, the entire web handling process consists of a series of several unwind units. If one unit fails, the entire process is shut down. Thus, the combined effect of relatively low unreliability unwind units becomes significant.

The force balance on a single element is:

$$A\sigma(x+\Delta x)-A\sigma(x)=\rho A\Delta x\frac{\partial^2\xi}{\partial t^2} \tag{7.1}$$

Where:

$$\sigma(x)=\frac{E\left[\xi(x)-\xi(x-\Delta x)\right]}{\Delta x} \tag{7.2}$$

As Δx approaches zero Equations (7.1) and (7.2) become:

$$A\frac{\partial\sigma}{\partial x}=\rho A\frac{\partial^2\xi}{\partial t^2} \tag{7.3}$$

$$\sigma(x)=E\frac{\partial\xi}{\partial x} \tag{7.4}$$

Substituting Equation (7.4) into (7.3) and adding an external forcing term to the mass element shown in Figure 7.3 we obtain:

$$A\left[\rho\frac{\partial^2\xi}{\partial t^2}-E\frac{\partial^2\xi}{\partial x^2}\right]=F(t) \tag{7.5}$$

7.4.2 Separation of Variables

Equation (7.5) is simply Newton's second law applied to a web treated as a collection of infinitesimal elements of mass. To obtain a solution to this equation it will be assumed (only initially) that the forcing term F(t)=0 and that the displacement at any point and time is the product of a function of time only and a function of position only, that is:

$$\xi(x,t)=Y(x)f(t) \tag{7.6}$$

Taking the partial differential of Equation (7.6), settling F(t)=0, dividing by ρYf and substituting into Equation (7.5):

$$\frac{1}{f}\frac{d^2f}{dt^2}=\frac{E}{\rho}\frac{1}{Y}\frac{d^2Y}{dx^2} \tag{7.7}$$

Both terms of Equation (7.7) must be equal to the same constant ($-\omega^2$). Thus Equation (7.7), can be separated into two total differential equations.

$$\frac{d^2 f}{dt^2} + \omega^2 f = 0 \tag{7.8}$$

$$\frac{d^2 Y}{dx^2} + \frac{\rho}{E}\omega^2 Y = 0 \tag{7.9}$$

The value of Equations (7.8) and (7.9) is that the solution of a partial differential equation (original formulation in Equation (7.5)) is substituted by the solution of two simultaneous total differential equations. The solution of Equation (7.9) is particularly important. It is related to the displacement of the web as a function of position which is related to the strain and/or tension in the material.

The solutions to Equation (7.9) are well known. These solutions [$Y_n(x)$] are the eigenfunctions or modal shapes in position of the material, i.e.. modes of vibration for the web.

$$Y_n(x) = B_n \sin\left[(2n-1)\pi/2 \frac{x}{4}\right] \quad n = 1, 2, \ldots \tag{7.10}$$

Similarly, modal shapes in time of [$\eta_n(t)$] are obtained using the procedure outlined below.

Now that separation of variables has been shown to be useful, the forced response of the system can be examined. It can be shown that the response of the system (forced or unforced, $\zeta(x,t)$) can be expressed as a linear combination of the modal shapes in time and position.

$$\xi(x,t) = \sum_{n=1}^{\infty} Y_n(x)\eta_n(t) \tag{7.11}$$

Substituting Equation (7.11) into the forced response Equation (7.5) to obtain solutions in terms of the easily solved modal shapes:

$$\sum_{n=1}^{\infty} \rho A Y_n \ddot{\eta}_n - \sum_{n=1}^{\infty} AE \frac{d^2 Y_n}{dx^2} \eta_n = F(t) \tag{7.12}$$

The modal shape functions are orthogonal to each other because they have sinusoidal components. Thus, the following holds:

$$\int_0^L Y_n(x)Y_m(x)dx = 0, \qquad n \neq m \tag{7.13}$$

Orthogonality of the modal shapes is used by multiplying Equation (7.12) by Y_m, integrating over the length of the span (L) and substituting $\frac{d^2Y}{dx^2} = -\frac{\rho}{E}\omega^2 Y$. All terms of the resulting summations will be zero except the one when n=m. Thus, the resulting equation is:

$$\left[\int_0^L \rho A Y_m^2 dx\right]\ddot{\eta}_m + \left[\int_0^L \rho A Y_m^2 dx\right]\omega_n^2 \ddot{\eta}_m = \int_0^L F(t)Y_m dx \tag{7.14}$$

The terms in the brackets are defined as the modal masses (m_m) and the right hand side term is defined as the modal forcing function [F(t) Ym(L)]. Similarly, the modal stiffness is defined as $k_m = m_m \omega_m^2$. Equation (7.14) can then be rewritten as:

$$m_m \ddot{\eta}_m + k_m \eta_m = F(t)Y_m(L) \tag{7.15}$$

In summary, the procedure to obtain the displacement of the distributed parameter web described by Equation (7.11) is the following: [2]

- Obtain modal shape functions in position, Ym.
- Substitute these functions evaluated at the point where the force is being applied into Equation (7.15) to obtain the modal forcing function.
- Solve for the modal shapes in time.
- Substitute modal shapes (time and position) into Equation (7.11) and obtain displacements as a function of time and position.

7.4.3 State Equation Equivalents of Modal Shape Functions

By defining two state variables, it is possible to describe the m modal equations as two state equations. Furthermore, this makes it possible to describe the distributed parameter model of a span with an equivalent bond graph with m discrete components that correspond to the m modal shapes. If the modal momentum p_m and the modal displacement q_m are defined as follows Equation (7.15) is equivalent to:

$$\begin{aligned} \frac{d}{dt}(p_m) &= -k_m q_m + F(t)Y_m(L) \\ \frac{d}{dt}(q_m) &= \frac{p_m}{m_m} \end{aligned} \tag{7.16}$$

---

[2] All of this development is discussed in detail by Karnopp et al [11] p. 368-388.

Given:

$$p_m \equiv m_m \dot{\eta}_m$$
$$q_m \equiv \eta_m$$

In terms of the state equations (7.16) each modal shape corresponds to a spring, a mass and a transformer. Thus, each span of material will no longer be a simple spring, but a combination of springs, masses and transformers that approximate the continuous nature of the material and predict the displacement (strain and consequently tension) of the web as a function of time and position. The equivalent bond graph for a span with m modal shapes is shown below.

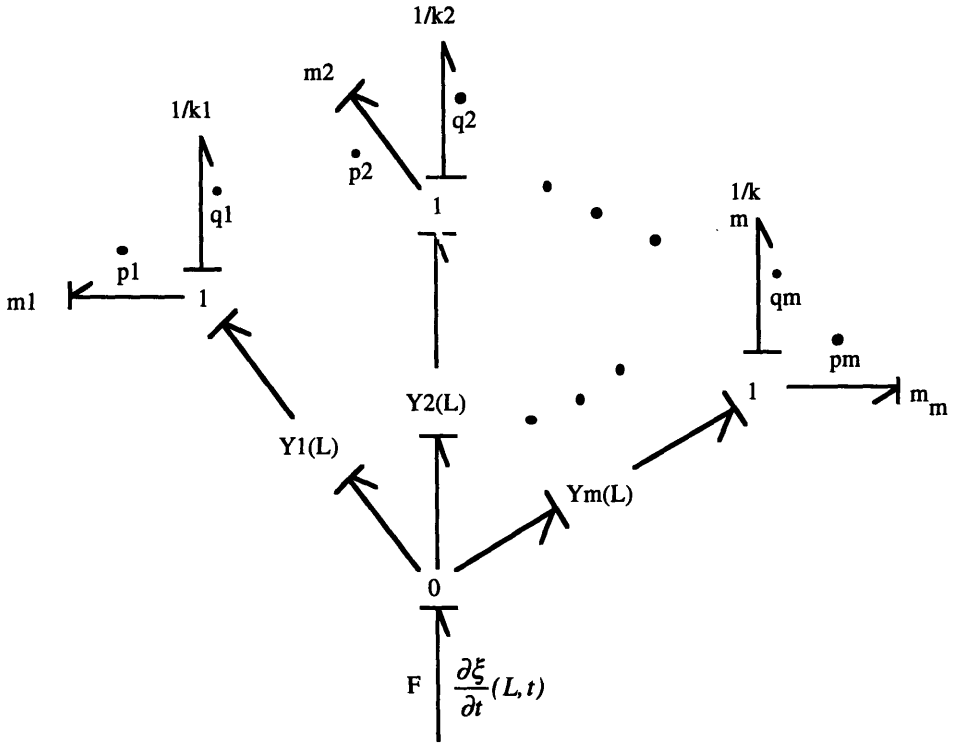

Figure 7.3: Bond Graph Equivalent of a Distributed Parameter Web Model

Notice two caveats in the modeling approach presented here. The first caveat is adequately determining the boundary conditions at each end of the spans, particularly the external force acting on the web. In general the velocities at the endpoints of the spans are known or can be measured, but the forces can't. Secondly, it is not obvious what is the minimum number of modal shapes necessary to adequately model the spatial distribution of the tension in the material.

Assuming that these two issues can be successfully resolved and that using modal shapes, the strain and tension of the web as a function of time and position can be predicted, the following control strategy can be implemented.

7.4.4 Tension Estimates in Full State Feedback Control

Direct tension measurements of the web are not currently realizable. Contact sensors alter the actual value of tension and thus bias measurements; non-contact sensors are too expensive or unavailable; and load cells on idlers are difficult to install and noise and vibration levels in the machine are much greater than tension levels. Thus, if tension is to be directly controlled, it has to be estimated from other process parameters.

The boundary conditions for the distributed parameter model are determined by the velocities at the ends of the spans. If these velocities are measured using either contact or non-contact velocity sensors (like the one used in the experimental section of this thesis) it is possible to estimate web tensions. These tension estimates are then used in a feedback loop. Tension set points are compared with the estimates and the control algorithm employed determines what the velocity of the unwind motor should be in order to maintain minimum tension. Schematically, the controller layout would be:

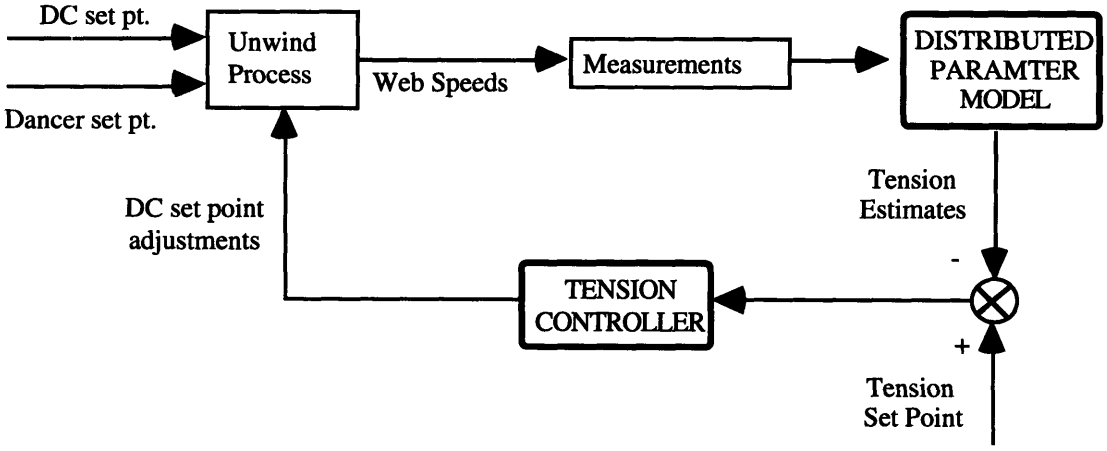

Figure 7.4: Tension Controller Schematic

Note that the control scheme presented above is very similar to Kalman Filter estimators and other state observers. These estimators have been used successfully in other applications where it is not possible to directly measure a state that is to be controlled. One of such applications is the control of bar tension in a steel rolling process as presented in McFarlane and Stone [8]. Other similar applications are also found in the literature.

Figure 7.4 assumes that only the unwind motor is to be controlled. However, given the localized peak tension and modes of vibration of the web it is very likely, that a single control point (single motor) will not be able to adequately control the tension of the web across the various spans. Thus it is reasonable to consider that instead of only controlling the rate at which web is being supplied and the rate at which it is being used up, additional control points could be added.

Think for example of the extreme case in which every idler is attached to a servo motor. By accurately controlling the velocities of the idlers, the flow of material and consequently the tension will be better controlled. The system would no longer depend on the web "surviving" its path from the unwind unit (control point A) to the metering roll (control point B). Unfortunately, this approach is limited by the cost of velocity sensors and servo controllers. However, the value of added control points should be recognized and a combination of increased material modeling (continuous web model) and additional control points should be pursued.

Appendix A

Ultimate Tensile Strength Distributions

The UTS histograms for the data sets from Plant A, Plant B, and Plant A and B combined are shown below. Normal distribution curves are superimposed and as seen the distributions are not completely normal. That is why a Weibull function was used to fit the data in Chapter 2.

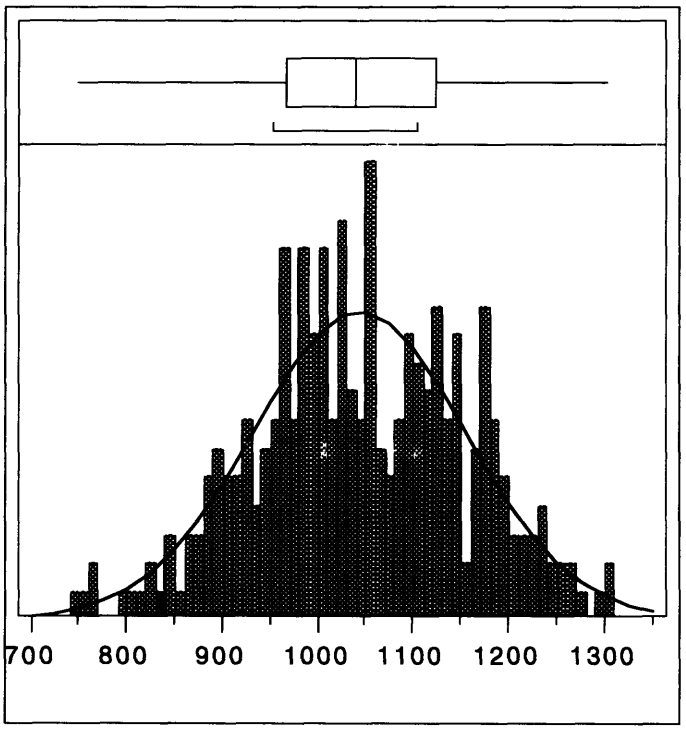

Figure A.1: Ultimate Tensile Strength Histogram #1 from Plant A

Recall that once A Weibull function was fit to the data, the integral or the cummulative probability distribution function (CDF) of the data was calculated. These CDF's can then be used to easily locate the point on the UTS axis where 3.42% of the area under the PDF curves is located. This point corresponds to the maximum UTS that results in unreliable startups.

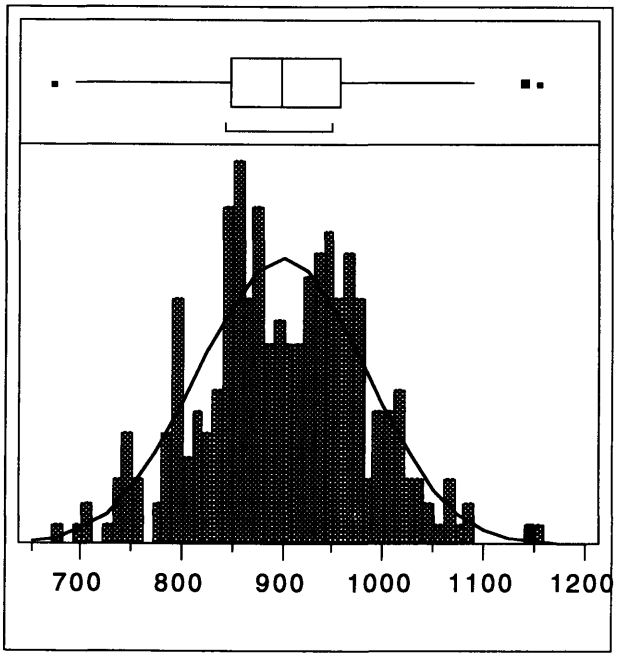

Figure A.2: Ultimate Tensile Strength Histogram #2 from Plant A

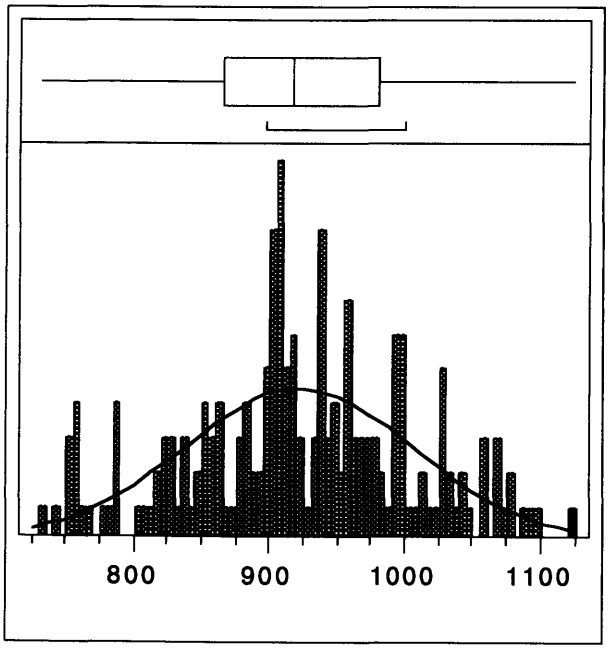

Figure A.3: Ultimate Tensile Strength Histogram from Plant B

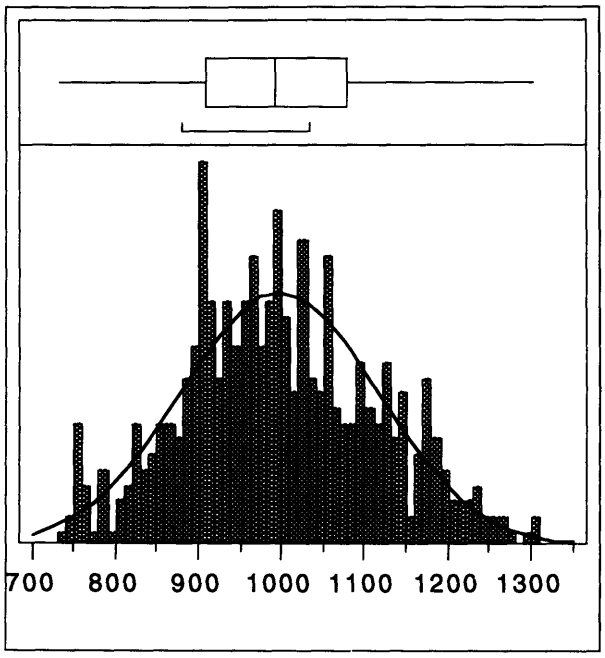

Figure A.4: Ultimate Tensile Strength Histogram from Plants A and B

The cummulative probability functions are shown below. They are followed by an enlargement of the 0 to 4% region.

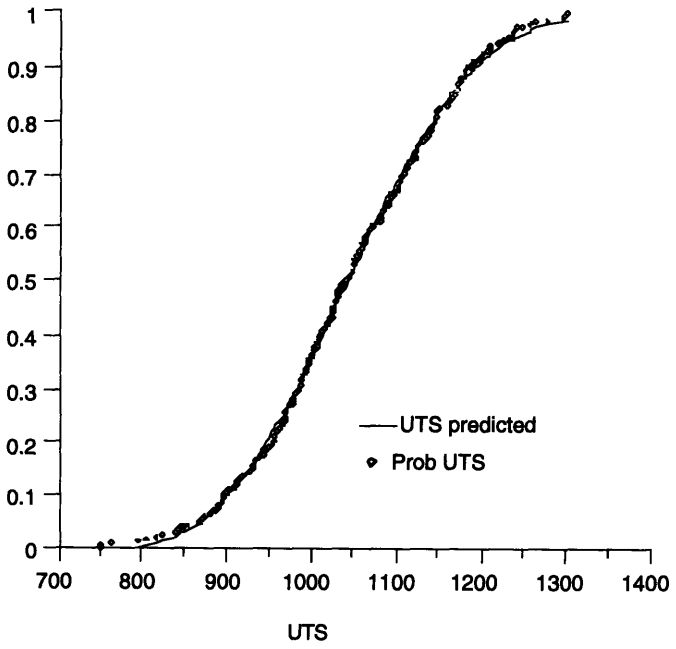

Figure A.5: Ultimate Tensile Strength CDF #1 for Plant A

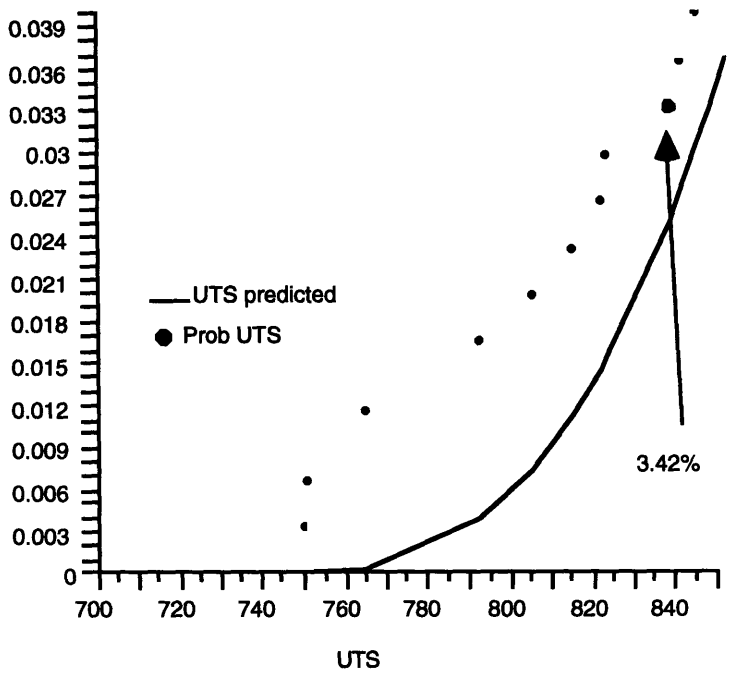

Figure A.6: Ultimate Tensile Strength CDF #1 for Plant A (0-4%)

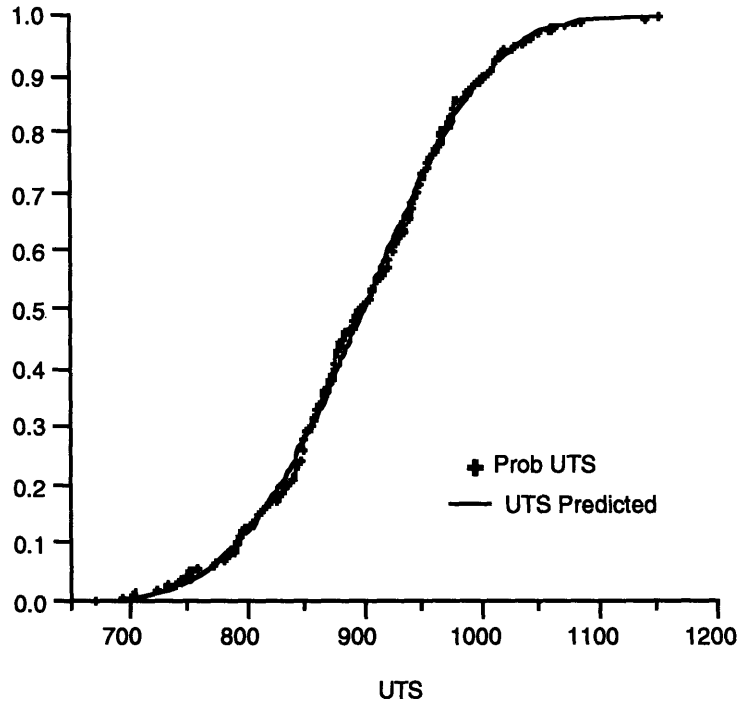

Figure A.8: Ultimate Tensile Strength CDF #2 for Plant A

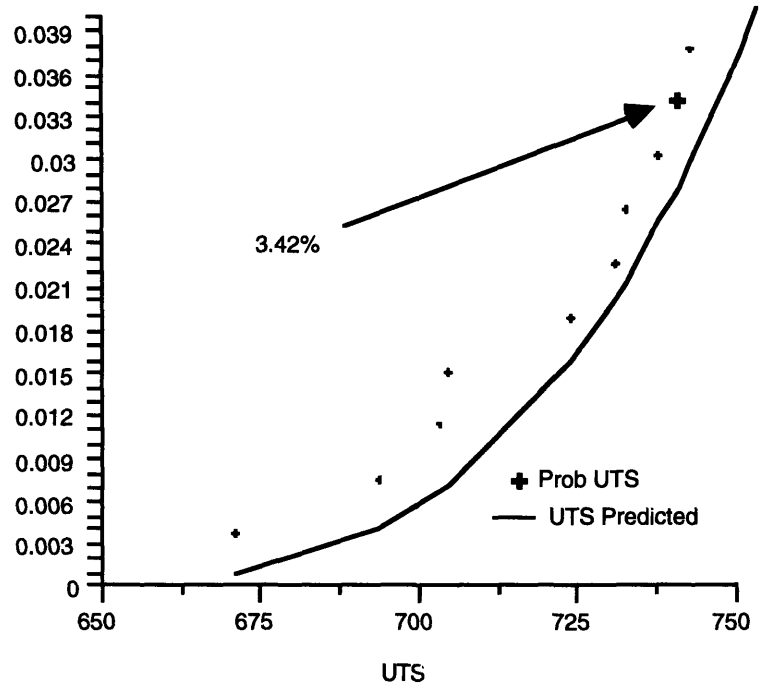

Figure A.9: Ultimate Tensile Strength CDF #2 for Plant A (0-4%)

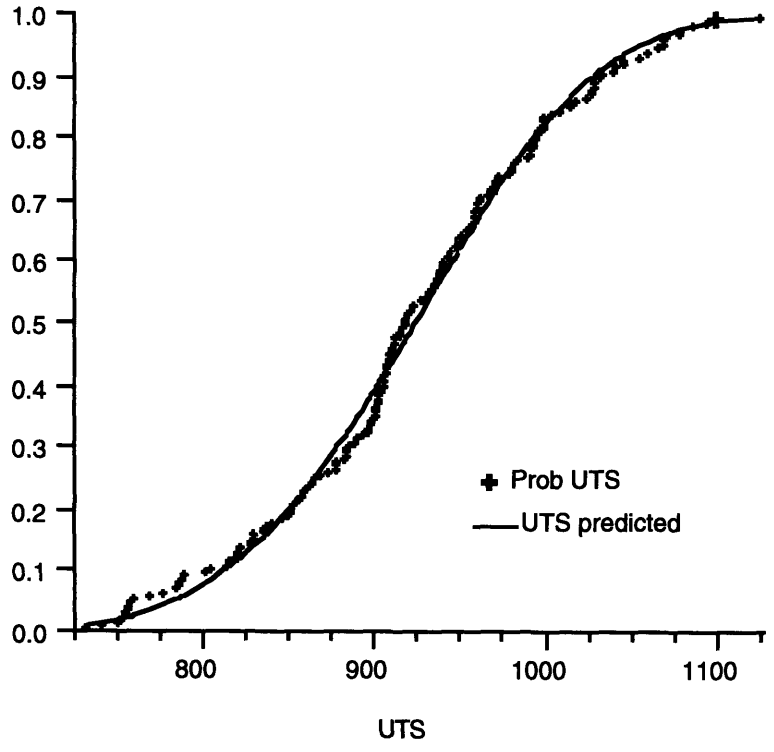

Figure A.9: Ultimate Tensile Strength CDF for Plant B

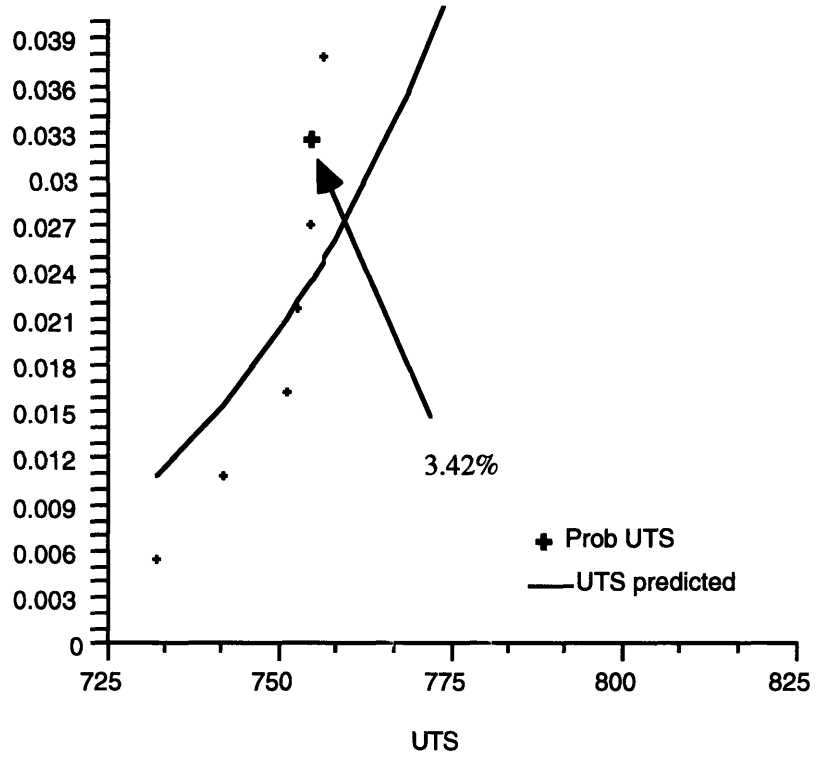

Figure A.10: Ultimate Tensile Strength CDF for Plant B (0-4%)

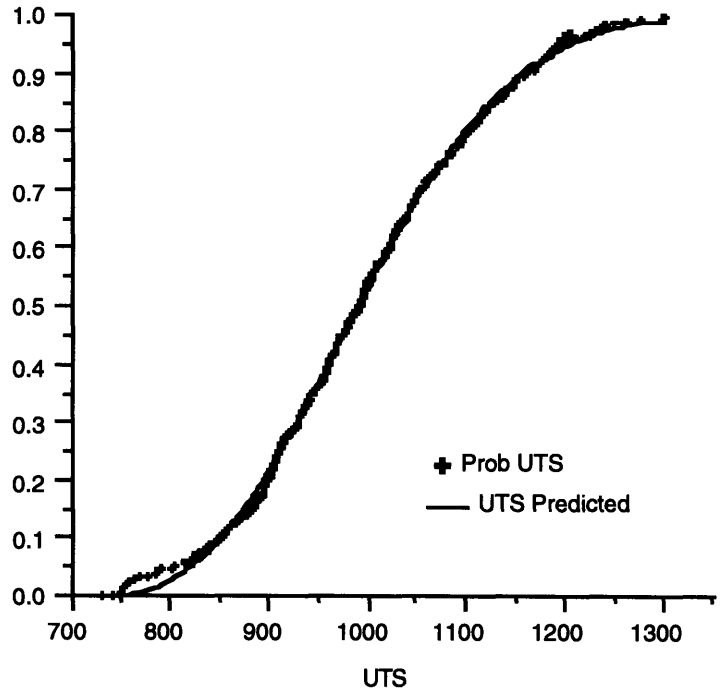

Figure A.11: Ultimate Tensile Strength CDF for Plants A and B

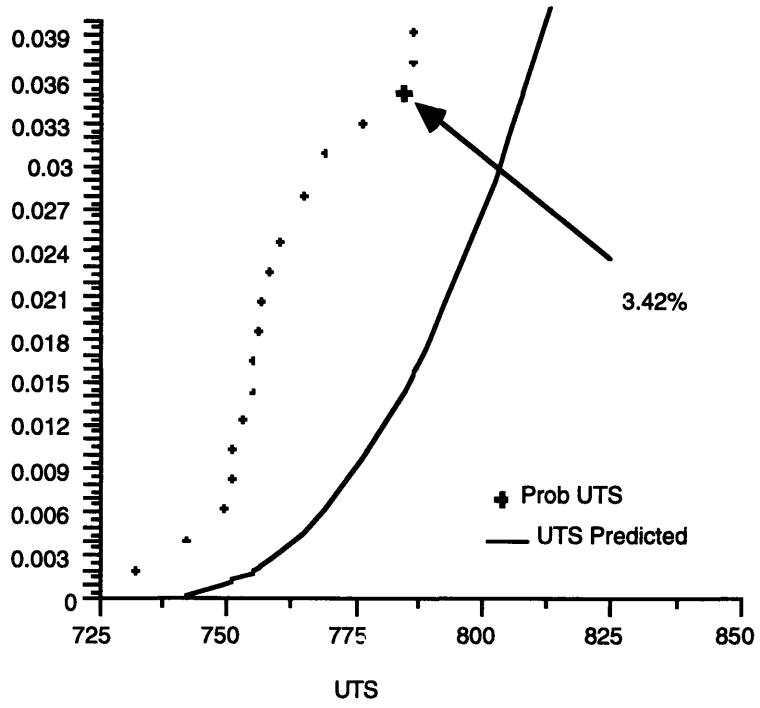

Figure A.12: Ultimate Tensile Strength CDF for Plants A and B (0-4%)

Appendix B

Non-linear Model Equivalent Inertia and Geometric Assumptions

B.1 Belt Drive Transmission and Equivalent Inertia

The belt drive transmission of the prototype unwind unit is configured as shown below:

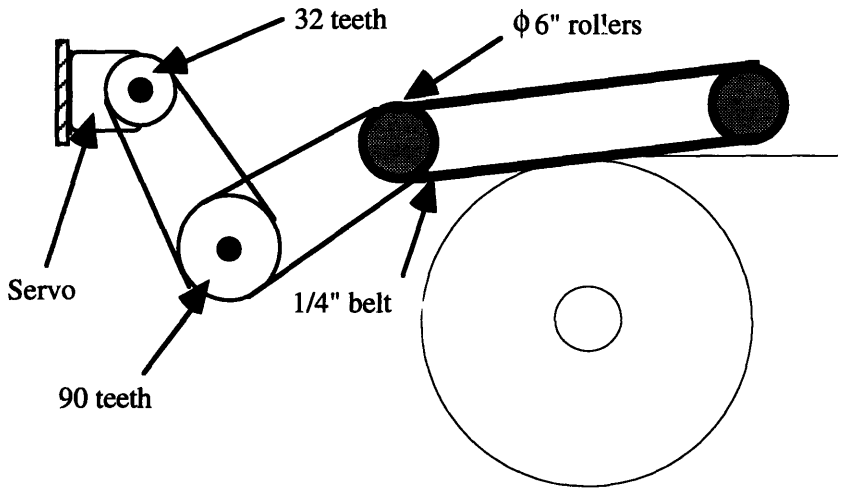

Figure B.1: Belt Drive Transmission Layout

The system shown in Figure B.1 can be represented with the bond graph shown in Figure B.2. Note the the shaft modelled as a torsional spring is neglected in the final analysis.

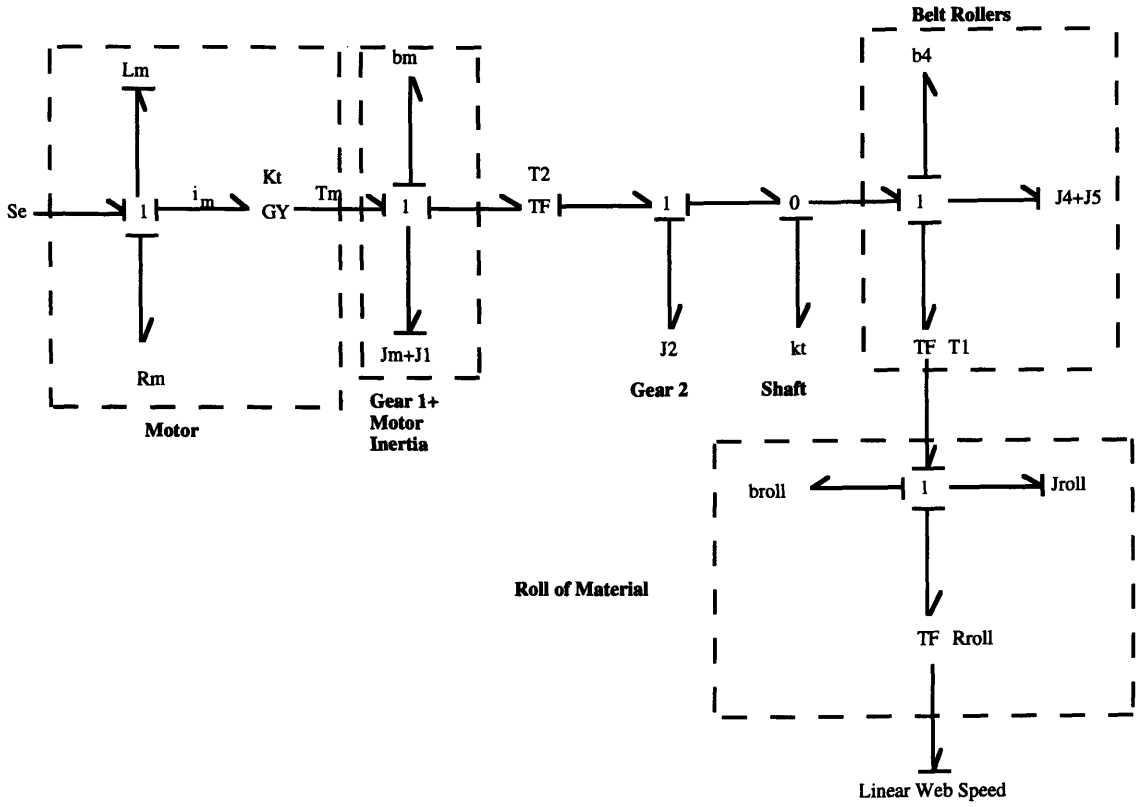

Figure B.2: Belt Drive Transmission Bond Graph

Reflecting the equivalent inertia of the roll into the belt we obtain the following relationships:

$$J_{eq_1} = \frac{J_{roll}}{T_1^2} \qquad \text{and} \qquad b_{eq_1} = \frac{b_{roll}}{T_1^2} \tag{B.1}$$

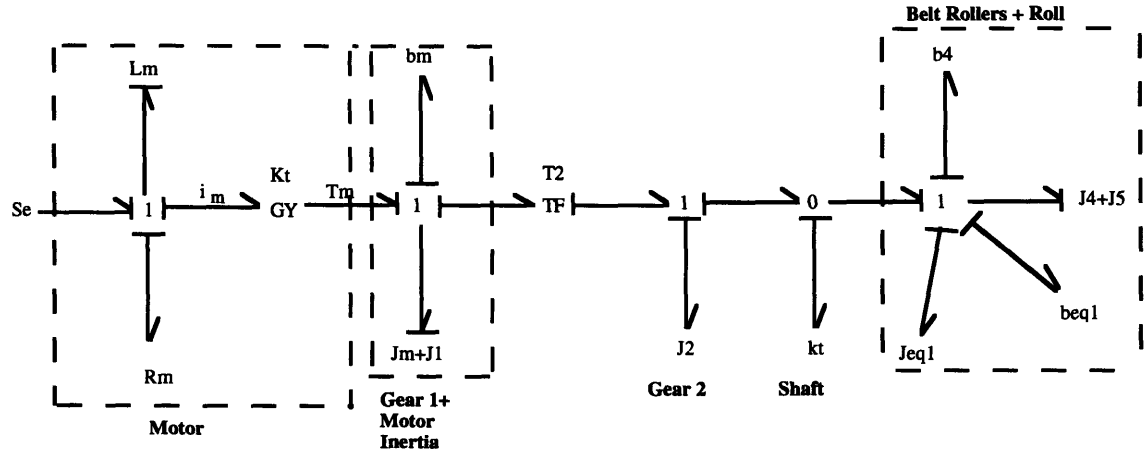

Figure B.3: Belt Drive Transmission Equivalent Bond Graph #1

Because J_{eq1} has derivative causality, it can be combined with J_4 and J_5. Similarly, b_4 and b_{eq1} are in series so they can be combined. Ignoring the torsional spring of the shaft, the resulting bond graph is shown below. Note that:

$$J_{eq_2} = J_{eq_1} + J_4 + J_5 \qquad \text{and} \qquad b_{eq_2} = b_{eq_1} + b_4 \tag{B.2}$$

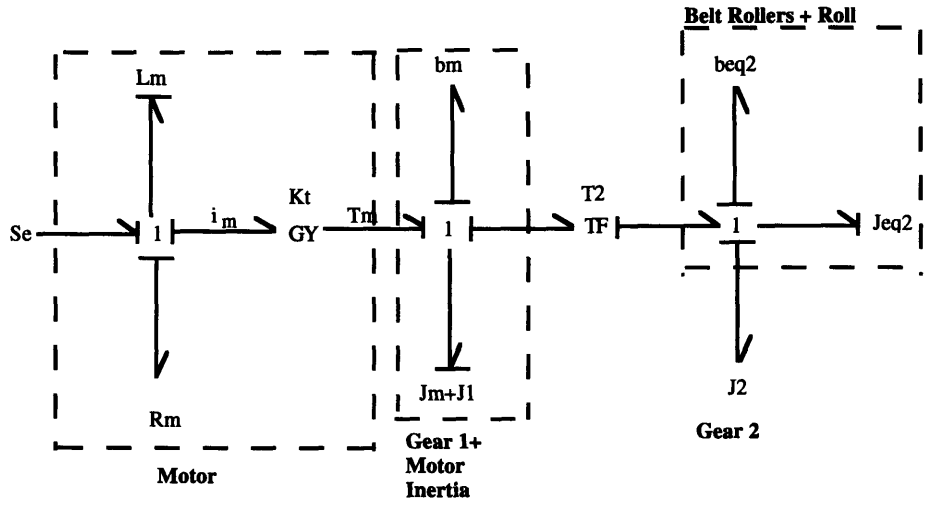

Figure B.4: Belt Drive Transmission Equivalent Bond Graph #2

Finally, by reflecting the equivalent inertia onto T2, grouping elements in series and inertias with derivative causality, and ignoring the dynamics of the inductance in the motor, the following bond graph is obtained. Note the following relationships:

$$J_{eq_3} = J_{motor} + J_1 + \frac{J_2}{T_2^2} + \frac{J_4 + J_5}{T_2^2} + \frac{J_{roll}}{T_1^2 T_2^2} \tag{B.3}$$

$$b_{eq} = b_{motor} + \frac{b_{beltrollers}}{T_2^2} + \frac{b_{rollmandrel}}{T_1^2 T_2^2} \tag{B.4}$$

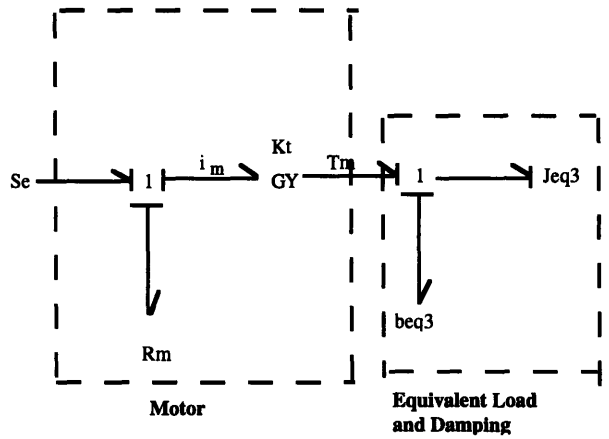

Figure B.5: Belt Drive Transmission Final Equivalent Bond Graph

B.2 Dancer Spans Lengths as a Function of Angular Displacement

The exact span length (Ln) as a function of θ_a (as shown in Figure B.6) is given by the following relationship:

$$L_n = \sqrt{(x_o - R_n \sin\theta_a)^2 + [y_o - R_n(1-\cos\theta_a)]^2} \qquad \text{(B.5)}$$

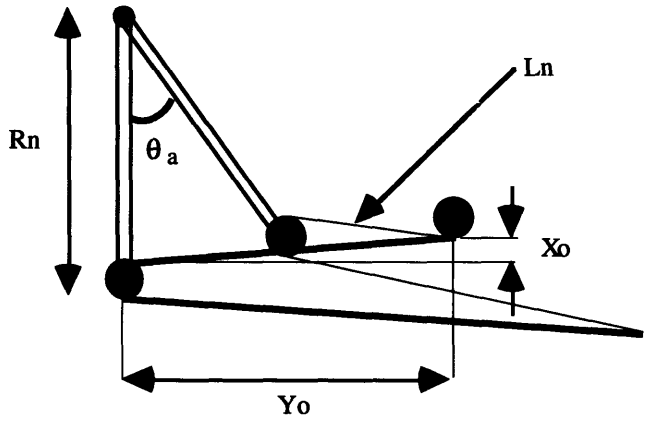

Figure B.6: Span Length Geometry

However, the dancer span length can be approximated by:

$$\begin{aligned} L_n &= l_{n_o} - R_n \sin\theta \\ L_n &\approx l_{n_o} - R_n\theta \qquad \text{for small } \theta \end{aligned} \qquad \text{(B.6)}$$

Where l_{no} is the initial span length.

A worksheet was created to compare the spans lengths of the dancer of the prototype unwind unit when calculated by Equations (B.5) and (B.6). The results are shown below.

span#	Radius (Rn)	Angle (theta_a)	in rads	length (non-linear)
1	21	34.497	0.601781	16.52404727
2	23	34.497	0.601781	10.27434209
3	25	34.497	0.601781	9.117521769
4	27	34.497	0.601781	6.719900926
5	29	34.497	0.601781	5.583565717
6	31	34.497	0.601781	5.717949255
7	33	34.497	0.601781	4.637349041
8	35	34.497	0.601781	13.64935818
			All spans =	**72.22403424**
span#	**delta length**			length (linearized)
1	0.41238877			16.1116585
2	-0.7050934			10.9794355
3	-0.7296907			9.847212504
4	-0.9950886			7.714989504
5	-0.9992008			6.582766505
6	0.26740575			5.450543505
7	-0.6809715			5.318320505
8	1.46326067			12.18609751
	-1.9669898		All spans =	**74.19102404**

Table B.1: Span Lengths for Maximum Positive Displacement

span#	Radius (Rn)	Angle (theta_a)	in rads	length (non-linear)
1	21	-38.891	-0.67843	41.45101183
2	23	-38.891	-0.67843	37.68429259
3	25	-38.891	-0.67843	38.94301289
4	27	-38.891	-0.67843	38.95677091
5	29	-38.891	-0.67843	40.22475147
6	31	-38.891	-0.67843	42.74545285
7	33	-38.891	-0.67843	44.02043146
8	35	-38.891	-0.67843	54.5187748
			All spans =	**338.5444988**
span#	**delta length**			length (linearized)
1	0.27198028			41.17903155
2	-0.7498848			38.43417741
3	-0.7463104			39.68932328
4	-0.9876982			39.94446914
5	-0.9748635			41.199615
6	0.29069199			42.45476086
7	-0.6894753			44.70990672
8	0.55372221			53.96505259
	-3.0318378		All spans =	**341.5763365**

Table B.2: Span Lengths for Maximum Negative Displacement

As shown by the tables above there is no major difference between the non-linear and the linear calculations of the span lengths.

Bibliography

[1] American Society of Quality Control Course Notes. *Reliability Engineering Student Manual: An Introdcution to a Programmatic Treatment of Reliability Engineering.* ASQC, Milwaukee, WI. 1990.

[2] Stephen H. Crandall, Dean C. Karnopp, Edward F. Kurtz, Jr., and David C. Pridmore-Brown. *Dynamics od Mechanical and Electromechanical Systems.* Robert E. Krieger Publishing Company. Malabar, Florida. 1982.

[3] Mathew E. Girgash. Programable Digital Winder Drives. *Reliance Electric Co. Finishing and Converting Conference Proceedings.* Atlanta, GA. 1988.

[4] W. Grant Ireson, and Clyde F. Coombs, Jr. *Handbook of Reliability Engineering and Management.* McGraw-Hill Inc. 1988.

[5] C. E. Kardamilas, and G. E. Young. Stochastic Modeling of Lateral Web Dynamics. *Proceedings of the American Control Conference.* San Diego, CA, May 23-25, 1990.

[6] Dean C. Karnopp, Donald L. Margolis, and Ronald C. Rosenberg. *System Dynamic: A Unified Approach.* Second Edition. John Wiley & Sons, Inc. 1990.

[7] Dimitri Kececioglu. *Reliability Engineering Handbook. Vol 1&2.* Prentice-Hall. 1991

[8] D.C. McFarlane and P.M. Stone. Minimum Tension in a Merchant Bar Rolling Mill Using Modern Control Techniques. *Proceedings of the 11^{th} Triennial World Congress of the International Federation of Automatic Control. 1991.*

[9] Katsuhiko Ogata. *Modern Control Engineering.* Second Edition. Prentice Hall, Inc. 1990.

[10] J. David Pfeiffer. Mechanics and Dynamics of Web Motion Between Spans. *Proceedings of the American Control Conference.* San Diego, CA, May 23-25, 1990.

[11] J. J. Shelton. Dynamics of Web Tension Control with Velocity or Torque Control. *Proceedings of the American Control Conference.* Minneapolis, MN, June 1987.

[12] G. E. Young, R. L. Lowery, and D. W. Plummer. Longitudinal Dynamics of he Rewind Portion of a Web Handling Machine. *Proceedings of the American Control Conference.* Seattle, WA, June 18-20, 1986.

[13] G. E. Young, J. J. Shelton, and B.Fang. Interaction of Web Spans: Part 1: Statics, Part 2: Dynamics. *ASME Journal of Dynamic Systems, Measurement and Control.* September 1989.

[14] G. E. Young, J. J. Shelton, and C.Kardamilas. Modeling and Control of Multiple Web Spans Using State Estimation. *ASME Journal of Dynamic Systems Measurement and Control.* September 1989.